

# Investigation of Thermal Loads onto a Cooled Strut Injector inside a Scramjet Combustion Chamber

A thesis accepted by the Faculty of Aerospace Engineering and Geodesy  
of the University of Stuttgart in partial fulfilment of the requirements  
for the degree of Doctor of Engineering Sciences (Dr.-Ing.)

by

**Dipl.-Ing. Nils Christoph Dröske**

born in Stuttgart, Germany

Committee chair: Prof. Dr.-Ing. Jens von Wolfersdorf  
Committee member: apl. Prof. Dr.-Ing. Peter Gerlinger  
Date of defence: August 8<sup>th</sup>, 2016

Institute of Aerospace Thermodynamics  
University of Stuttgart  
2016



---

## Acknowledgments

---

This thesis originated out of the work during my time as research associate at the Institute of Aerospace Thermodynamics (ITLR) at the University of Stuttgart. The research was partially conducted within the framework of the Research Training Group GRK 1095 ‘Aero-Thermodynamic Design of a Scramjet Propulsion System for Future Space Transportation Systems’, funded by the German Research Foundation (DFG). I would like to thank Prof. Dr.-Ing. habil. Bernhard Weigand as head of the graduate school, and also in his role as director of the institute, for providing an excellent work environment.

My sincere gratitude belongs to my thesis supervisor Prof. Dr.-Ing. Jens von Wolfersdorf, who got me interested in this project and always provided motivation and an open door for questions during the course of the work. This thesis benefited a lot from his expertise, his invaluable advice and from numerous productive discussions. Furthermore, I would like to thank apl. Prof. Dr.-Ing. Peter Gerlinger for his interest in my work and for agreeing to co-referee this thesis.

Among all the colleagues and friends, who contributed to a memorable time at the institute, some have to be mentioned in particular at this point. My special thanks go to Felix Förster for countless fruitful and entertaining discussions, for his company during long hours of experimental campaigns, and for sharing phases of temporary frustration in times of technical failures. The cooperation with Konrad Makowka, who designed important modules of the numerical solver, started within the GRK 1095 and simplified solver development considerably. Thanks for all the work on programming, the fiddling with OpenFOAM, and the occasional bug hunting in the source code. Moreover, many thanks belong

to my predecessor Jiby Vellaramkalayil, who introduced me to the world of scramjets and taught me many useful lessons on dealing with the experimental facility and its somewhat special characteristics. I would also like to thank my long-term office mate Kristian Haase for an outstanding work atmosphere and for providing a non-scramjet point of view when things got stuck.

The experimental part of this work could not have been done without the help of the workshops at ITLR. Their support in conducting the test campaigns, as well as their constant commitment to tackle tricky issues, was essential for the success of the research. Therefore, I would like to thank Christian Otto, Dennis Nehring, Jürgen Fauser, Olaf Ordner and Eberhard Mayer from the mechanical workshop as well as Uli Schwaderer and Thomas Bernik from the electrical workshop.

Finally, I would like to express my deepest gratitude to my family. This thesis would not have been possible without their patience and unconditional support not only during the thesis itself, but also on the whole path that lead there.

Stuttgart, August 2016

Nils Dröske

---

## Contents

---

<b>List of Figures</b>	<b>ix</b>
<b>List of Tables</b>	<b>xiii</b>
<b>List of Symbols</b>	<b>xv</b>
<b>Abstract</b>	<b>xxi</b>
<b>Kurzfassung</b>	<b>xxiii</b>
<b>1 Introduction</b>	<b>1</b>
1.1 Air-Breathing Supersonic Propulsion Systems . . . . .	3
1.1.1 Ramjet . . . . .	5
1.1.2 Dual-mode Ram/Scramjet . . . . .	7
1.1.3 Scramjet . . . . .	7
1.2 State of Knowledge . . . . .	8
1.2.1 Selected Research Programs . . . . .	9
1.2.2 Fuel Injection Concepts . . . . .	14
1.3 Objectives and Outline of the Thesis . . . . .	18
1.4 Publications . . . . .	19
<b>2 Physical Fundamentals</b>	<b>21</b>
2.1 Governing Equations for Compressible, Viscous Flow . . . . .	21
2.1.1 Conservation of Mass . . . . .	22
2.1.2 Conservation of Momentum . . . . .	23

## Contents

---

2.1.3	Conservation of Energy . . . . .	24
2.1.4	Equations of State . . . . .	26
2.2	Heat Conduction and Heat Transfer . . . . .	27
2.3	High-Speed Flows . . . . .	28
2.3.1	Shock Waves and Prandtl-Meyer Expansion Fans . . . . .	29
2.3.2	Viscous Interactions . . . . .	31
<b>3</b>	<b>Experimental Methods</b>	<b>37</b>
3.1	Experimental Facility . . . . .	37
3.1.1	Model Combustion Chamber . . . . .	39
3.1.2	Modular Test Channel . . . . .	40
3.1.3	Fuel Injectors . . . . .	41
3.2	Measurement Techniques . . . . .	44
3.2.1	Mass Flow Measurements . . . . .	44
3.2.2	Temperature Measurements . . . . .	44
3.2.3	Static Wall Pressure . . . . .	45
3.2.4	Schlieren Imaging . . . . .	45
3.2.5	Laser-Induced Thermal Acoustics . . . . .	47
3.2.6	Infrared Thermography . . . . .	48
<b>4</b>	<b>Numerical Methods</b>	<b>51</b>
4.1	Fundamentals . . . . .	51
4.1.1	Finite Volume Method . . . . .	52
4.1.2	Turbulence . . . . .	53
4.2	Solver Development . . . . .	61
4.2.1	Multi-Species Transport . . . . .	62
4.2.2	Chemical Reactions . . . . .	63
4.2.3	Conjugate Heat Transfer . . . . .	63
4.2.4	Local Time-Stepping . . . . .	64
4.3	Additional Developments for OpenFOAM . . . . .	65
4.3.1	Improved Wall Function . . . . .	65
4.3.2	Changes in Post-Processing Tools . . . . .	66
<b>5</b>	<b>Solver Validation</b>	<b>67</b>
5.1	15°-Wedge . . . . .	68
5.1.1	Numerical Setup . . . . .	68
5.1.2	Results . . . . .	69
5.2	Flat Plate . . . . .	71
5.2.1	Numerical Setup . . . . .	72
5.2.2	Adiabatic Plate, $M_\infty = 2.0$ . . . . .	72
5.2.3	Adiabatic Plate, $M_\infty = 4.5$ . . . . .	78

---

5.2.4	Isothermal Plate, $M_\infty = 6.0$ . . . . .	83
5.2.5	Computational Costs for Transient and LTS Simulations . . . . .	85
5.3	Shock Wave/Boundary Layer Interaction . . . . .	85
5.4	Intermediate Summary: Numerical Settings . . . . .	91
5.5	Model Combustion Chamber . . . . .	91
5.5.1	Two-Dimensional Simulations . . . . .	93
5.5.2	Three-Dimensional Simulations . . . . .	98
5.6	Summary . . . . .	105
<b>6</b>	<b>Investigation of Thermal Loads onto the Lobed Strut Injector</b>	<b>107</b>
6.1	Test Matrix and Numerical Setup . . . . .	107
6.2	Moderate Flow Conditions . . . . .	111
6.2.1	External Channel Flow . . . . .	112
6.2.2	Internal Flow Field . . . . .	117
6.2.3	Injector Surface . . . . .	118
6.3	Hot Flow Conditions . . . . .	127
6.3.1	External Combustor Flow . . . . .	127
6.3.2	Internal Flow Field . . . . .	129
6.3.3	Injector Surface and Body . . . . .	131
6.4	Summary . . . . .	142
<b>7</b>	<b>Conclusion and Outlook</b>	<b>143</b>
	<b>Bibliography</b>	<b>147</b>
	<b>Appendix</b>	
<b>A</b>	<b>Iisentropic Relations</b>	<b>167</b>
<b>B</b>	<b>Modified JANAF Coefficients</b>	<b>169</b>
<b>C</b>	<b>Additional Data for the Investigation of the Strut Injector</b>	<b>171</b>
C.1	Uncertainty Analysis . . . . .	171
C.2	Injector Material Variation . . . . .	173
<b>D</b>	<b>Scaling Performance of <i>scramjetFoam</i></b>	<b>175</b>



---

## List of Figures

---

1.1	Comparison of specific impulses for different propulsion systems .	3
1.2	Ideal Joule cycle for turbojets . . . . .	4
1.3	Ideal and real Brayton cycle for ramjets . . . . .	5
1.4	Schematic of a ramjet . . . . .	6
1.5	Schematic of a dual-mode ram/scramjet . . . . .	7
1.6	Schematic of a scramjet . . . . .	8
1.7	Examples of three-dimensional injector trailing edge geometries .	16
1.8	Lobed strut injector investigated at ITLR during the GRK 1095	17
2.1	High speed flow phenomena . . . . .	29
2.2	Shock wave/boundary layer interaction . . . . .	34
2.3	Flow structures in a pseudo-shock region . . . . .	35
3.1	ITLR combustion test facility . . . . .	38
3.2	Operational range of the facility for different Laval nozzles . . . .	39
3.3	Schematic of the model combustion chamber . . . . .	40
3.4	Schematic of the modular test channel . . . . .	41
3.5	Schematics of the fuel injectors . . . . .	42
3.6	Geometry of the strut injector . . . . .	43
3.7	Internal flow path of the strut injector . . . . .	43
3.8	Schlieren imaging setup . . . . .	46
3.9	Focusing schlieren imaging setup . . . . .	46
3.10	Infrared measurement setup . . . . .	49

## List of Figures

---

5.1	Flow over a 15°-wedge, numerical setup . . . . .	69
5.2	Flow over a 15°-wedge, pressure ratio $p/p_\infty$ at different locations . . . . .	70
5.3	Flow over a 15°-wedge, Mach number distribution . . . . .	71
5.4	Flow over a flat plate, numerical setup . . . . .	72
5.5	Flow over an adiabatic flat plate at $M_\infty = 2.0$ , boundary layer profiles . . . . .	73
5.6	Flow over an adiabatic flat plate at $M_\infty = 2.0$ , skin friction coefficient . . . . .	74
5.7	Flow over an adiabatic flat plate at $M_\infty = 2.0$ , influence of $Pr_t$ on the boundary layer profiles . . . . .	75
5.8	Flow over an adiabatic flat plate at $M_\infty = 2.0$ , influence of $Pr_t$ on the skin friction coefficient . . . . .	75
5.9	Flow over an adiabatic flat plate at $M_\infty = 2.0$ , influence of the flux reconstruction scheme on the boundary layer profiles . . . . .	77
5.10	Flow over an adiabatic flat plate at $M_\infty = 2.0$ , influence of the flux reconstruction scheme on the skin friction coefficient . . . . .	77
5.11	Flow over an adiabatic flat plate at $M_\infty = 4.5$ , boundary layer profiles . . . . .	79
5.12	Flow over an adiabatic flat plate at $M_\infty = 4.5$ , skin friction coefficient . . . . .	79
5.13	Flow over an adiabatic flat plate at $M_\infty = 4.5$ , influence of $Pr_t$ on the boundary layer profiles . . . . .	80
5.14	Flow over an adiabatic flat plate at $M_\infty = 4.5$ , influence of $Pr_t$ on the skin friction coefficient . . . . .	81
5.15	Flow over an adiabatic flat plate at $M_\infty = 4.5$ , influence of the flux reconstruction scheme on the boundary layer profiles . . . . .	82
5.16	Flow over an adiabatic flat plate at $M_\infty = 4.5$ , influence of the flux reconstruction scheme on the skin friction coefficient . . . . .	82
5.17	Flow over an isothermal flat plate at $M_\infty = 6.0$ , skin friction coefficient . . . . .	84
5.18	Flow over an isothermal flat plate at $M_\infty = 6.0$ , Stanton number . . . . .	84
5.19	Computational cost reduction of test cases using LTS . . . . .	85
5.20	Shock wave/boundary layer interaction, numerical setup . . . . .	86
5.21	Shock wave/boundary layer interaction at $M_\infty = 5.0$ , shadowgraph images . . . . .	87
5.22	Shock wave/boundary layer interaction at $M_\infty = 5.0$ , static wall pressure distribution . . . . .	88
5.23	Shock wave/boundary layer interaction at $M_\infty = 5.0$ , skin friction coefficient . . . . .	88
5.24	Shock wave/boundary layer interaction at $M_\infty = 5.0$ , Stanton number . . . . .	89

5.25 Shock wave/boundary layer interaction at $M_\infty = 5.0$ , boundary layer profiles downstream of the shock impact location . . . . .	90
5.26 ITLR model combustor, numerical domain . . . . .	93
5.27 ITLR model combustor (2D), static wall pressure for $M = 2.0$ . .	94
5.28 ITLR model combustor (2D), static wall pressure for $M = 2.5$ . .	95
5.29 ITLR model combustor (2D), flow profiles for $M = 2.0$ . . . . .	96
5.30 ITLR model combustor (2D), flow profiles for $M = 2.5$ . . . . .	97
5.31 ITLR model combustor, composite of numerical and experimental schlieren images at $T_t = 390$ K . . . . .	99
5.32 ITLR model combustor, composite of focusing schlieren and numerical schlieren images ( $\partial\rho/\partial z$ ) at $M = 2.5$ and $T_t = 1300$ K . . . . .	100
5.33 ITLR model combustor (3D), static wall pressure for $M = 2.0$ . .	101
5.34 ITLR model combustor (3D), static wall pressure for $M = 2.5$ . .	102
5.35 ITLR model combustor (3D), flow profiles for $M = 2.0$ . . . . .	103
5.36 ITLR model combustor (3D), flow profiles for $M = 2.5$ . . . . .	104
6.1 Numerical domain . . . . .	109
6.2 Static temperature distribution at the domain inlet for different flow conditions . . . . .	110
6.3 Experimental schlieren images of the flow field downstream of the uncooled and the air-cooled injector . . . . .	112
6.4 Static wall pressure along the top wall, $T_t = 500$ K . . . . .	113
6.5 Mach number distribution of the external flow, $T_t = 500$ K . . .	114
6.6 Comparison of numerical simulations and LITA measurements upstream and downstream of the strut, $T_t = 500$ K . . . . .	116
6.7 Top view of the internal air flow, $T_t = 500$ K . . . . .	118
6.8 Computed area-specific air mass flux along the horizontal center line of the injection ports, $T_t = 500$ K . . . . .	119
6.9 Influence of the total flow temperature on the dimensionless surface temperature, experimental data for the uncooled and the air-cooled injector . . . . .	120
6.10 Influence of the total flow temperature on the dimensionless surface temperature, comparison of experimental and numerical data . .	122
6.11 Mach number distribution of the external flow and injector surface temperature, $T_t = 500$ K . . . . .	123
6.12 Influence of the coolant medium on the dimensionless surface temperature, $T_t = 500$ K . . . . .	125
6.13 Influence of the coolant medium on the numerical surface temperature, $T_t = 500$ K . . . . .	125
6.14 Influence of the injector material on the dimensionless surface temperature, $T_t = 500$ K . . . . .	126

## List of Figures

---

6.15	Mach number distribution of the external flow, $T_t = 1300$ K . . .	128
6.16	Static wall pressure along the top wall, $T_t = 1300$ K . . . . .	129
6.17	Top view of the internal flow field, $T_t = 1300$ K . . . . .	130
6.18	Injector surface temperature, $T_t = 1300$ K . . . . .	132
6.19	Mach number distribution of the external flow and injector surface temperature, uncooled injector, $T_t = 1300$ K . . . . .	133
6.20	Evaluation positions along the injector surface . . . . .	133
6.21	Temperature and Stanton number distribution at the injector top surface in $x$ -direction, $T_t = 1300$ K . . . . .	134
6.22	Temperature and Stanton number distribution at the injector top surface (upstream half) in $y$ -direction, $T_t = 1300$ K . . . . .	136
6.23	Temperature and Stanton number distribution at the injector top surface (downstream half) in $y$ -direction, $T_t = 1300$ K . . . . .	137
6.24	Injector temperature, $T_t = 1300$ K . . . . .	138
6.25	Hydrogen-cooled strut at different combustor wall temperatures, $T_t = 1300$ K . . . . .	140
6.26	Composite of the numerical surface temperature and an injector used during combustion experiments . . . . .	141
C.1	Relative uncertainty of $\Theta$ . . . . .	172
C.2	Influence of the injector material on the dimensionless surface temperature, $T_t = 400$ K . . . . .	173
D.1	Strong scaling of <i>scramjetFoam</i> on Cray XC40 at HLRS . . . . .	176

---

## List of Tables

---

2.1	Parameters for Sutherland's law . . . . .	24
2.2	Species Schmidt numbers . . . . .	26
3.1	Overview of the experimental conditions for the main air flow . . . . .	39
4.1	Major development steps of <i>scramjetFoam</i> . . . . .	62
4.2	Adapted OpenFOAM tools . . . . .	66
5.1	Flow over 15°-wedge, boundary conditions . . . . .	69
5.2	Flow over adiabatic flat plate at $M_\infty = 2.0$ , boundary conditions . . . . .	73
5.3	Flow over adiabatic flat plate at $M_\infty = 4.5$ , boundary conditions . . . . .	78
5.4	Flow over isothermal flat plate at $M_\infty = 6.0$ , boundary conditions . . . . .	83
5.5	Shock wave/boundary layer interaction at $M_\infty = 5.0$ , boundary conditions . . . . .	86
5.6	Shock wave/boundary layer interaction at $M_\infty = 5.0$ , boundary layer thickness $\delta$ at selected cross sections . . . . .	91
5.7	Overview of numerical simulations for the ITLR model combustor . . . . .	92
5.8	Inlet conditions for ITLR model combustor . . . . .	93
6.1	Overview of investigated cases for strut injector . . . . .	108
6.2	Properties of the investigated coolants at $T = 300$ K . . . . .	111
6.3	Heat flux balance at the strut, $T_t = 1300$ K . . . . .	139
D.1	Data for the strong scaling test at HLRS . . . . .	176



---

## List of Symbols

---

### Latin Characters

Symbol	Description	Unit
$A$	cross section	$\text{m}^2$
$a$	speed of sound	$\text{m/s}$
$c$	specific heat capacity	$\text{J}/(\text{kg K})$
$D$	mass diffusivity	$\text{m}^2/\text{s}$
$d$	diameter	$\text{m}$
$e$	specific internal energy	$\text{J}/\text{kg}$
$F$	force	$\text{N}$
$g$	gravitational acceleration	$\text{m}/\text{s}^2$
$f$	focal length	$\text{m}$
$H$	enthalpy	$\text{J}$
$h$	heat transfer coefficient	$\text{W}/(\text{m}^2 \text{K})$
$h$	specific enthalpy	$\text{J}/\text{kg}$
$h_c$	heat of formation	$\text{J}/\text{kg}$
$I$	radiation intensity	$\text{W}/\text{m}^2$
$I$	turbulence intensity	—
$I_{sp}$	specific impulse	$\text{s}$

## List of Symbols

Symbol	Description	Unit
$j$	diffusion mass flux	$\text{kg}/(\text{m}^2 \text{ s})$
$k$	turbulent kinetic energy	$\text{m}^2/\text{s}^2$
$M$	molecular mass	$\text{g}/\text{mol}$
$\dot{m}$	mass flow rate	$\text{kg}/\text{s}$
$p$	pressure	$\text{Pa}$
$\dot{Q}$	heat flux	$\text{W}$
$\dot{q}$	heat flux density	$\text{W}/\text{m}^2$
$\dot{q}_v$	volumetric heat source	$\text{W}/\text{m}^3$
$R$	specific gas constant	$\text{J}/(\text{kg K})$
$R_m$	universal gas constant	$\text{J}/(\text{mol K})$
$r$	recovery factor	—
$S$	surface	$\text{m}^2$
$T$	temperature	$\text{K}$
$t$	time	$\text{s}$
$u$	velocity	$\text{m}/\text{s}$
$V$	volume	$\text{m}^3$
$\dot{V}$	volume flow rate	$\text{m}^3/\text{s}$
$Y$	species mass fraction	—

## Greek Characters

Symbol	Description	Unit
$\alpha$	thermal diffusivity	$\text{m}^2/\text{s}$
$\Gamma$	blending factor	—
$\gamma$	heat capacity ratio	—
$\delta$	boundary layer thickness	$\text{m}$
$\delta_{ij}$	Kronecker delta	—
$\varepsilon$	turbulence dissipation rate	$\text{m}^2/\text{s}^3$
$\epsilon$	emissivity	—
$\Theta$	dimensionless temperature	—
$\lambda$	thermal conductivity	$\text{W}/(\text{m K})$
$\mu$	dynamic viscosity	$\text{kg}/(\text{m s})$
$\nu$	kinematic viscosity (momentum diffusivity)	$\text{m}^2/\text{s}$
$\rho$	density	$\text{kg}/\text{m}^3$
$\sigma$	standard deviation	—

---

## List of Symbols

---

Symbol	Description	Unit
$\tau_{ii}$	normal stress	N/m <sup>2</sup>
$\tau_{ij}$	shear stress	N/m <sup>2</sup>
$\omega$	specific turbulence dissipation rate	1/s

---

## Subscripts

---

Symbol	Description
$\infty$	free-stream conditions
<i>ad</i>	adiabatic
<i>eff</i>	effective
<i>ex</i>	exhaust
<i>f</i>	fluid
<i>e</i>	boundary layer edge
<i>i</i>	internal flow
<i>l</i>	laminar
<i>max</i>	maximum value
<i>min</i>	minimum value
<i>p</i>	at constant pressure
<i>ref</i>	reference value
<i>s</i>	static conditions
<i>t</i>	stagnation conditions
<i>t</i>	turbulent
<i>uc</i>	uncooled
<i>v</i>	at constant volume
<i>visc</i>	viscous
<i>w</i>	wall

---

## Superscripts

---

Symbol	Description
—	averaged quantity
*	critical cross-section

---

## List of Symbols

---

Symbol	Description
$\sim$	Favre mean
'	fluctuating quantity
"	Favre fluctuation
+	dimensionless wall-normal quantity

---

## Dimensionless Quantities

Symbol	Description	Definition
$C$	Courant-Friedrichs-Lewy number	$C = (u + a) \Delta t / \Delta x$
$Fo$	Fourier number	$Fo = \alpha \Delta t / \Delta x^2$
$M$	Mach number	$M = u/a$
$Pe$	Peclet number	$Pe = RePr = uL/\alpha$
$Pr$	Prandtl number	$Pr = \nu/\alpha$
$Re$	Reynolds number	$Re = uL/\nu$
$Sc$	Schmidt number	$Sc = \nu/D$
$St$	Stanton number	$St = \dot{q}/(\rho u c_p \Delta T)$

---

## Abbreviations

Abbreviation	Description
CFD	Computational Fluid Dynamics
CFL	Courant-Friedrichs-Lewy
DFG	German Research Foundation
DLR	German Aerospace Center
DNS	Direct Numerical Simulation
DSTO	Defence Science and Technology Organisation
HEXAFly	High-Speed Experimental Fly Vehicles
HIFiRE	Hypersonic International Flight Research Experimentation Program
HLLC	Harten-Lax-van-Leer-Contact
HLRS	High Performance Computing Center Stuttgart
ITAM	Khristianovich Institute of Theoretical and Applied Mechanics

---

---

## List of Symbols

---

Abbreviation	Description
ITLR	Institute of Aerospace Thermodynamics
JANAF	Joint Army-Navy-Air Force
JAPHAR	Joint Airbreathing Propulsion for Hypersonic Application Research
JAXA	Japan Aerospace Exploration Agency
LAPCAT	Long-term Advanced Propulsion Concepts and Technologies
LITA	Laser-Induced Thermal Acoustics
LES	Large Eddy Simulation
LTS	Local Time-Stepping
NASA	National Aeronautics and Space Administration
NPARC	National Program for Application-Oriented Research in CFD
ONERA	Office National d'Études et de Recherches Aérospatiales
OpenFOAM	Open Field Operation and Manipulation
PREPHA	Programme de Recherche et de Technologie sur la Propulsion Hypersonique Avancée
RANS	Reynolds-Averaged Navier-Stokes
RBCC	Rocket-Based Combined Cycle
SCRJ	ScramjetFoam
SEP	Société Européenne de Propulsion
SST	Shear-Stress Transport
SSTO	Single-Stage-To-Orbit
TBCC	Turbo-Based Combined Cycle
TSTO	Two-Stage-To-Orbit
TVD	Total Variation Diminishing

---



---

## Abstract

---

For future aviation or space transportation systems, scramjets could provide a complement or even an alternative to conventional propulsion systems. In aviation, scramjets would considerably reduce travel times due to the high flight Mach number. For space transportation, the integration of a scramjet-based stage would imply a gross weight reduction compared to a rocket, as scramjets are able to take the oxidizer out of the ambient atmosphere instead of carrying it on board. This would increase the payload mass and thus reduce operational costs. However, due to the high-enthalpy flow environment, scramjet development still implies considerable technical challenges.

Besides aerodynamics and the development of high temperature materials, one of the most relevant issues is the need for an efficient fuel injection and mixing system. It has to guarantee a stable and reliable combustion process, as the flow residence time inside the engine is only in the order of several milliseconds. Strut-based injection systems have proven to be a suitable choice due to their ability to provide fuel directly into the center of the flow. In contrast to wall-based injection systems, however, struts are exposed to the complete aerodynamic heat loads of the flow, which necessitates active cooling to avoid structural damages. As experimental facilities are hardly able to reproduce flight conditions over a long period of time, a numerical approach is inevitable to assess the heat loads onto a strut and to evaluate the internal cooling mechanism.

Within the present thesis, a numerical solver for the conjugate simulation of heat transfer in supersonic flows was developed and integrated into the OpenFOAM software package. A thorough validation for a variety of data from

## Abstract

---

both literature and in-house studies was conducted. The accurate prediction of different phenomena relevant for supersonic flows could be verified. The new solver was then applied to the evaluation of an internally cooled lobed strut injector. In a first step, the injector was investigated at moderate flow conditions. Experimental data for different flow temperatures and coolants was obtained using infrared thermography of the injector surface. A comparison to numerical simulations led to the identification of characteristic well and poorly cooled zones along the injector surface, which could be explained by features of either the external or the internal flow field.

Finally, the lobed strut injector was studied numerically at hot gas conditions representative for the ITLR model combustor, where no experimental data of the surface is available. Besides the leading edge, a second hot zone was identified towards the trailing edge of the strut, which was attributed to the impact of the reflected leading edge shock wave onto the surface. Activation of internal air cooling was found to lower the general temperature level as expected, but to have only a small effect on the leading edge. Instead, heat conduction towards the cooled combustor side walls provided a considerable part of the cooling in this area. Switching to hydrogen as coolant led to a further reduction of the injector temperature at a considerably lower coolant mass flux, without changing the overall characteristics of the cooled injector. Changing to more realistic, hotter combustor side walls for a hydrogen-cooled strut caused a generally higher injector surface temperature. While the hottest injector regions were found to be near the side walls, the leading edge could still be partially cooled by the internal hydrogen flow.

---

## Kurzfassung

---

Im Hinblick auf zukünftige Luftfahrtkonzepte und Raumtransportsysteme stellen Überschall-Staustrahlantriebe eine vielversprechende Ergänzung oder sogar eine Alternative zu herkömmlichen Antriebssystemen dar. Im Bereich der Luftfahrt könnten die Reisezeiten durch die höhere Fluggeschwindigkeit eines Staustrahlantriebs mit Überschallverbrennung deutlich reduziert werden. Der Einsatz eines solchen Antriebs als Stufe eines Raumtransportsystems könnte zudem die mögliche Nutzlast im Vergleich zu Raketen deutlich erhöhen, da der für die Verbrennung notwendige Oxidator direkt aus der Umgebungsluft gewonnen werden kann. Dies würde gleichzeitig eine Senkung der Betriebskosten bedeuten. Aufgrund der vorliegenden Hochenthalpieströmungen stellt die Entwicklung eines solchen Staustrahlantriebs jedoch nach wie vor eine technische Herausforderung dar.

Neben der Aerodynamik und der Entwicklung von Hochtemperaturmaterialien ist die effiziente Einbringung und Vermischung des Treibstoffs eines der Hauptprobleme. Trotz der kurzen Aufenthaltszeit der Strömung innerhalb der Brennkammer von nur wenigen Millisekunden muss eine stabile Verbrennung gewährleistet werden. Eine vielversprechende Möglichkeit ist dabei der Einsatz von sogenannten Zentralkörpern, mit deren Hilfe der Treibstoff direkt in die Mitte der Strömung eingebracht werden kann. Im Gegensatz zu wandgebundenen Injektionssystemen sind Zentralkörper dadurch aber auch den vollständigen Wärmelasten der auftreffenden Strömung ausgesetzt, was in der Regel eine aktive Kühlung des Bauteils erfordert. Da experimentelle Anlagen jedoch kaum in der Lage sind, realistische Strömungsbedingungen über eine ausreichend

lange Zeit zur Verfügung zu stellen, ist eine numerische Untersuchung zur Beurteilung der Wärmelasten und der Kühlmechanismen unumgänglich.

Im Rahmen der vorliegenden Arbeit wurde ein numerischer Löser für die konjugierte Simulation von Wärmeübergängen in Überschallströmungen entwickelt und in das Software-Paket OpenFOAM integriert. Dieser Löser wurde sowohl anhand verschiedener Testfälle aus der Literatur als auch basierend auf Experimenten, die am ITLR durchgeführt wurden, validiert. Dabei konnte die korrekte Wiedergabe relevanter Strömungsphänomene nachgewiesen werden. Im Anschluss wurde der Löser zur Untersuchung eines innengekühlten Zentralkörpers eingesetzt. Im ersten Schritt wurde der Einfluss verschiedener Strömungstemperaturen und Kühlmedien auf den Injektor bei moderaten Strömungsbedingungen untersucht. Mittels Infrarotthermographie wurden dabei experimentelle Daten der Injektoroberfläche gewonnen. Der Abgleich dieser Daten mit numerischen Simulationen ermöglichte die Identifikation von charakteristischen Zonen mit über- oder unterdurchschnittlicher Kühlung, deren Existenz auf Merkmale der externen und internen Strömungsfelder zurückgeführt werden konnte.

Abschließend wurde der Zentralkörper bei Heißgasbedingungen untersucht. Diese sind repräsentativ für Experimente an der ITLR-Modellbrennkammer, wobei allerdings keine Daten der Injektoroberfläche gewonnen werden können. Neben der Injektorvorderkante konnte durch die Simulationen auch im Bereich der Hinterkante eine erhöhte Oberflächentemperatur nachgewiesen werden, die durch das Auftreffen des an der Wand reflektierten Verdichtungsstoßes der Vorderkante ausgelöst wird. Durch die Aktivierung der internen Luftkühlung konnte das Temperaturniveau an der Oberfläche wie erwartet gesenkt werden, ein signifikanter Einfluss auf die unmittelbare Umgebung der hochbeanspruchten Vorderkante wurde jedoch nicht festgestellt. Stattdessen wird ein Großteil der Kühlleistung in diesem Bereich durch Wärmeleitung in Richtung der gekühlten Brennkammerwände erzeugt. Die Verwendung von Wasserstoff als Kühlmedium ermöglichte eine weitere Absenkung des Temperaturniveaus, ohne jedoch die charakteristischen Eigenschaften des gekühlten Injektors zu verändern. Der Wechsel hin zu einer höheren, realistischeren Wandtemperatur der Brennkammer führte zu einem insgesamt höheren Temperaturniveau auf der Injektoroberfläche. Während die Injektorvorderkante noch teilweise durch den Wasserstoff der Innenströmung gekühlt werden konnte, wiesen die seitlichen Regionen des Injektors für diesen Fall die höchste Oberflächentemperatur auf.

# CHAPTER 1

---

## Introduction

---

It is hard to imagine the world today without aviation and space flight. In such times of globalization and technological progress, the access to fast and efficient long-range transport systems is a vital aspect for both the global economy and – especially in case of space flight – scientific purposes. Thus major goals are to reduce operating costs, enhance efficiency and also to increase the speed of these systems. Plane and rocket engines have been significantly improved over the past decades, and have thus become more fuel-efficient and also more environmentally friendly. However, especially regarding widely-used jet engines such as turboprops, turbofans and turbojets, this optimization nowadays only results in a small increase in effectiveness due to the already very high level of technology. This illustrates the need for new technological approaches to unlock new domains in aerial transport.

Considering space transportation, one of the major drawbacks of current propulsion systems is their small percentage of payload compared to the overall mass of the vehicle. A potential way to allow for a higher payload would be the use of an air-breathing propulsion system for the time the vehicle is still flying inside the Earth's atmosphere. The oxidizer could be taken out of the surrounding atmosphere during this phase of flight. As part of a space transport system the trajectory would include supersonic and hypersonic flight, which

## 1 Introduction

---

eliminates most of the available and highly developed engine technologies. A possible solution is the use of ramjets or supersonic combustion ramjets, short scramjets. Although this approach would still require an additional, supporting propulsion system to accelerate the vehicle up to the regime where a (sc)ramjet can operate efficiently, it could provide a considerable improvement in terms of maximum payload mass. Besides being used as a stage of a space transportation system, scramjets might also drastically reduce travel times when used for civil aviation. However, as scramjet design includes major technological challenges, it has been and still is subject of extensive research.

To illustrate the benefit of ramjet and scramjet systems, a comparison of different engine types and propellants is shown in figure 1.1. Here the specific impulse

$$I_{sp} = \frac{F}{\dot{m}g} = \frac{u_{ex}}{g}, \quad (1.1)$$

which is a measure for both power and fuel efficiency of an engine, is presented depending on flight Mach number. The specific impulse is a suitable quantity to compare jet or rocket engines, as it describes the achievable engine thrust  $F$  per unit propellant flow rate. In case of a rocket engine, it may also be obtained using the exhaust gas velocity  $u_{ex}$ . The flight Mach number is a dimensionless quantity, which describes the ratio of flight speed to the local speed of sound.

The only propulsion system to cover the whole range of Mach numbers is a rocket, but it exhibits a low overall efficiency as can be seen in figure 1.1. Thus it exceeds the performance of air-breathing systems only at very high Mach numbers. For any other vehicle, flying faster than about three times the speed of sound either requires a staged propulsion system or an integrated engine, which combines several of the aforementioned principles. While the subsonic and low supersonic range is usually covered by a turbojet, a ramjet can be used for moderate supersonic speeds before a scramjet takes over at hypersonic Mach numbers. By using a lightweight gas like hydrogen as propellant, the theoretical specific impulse can be increased significantly. However, this raises the issue of storing a fuel with such a low density, which is why hydrogen has hardly been used for air-breathing engines so far [22].

While rockets still are the most common space transportation system, two major approaches exist which at least partly rely on an air-breathing turbojet system. A two-stage-to-orbit (TSTO) system consisting of the air-breathing *WhiteKnightTwo* and its rocket powered upper stage *SpaceShipTwo* is currently undergoing flight tests [23]. A completely different approach is pursued by the *Skyton* vehicle [172], which uses a fully integrated combination of turbojet and

## 1.1 Air-Breathing Supersonic Propulsion Systems

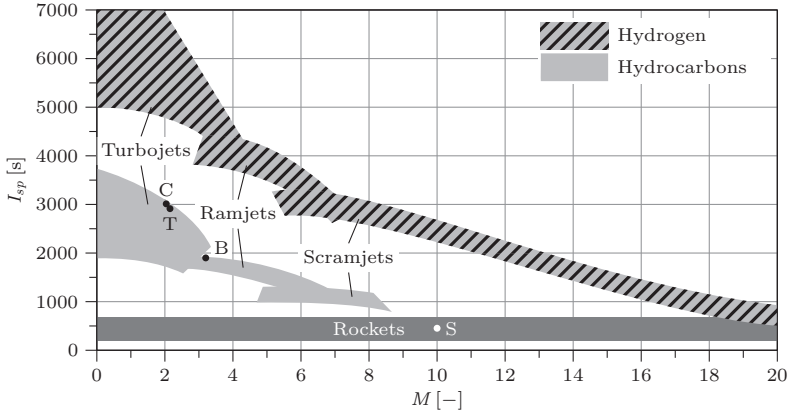


Figure 1.1: Comparison of specific impulses for different propulsion systems, adapted from [142] (B: SR-71 ‘Blackbird’, C: Concorde, S: Space Shuttle Main Engine, T: Tu-144D)

rocket and thus represents a single-stage-to-orbit (SSTO) approach. *Skylon* is still under development with first flights envisioned for 2019. However, both of these systems switch to rocket propulsion at comparably low Mach numbers and do not include a ramjet as one of the subsystems. Currently the application of ramjets as propulsion system is mostly limited to missiles, but significant amounts of research have been and still are conducted to render ramjets and scramjets a suitable alternative to rocket-based systems. Selected research projects will be discussed in more detail in one of the following sections, but first the general principle of an air-breathing engine is introduced.

### 1.1 Air-Breathing Supersonic Propulsion Systems

As mentioned above, turbojets or (sc)ramjets are possible air-breathing propulsion systems for supersonic flight. In order to point out the advantages of ramjets for high flight Mach numbers, first the turbojet has to be discussed briefly. Its thermodynamic principle is based on the Joule cycle as shown in figure 1.2, where the six distinct states correspond to the engine intake (1), the compressor inlet (2), the compressor exit (3), the turbine inlet (4), the turbine exit (5) and the thrust nozzle exit (6). The incoming air is compressed adiabatically inside the inlet and the compressor, which usually features multiple compression stages. In the combustion chamber, heat is added to the

## 1 Introduction

---

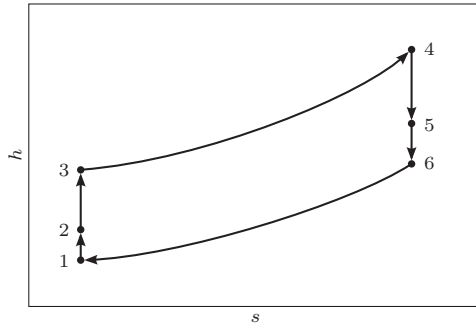


Figure 1.2: Ideal Joule cycle for turbojets

flow by the combustion of fuel. This process is considered isobaric from the thermodynamic point of view. The flow is then expanded adiabatically in the turbine, and major parts of the resulting energy are used to power the compressor unit. Actual thrust is obtained by further expanding the flow in the nozzle.

While operating over a wide range of flight conditions, a turbojet still has to be able to provide the combustion chamber with air at a suitable thermodynamic state. Furthermore, independently of the flight Mach number the air ejected at the nozzle exit is desired to be at ambient pressure to minimize drag. This usually requires a variable nozzle exit section when operating the same engine in both subsonic and supersonic flight, which significantly contributes to the complexity of the system. The operational range of a turbojet is essentially limited by the high stagnation temperatures at increased Mach numbers. The compressor blades are no longer able to withstand these temperatures above approximately Mach 3. At these high flight Mach numbers, the air can be compressed more efficiently and without any rotating machinery by simply exploiting compression shocks. This represents the functional principle of the ramjet engine.

Turbojet engines have been successfully used for only two supersonic, commercial airliners in the past. The final version of the Russian Tupolev Tu-144 was powered by four Kolesov RD-36-51 turbojets, which allowed supersonic cruise at Mach 2.15. However, the Tu-144 only was in active service for several months. Its European counterpart Concorde, although slightly slower, considerably surpassed the Russian airliner in range and remained in commercial service for over 27 years, thus rendering it the only successful supersonic passenger

## 1.1 Air-Breathing Supersonic Propulsion Systems

aircraft. Concorde was powered by Rolls-Royce/Snecma Olympus 593 turbojet engines and operated at Mach 2.04 during cruise. Although turbojets are far more efficient, it is interesting to note that the actual speed record for a civil airliner of Mach 2.29 was obtained by a Tu-144 operating Kuznetsov NK-144 turbfans with constant use of the afterburner.

Sustained flight of a manned, air-breathing aircraft at even higher Mach numbers has only been achieved by the SR-71 'Blackbird', which reached Mach 3.53 in 1976. However, this could not be realized using a pure turbojet. Combined turbojet/ramjet engines manufactured by Pratt & Whitney were installed instead. At about Mach 2 the engine switched from turbojet to combined turbojet/ramjet operation using a variable internal flow path. The specific impulses of these turbojet based engines are also shown in figure 1.1. As can be seen, the combined turbo-ramjet cycle of the SR-71 delivers a considerably lower  $I_{sp}$  compared to the pure turbojets, but significantly increases the maximum flight Mach number.

### 1.1.1 Ramjet

The ramjet is based upon the Brayton cycle as depicted in figure 1.3. It consists of a set of four thermodynamic changes of state, each of which again corresponds to a specific part of the engine. These changes of state are thermodynamically identical to those present in a turbojet engine, but the technical implementation is completely different in a ramjet due to the higher air speed and the absence of rotating parts. To maintain comparability to turbojets, the relevant thermodynamic states are numbered identically.

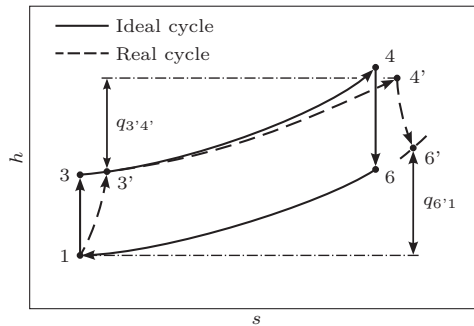


Figure 1.3: Ideal and real Brayton cycle for ramjets

## 1 Introduction

---



Figure 1.4: Schematic of a ramjet

The incoming air (1) is compressed adiabatically in the engine intake. In case of supersonic flight Mach numbers, this is usually achieved by means of several oblique shocks and a final normal shock. The compressed and decelerated air is then led through the isolator duct towards the combustor inlet (3) at high subsonic speed. The isolator is intended to prevent any pressure gradients originating in the combustion chamber from propagating upstream and possibly causing an inlet unstart. Inside the combustion chamber (3 – 4) fuel is injected, mixed and burned at subsonic speed. The heat release due to the combustion is again assumed to be isobaric. It causes a significant increase in temperature and specific enthalpy. The flow is then re-accelerated to supersonic speed by a convergent-divergent geometrical nozzle and expanded adiabatically in the thrust nozzle (4 – 6) before being ejected into ambient again. A sketch of the complete ramjet engine with an indication of subsonic and supersonic flow regions is shown in figure 1.4.

In reality, however, each one of the theoretically ideal thermodynamic processes is subject to losses as also pictured in figure 1.3. These losses can either be caused by viscous effects such as friction and boundary layers, or by thermal effects. Furthermore, the combustion process itself is not ideal, which leads to a lower heat addition  $q_{3'4'}$  than theoretically possible. To reduce skin friction, the thrust nozzle is often truncated, which results in an underexpanded exhaust flow. This causes the flow to exit the nozzle with a higher remaining heat  $q_{6'1}$  and thus reduces thrust, as the amount of enthalpy converted into kinetic energy is diminished.

The standard operating regime for a ramjet engine are flight Mach numbers of 2 to 5. At higher Mach numbers, the deceleration of the flow to subsonic speed by means of a normal shock causes a significantly higher total pressure loss, high static pressures inside the engine and also high thermal loads onto the engine structure. Furthermore, the increase in static temperatures results in dissociation of the flow inside the duct, which leads to additional losses. Ramjet engines have been successfully used in the past for missile systems and – in rare cases – also airplanes. However, as mentioned above, they still exhibit the inherent problem of only being functional at reasonably high airspeed.

### 1.1.2 Dual-mode Ram/Scramjet

At Mach numbers of 5 to 7, the transition regime from ramjet to pure scramjet can be bridged using dual-mode operation of the engine. Instead of the distinct normal shock at the isolator inlet, a pre-combustion shock train in the isolator decelerates the flow to subsonic speed when flying at lower Mach numbers. This shock train is caused by the high static pressure inside the combustor and diminishes in strength with increasing flight Mach number. When approaching the scramjet regime, at first a supersonic core flow is created, before the shock train vanishes completely and the engine operates in scramjet mode.

A schematic of such a dual-mode engine geometry and the internal shock system is presented in figure 1.5. The most notable difference to a pure ramjet is the absence of a geometrical throat at the exit of the combustion chamber. Acceleration to supersonic velocities is instead achieved by a thermal throat, which is created by the heat addition during combustion. Similar to the pre-combustion shock train in the isolator, the thermal throat vanishes at higher flight Mach numbers and thereby enables a supersonic flow throughout the duct.

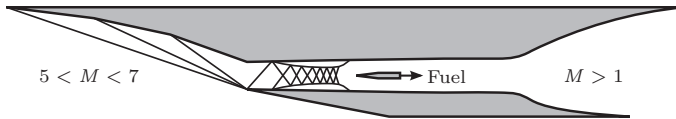


Figure 1.5: Schematic of a dual-mode ram/scramjet

Although a dual-mode engine may be desirable due to the ability to operate over a wider range of Mach numbers, the engine design is very challenging and in most cases requires a moveable engine geometry to allow adaption to the range of flight conditions. Especially the positioning of the thermal throat by controlling the heat release and ensuring a stable combustion over the whole operational range are topics of ongoing research.

### 1.1.3 Scramjet

At flight Mach numbers above 7, the losses due to flow deceleration to subsonic velocities would be unreasonably high. Therefore, in pure scramjet mode the main flow remains supersonic throughout the entire engine duct and also during combustion itself. This renders any kind of geometrical or thermal

## 1 Introduction

---

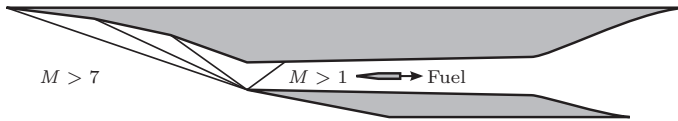


Figure 1.6: Schematic of a scramjet

throats unnecessary. The resulting engine geometry and the corresponding shock system are shown in figure 1.6.

However, the high velocities in the duct imply additional challenges. Firstly, any kind of stagnation point inside the engine is exposed to very high static temperatures. This applies to fuel injectors as well as to the engine walls themselves, and thus either thermal protection or active cooling systems are required. Secondly, the short residence time of the flow inside the combustor requires efficient and fast fuel injection and mixing to ensure a stable operation of the engine. Both these issues lead to the central aspect of the present thesis.

In contrast to ramjets, which have been in active use for more than fifty years by now, scramjet engines are still in the stage of testing at model level and will probably remain so for several years, if not decades. Fundamental research is still ongoing regarding aerodynamics, thermodynamics and also materials suitable for this kind of jet engine. Therefore, the next section is intended to provide a brief overview of past and current research in this field.

### 1.2 State of Knowledge

The theoretical idea of subsonic ramjet propulsion as originally proposed by René Lorin [96] has existed for over one hundred years now. However, technological challenges and World War I significantly delayed the practical implementation. The construction and testing of such engines only started in the 1930s mainly in France, Russia and Germany, and later also in the United States and Great Britain. An extensive historical overview covering the last century of ramjet development is provided by Fry [53]. While being restricted to subsonic Mach numbers at first, the application of ramjet engines was quickly extended to cover supersonic flight.

The idea of supersonic combustion was suggested by Roy [134], who proposed a detonation wave to achieve ignition of the fuel. Some years later Ferri [47, 48] stated that combustion could also be achieved by diffusion of the fuel. However, even fifty years after these initial considerations, the realization of

stable supersonic combustion for a flying vehicle remains a very challenging topic. Successful flight experiments are scarce and usually only feature a duration of a few minutes at most. In the following, a selective overview of major research programs realized within the past decades is given. Relevant fuel injection concepts will be discussed subsequently, with a focus on strut injectors.

### 1.2.1 Selected Research Programs

The first detailed investigations of scramjet technology were concentrated in only a few countries, namely France, Russia, Germany and the United States. Since that time additional countries such as Australia, Japan, Great Britain and lately also China and India developed own research programs or joined already existing ones. Due to the complexity and the enormous costs especially regarding flight experiments, by now multi-national programs are predominant when considering civil research projects. The programs selected for a discussion in more detail are chosen based on their significance for the respective national research. A more complete overview has been compiled by Curran [30].

#### Sänger II

Named after Austrian aerospace engineer Eugen Sänger, the Sänger II vehicle was designed as a TSTO concept and was envisioned to considerably reduce the costs of payload transportation into orbit [84]. As part of the German Hypersonic Research Program, it was essentially based on the Sänger concept, which had been designed in Germany until 1974. The first stage featured a turbo-ramjet engine and was intended to take off and land horizontally using an ordinary airport runway. Pure ramjet operation would begin at Mach 3, while the maximum flight Mach number of 6.8 was to be reached at an altitude of 31 km shortly before stage separation at 37 km altitude [85]. The rocket-based upper stage would then deliver approximately 7 t of payload or 3 t and several passengers into lower Earth orbit [185], before returning to Earth similar to the Space Shuttle.

The major technological challenges during the Sänger II project were the propulsion system and its integration into the aircraft, as well as the thermal management of the engine. A fully integrated combination of turbojet and ramjet was originally considered for the first stage vehicle. However, due to lower complexity the final concept included a co-axial engine configuration, where both engine types only shared the inlet and the thrust nozzle. A boundary

## 1 Introduction

---

layer bleed ending in a separate duct was projected to be installed upstream of the engine inlet to avoid thick boundary layers inside the engine during turbojet operation [92]. Apart from the engine section, active cooling of the first stage vehicle body was not considered necessary [185], critical sections were to be manufactured out of ceramic matrix composite materials instead.

After the Sanger II program was discontinued in 1995, efforts were subsequently joined with France during the JAPHAR project. Fundamental component research was also continued within the frame of three collaborative research centers (SFB 253, 255 and 259) located at several German universities [35].

### PREPHA

The French PREPHA (Programme de Recherche et de Technologie sur la Propulsion Hypersonique Avanc ee) program combined efforts of both civil and military research institutions [136]. The program started in 1992 and was aimed at obtaining first experiences in the area of scramjet technology. For this purpose, the design of an entire engine including all relevant components was envisioned. Also new ground test facilities were to be developed. However, a full-scale scramjet ground test at realistic conditions still is impossible, therefore a combined experimental and numerical approach was pursued. Furthermore, also material and system studies were included in the scope of the program [33]. The work packages were distributed between the main project contributors Aerospatiale, Dassault Aviation, SEP, Snecma and ONERA [45].

Different concepts were assessed regarding the combustion chamber, most of which were based on strut injection. Investigations also included staged fuel injection by means of several struts distributed along the combustor. Due to the high thermal loads onto the struts, an internal cooling mechanism using the fuel as coolant was pursued as described by Ren -Corail et al. [128]. Cooling bores were introduced along the strut leading edge, which is the most stressed part of the injector. A summary of the combustion test results is provided by Bouchez et al. [13] and Rothmund et al. [133].

### JAPHAR

Combining the findings of Sanger II and PREPHA led to a French-German cooperation named JAPHAR (Joint Air-Breathing Propulsion for Hypersonic Application Research), which included ONERA and DLR [119]. Lasting from 1997 to 2001, the project was focused on the development of a dual-mode

ramjet. While ONERA contributed the engine developed during PREPHA, DLR could resort to basic research and the component tests conducted within the collaborative research centers [35] following Sanger II. The target flight Mach number was planned to be between 4 and 8. Regarding the combustion inside the engine, this corresponds to the typical dual-mode and the lower supersonic regime.

The JAPHAR project included a variety of work packages, such as design studies [42], the investigation of the aerodynamic performance [40] and combustion tests conducted at ONERA [34]. Based on the results of PREPHA, the combustor and injection concept consisted of a two-staged strut configuration fueled by hydrogen. The experiments proved that this staged injection scheme was able to meet the demands for a stable combustion over a wide operational range.

### Hyper-X

Several flight tests of scramjet engines have been conducted within NASA's Hyper-X program, which was started in 1996 by the United States. Aimed at providing key technologies for a more economic access to space, flight demonstrations of a scramjet were the main objective of this project [116]. After an initial failure due to booster malfunction in 2001, two successful flights of the X-43A vehicle were finally achieved in 2004. The vehicle was released from a B-52 aircraft and accelerated by a Pegasus rocket, before the scramjet engine started to operate. While during the first flight a maximum Mach number of 6.83 was reached for 11 seconds, the second flight resulted in a new speed record for air-breathing engines of  $M = 9.68$ . A controlled crash of the vehicle into the Pacific Ocean was executed afterwards. The critical leading edges were cooled by circulating water during flight [102]. Selected results of the flight tests, during which both hydrogen and hydrocarbons were tested as fuel, have been published [6, 31, 108, 177].

Since 2006, the X-51A 'Waverider' has succeeded the X-43A [94]. It is fueled by JP7, which is a hydrocarbon jet propellant developed by the U.S. Air Force and had already been used for the integrated turbojet/ramjet engines of the SR-71 'Blackbird' [111]. The vehicle was first tested on ground, before a successful flight at approximately Mach 5 was realized in 2010. An acceleration system similar to the one of the X-43A flight tests was used prior to scramjet operation. Two consecutive flights then failed, one in June 2011 due to an inlet unstart and the other one fourteen months later due to loss of control caused by an unlocked fin. A fourth flight was conducted in 2013, where the vehicle achieved

## 1 Introduction

---

210 seconds of propelled flight at Mach 5.1 [132]. However, it has to be noted that the low Mach number of the X-51A flights corresponds to dual-mode rather than to pure scramjet operation as was achieved by the X-43A.

### HyShot

Led by the University of Queensland (UQ), the HyShot program [124] represented a low-cost approach to scramjet flight testing. Carried by a commercial Terrier-Orion sounding rocket, the vehicle was sent onto a parabolic flight trajectory and reached the Mach numbers necessary for engine testing during the reentry phase. This allowed for test times of approximately 10 seconds at a Mach number around 7.5.

Four flight experiments were realized between 2001 and 2007, and during two of the flights actual scramjet operation was achieved [15, 20, 144]. Additional ground experiments involving DLR and JAXA were carried out in parallel with the flight tests. Experiments were mostly conducted in the T4 wind tunnel at UQ and in the high-enthalpy shock tunnel at DLR Göttingen. Selected results of these test campaigns have been published by Gardner et al. [57], Martinez-Schramm et al. [103] and Hannemann et al. [69].

Several successive projects evolved out of the HyShot program. The most notable one is probably HIFiRE [191], which was realized by DSTO in cooperation with NASA, the U.S. Air Force and other partners. Besides supplementary ground tests [97, 179], several flight experiments have been successfully conducted between 2009 and 2015 [80, 82, 146]. The remaining HyShot flights V, VI and VII have also been included in HIFiRE. The most challenging one will be HyShot VII, where a scramjet-powered and self-sustained flight at Mach 8 for up to one minute is projected. During HyCAUSE [181, 182], flight tests were carried out at a flight Mach number of 10.

In 2013, the Scramspace [16, 164] flight test failed due to a malfunction of the first stage rocket motor. However, the ascent phase still allowed for gathering of aerothermal and structural data of the vehicle.

### LAPCAT

The first phase of the Long-term Advanced Propulsion Concepts and Technologies (LAPCAT) project was initiated by the European Union in 2005 in an attempt to coordinate research conducted at institutions all over Europe [148, 150]. The main goal was the design of a supersonic airliner, which was intended

to cover the distance between Brussels and Sydney in about two to four hours. Design studies resulted in the finding that this ambitious objective could only be achieved using an engine concept either employing a turbo-based combined cycle (TBCC) or a rocket-based combined cycle (RBCC) [149]. Furthermore, aspects regarding numerical combustion modeling, fuel injection systems and overall performance of the vehicle were investigated. After the end of the first phase, the project was extended by a second, four-year phase in 2008 [152]. The findings of the first phase were pursued further on both vehicle and component level. Two vehicles were investigated in detail, a Mach 5 version based on a TBCC and an aircraft designed for cruise at Mach 8 [151]. In addition to a system analysis of the vehicles, also ground tests covering supersonic combustion were carried out at different experimental facilities to identify the effects of test gas vitiation on ignition and combustion processes. In 2014, a free-flying model of the Mach 8 vehicle including a fully-functional propulsion system was tested at DLR Göttingen to demonstrate the functionality of the concept on a small scale [104].

The Mach 8 vehicle developed in LAPCAT is further investigated within the HEXAFLY program [152]. In the first phase, the foundations for a future flight experiment were laid and a stable, controllable version of the vehicle was designed [125]. During a second, international phase of HEXAFLY the actual flight experiment is to be conducted in cooperation with partners in Russia and Australia.

### **Research Training Group GRK 1095**

The German Research Training Group GRK 1095 ‘Aero-Thermodynamic Design of a Scramjet Propulsion System for Future Space Transportation Systems’ was started in 2005 and lasted until 2014 [184]. The program included partners at the University of Stuttgart, the Technical University of Munich, RWTH Aachen University and the DLR Cologne. The main goal of the project was the conceptual design of a scramjet demonstrator, which was intended to operate at a flight Mach number of 8 and a cruise altitude of 32 km. As a complete vehicle represents a highly non-linear system, the close cooperation of the single work packages, which were processed in the framework of PhD theses and postdoctoral studies, was considered a major aspect.

The work packages covered all relevant parts of the vehicle, such as the inlet geometry, the combustion chamber with the fuel injection concept and the thrust nozzle design [55]. A combination of numerical and experimental studies was chosen to investigate the different scramjet elements. The

## 1 Introduction

---

various numerical codes and different experimental test rigs available at the collaborating institutions enabled a thorough study of the single components and their interaction. Additional combustion experiments were conducted at the Khristianovich Institute of Theoretical and Applied Mechanics (ITAM) in Novosibirsk, where a hypersonic wind tunnel for even higher flow enthalpies than at the other institutions was available [56].

Parts of the experimental and numerical investigation of the scramjet combustor and the fuel injection concept were carried out at the Institute of Aerospace Thermodynamics (ITLR) in Stuttgart, where also the research for the present thesis has been conducted. During preceding studies, a staged fuel injection scheme was identified to be the most promising and stable approach [138, 176]. A lobed strut injector, which is described in more detail in section 3.1.3, was chosen as first injection stage, while the second stage was designed to be a wall-bound ramp configuration. However, while enabling stable and efficient combustion of the fuel, the thermal management of the strut injector remained an open issue. Although it is internally cooled by the fuel, a quantification of the thermal loads could not be achieved experimentally. Thus the need for a numerical approach arose, which should include both the combustor flow field and the solid injector structure. This subject will be covered in the present thesis.

### 1.2.2 Fuel Injection Concepts

A stable and reliable combustion process at high flight Mach numbers is one of the major objectives for any scramjet engine. For this reason, a wide range of studies regarding an efficient fuel injection concept is available in literature. Many investigations focus on injection via port holes or ramps located at the combustion chamber walls [3, 66, 91], which inject the fuel into the main flow at a suitable angle. Often additional geometrical features like cavities are introduced to enhance flame-stabilization and provide high static temperatures, which are favorable for ignition [79, 183, 194]. Several wall injection ports and cavities can also be combined to realize a staged fuel injection with flame-holding, as has been investigated during HIFiRE by Cabell et al. [19]. Wall injection in general is not only advantageous in terms of a simple implementation, it also avoids the introduction of any drag-inducing obstacles into the main combustor flow.

However, the main drawback of any wall-bound injection scheme is the need for a high jet momentum to achieve a sufficient penetration depth and mixing of the fuel. Especially at high flight Mach numbers, a reasonable penetration

depth can only be realized by using perpendicular injection and thus accepting a severe pressure loss due to the blockage effect of the fuel jet. At the same time, however, the fuel injection angle should approach coaxial at high Mach numbers to obtain optimum thrust as stated by Billig [10]. Furthermore, the injection of fuel into the boundary layer may lead to unwanted effects such as boundary layer separation or premature ignition due to high local static temperatures. This has to be taken into account when designing the injection system, as additional cooling may be required in case local combustion zones occur in the vicinity of the combustor walls.

A suitable alternative for supplying the fuel directly into the center of the combustor flow is strut injection, where coaxial injection can be realized, while good mixing of the fuel is ensured simultaneously. However, this method comes at the price of higher drag due to the geometrical blockage caused by the injector. Struts can either cover the full width of the combustion chamber, or they are designed as semi- or partial struts and only reach into the flow to a certain extent [7]. The simplest geometry is a plain, wedge-shaped injector with fuel injection at the trailing edge and a sharp leading edge, which is intended to minimize the intensity of the bow shock [122, 167, 180, 195]. Using the same geometry, pilot fuel injection ports at the top and bottom surfaces of the strut can be installed to enhance combustion [73, 129]. This type of injector has also been used within the JAPHAR project as described by Dessornes and Scherrer [34]. Although the strut itself may already provide flame-holding capabilities, the influence of an additional cavity located directly downstream of the strut has been investigated by Hsu et al. [72]. Further variations include the positioning of the leading edge in the inlet section of the engine [161] or the annular arrangement of several partial struts in a circular combustion chamber [160].

While variations in the leading edge geometry are limited due to drag considerations, the trailing edge may be modified to significantly enhance the mixing capabilities of the strut. The most basic alteration would be the introduction of two-dimensional features such as corners [83] or steps [59, 193]. A more complex approach is a three-dimensional, lobed modification of the trailing edge to induce streamwise vorticity into the main flow and thereby enhance the mixing process. Selected examples for three-dimensional trailing edge geometries are shown in figure 1.7.

Such a fuel injector with a sinusoidally lobed trailing edge was originally developed for use in turbofan engines by Presz et al. [126, 127] in the late 1980s. Its application in subsonic flows was further investigated experimentally [41, 145] and numerically [154] in the following decade. Gaston et al. [60] and

## 1 Introduction

---

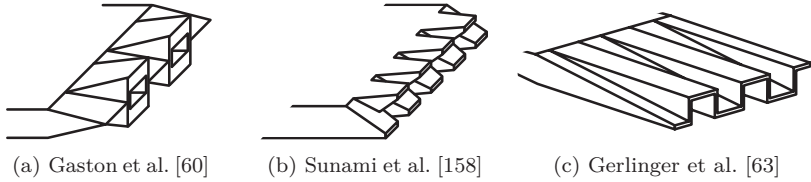


Figure 1.7: Examples of three-dimensional injector trailing edge geometries

Charyulu et al. [24] then adapted similar concepts for supersonic flows, while at the same time the Hypermixer injector, as shown in figure 1.7b, was developed at JAXA by Sunami et al. [156, 158]. Since then, different versions of the Hypermixer have been tested extensively during experiments in cooperation with ONERA [87, 157, 158]. Furthermore, sophisticated numerical simulations of the flow field around the injector have been conducted [54]. During the first phase of LAPCAT, also strut injectors with three-dimensional trailing edges have been studied [68, 137]. However, they were not pursued any further during the second phase of the project and the focus was laid on wall injection instead.

Within the GRK 1095, a lobed strut injector is the central part of the staged fuel injection system. Its prototype is shown in figure 1.7c and was first investigated by Gerlinger et al. [62, 63]. A slightly modified version, as shown in figure 1.8a, which was reduced in width by one lobe to fit the supersonic test channel at ITLR, was then used as first fuel injection stage for the GRK scramjet demonstrator. Numerical and experimental investigations have proven the capabilities of the strut [64], also in conjunction with a second, wall bound injection stage [174, 175]. The wider version of the strut has also been tested at ITAM [56], where higher enthalpy conditions than at ITLR could be realized.

However, in contrast to wall bound fuel injection systems, struts have the inherent drawback of being exposed to the main flow inside the combustion chamber, which results in considerable heat loads especially at high flight Mach numbers. For this reason, Billig [10] does not recommend the use of protruding fuel injectors above Mach 10 unless active cooling of the injection device can be realized. Even specialized carbon/carbon materials, as for example tested by Bouchez et al. [12], reach their operational limits at such high Mach numbers. Also the use of a rounded leading edge is limited by the fact that, despite exhibiting lower heat fluxes [5], the intensity of the leading edge shock wave, and thus also drag and pressure losses, are increased.

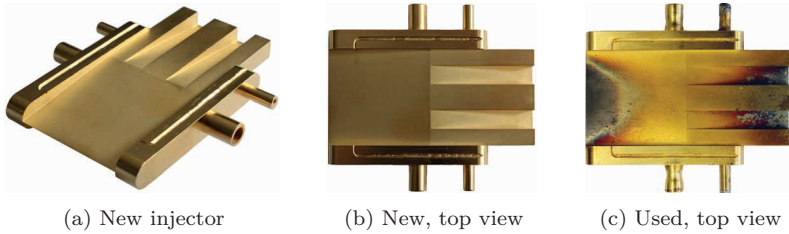


Figure 1.8: Lobed strut injector investigated at ITLR during the GRK 1095

While water can be used during ground tests to internally cool the strut leading edge [105, 165], for flight tests the fuel is the most efficient choice for the coolant. During PREPHA, hydrogen was fed through a bore along the leading edge before being injected into the main flow [128], thus combining fuel preheating and cooling of the highly stressed parts of the injector. Also approaches with porous struts exist [74, 75], where the fuel passes through the strut walls during injection. However, in case the leading edge is intended to be cooled with this method, high internal pressures are required to account for the stagnation pressure of the main flow. Furthermore, ignition of the fuel directly at the strut surface and at the leading edge has to be prevented despite the high static flow temperatures.

The quantification of the heat loads remains a challenging topic, as they can hardly be measured experimentally. In case of the GRK strut, only damages to the surface can be evaluated, as can be seen by a comparison of figures 1.8b and 1.8c. Therefore, a numerical approach is essential to further identify highly stressed zones and optimize the internal cooling. A coupled numerical approach, which also takes into account the heat conduction inside the solid strut, is inevitable to obtain accurate results. Zhong et al. [196] investigated a semi-strut with simple fuel bores using a loosely coupled numerical simulation and identified highly stressed zones along the leading edge. Better cooling can be achieved using a more complex internal flow path as integrated into the lobed strut investigated withing the GRK 1095 and described in detail in section 3.1.3.

Conjugate simulations for this strut have been realized by Rust et al. [135] as well as by Gerlinger and Simsont [65, 143], but due to being restricted to a structured numerical grid the internal geometry of the strut still had to be simplified. Yet characteristics of the internal flow could be identified, and it was shown that the use of a blunt leading edge indeed reduces the maximum temperatures of the structure. Preliminary experiments and also numerical

## 1 Introduction

---

simulations of a modified model containing only the upstream half of the injector have been conducted within the frame of student research projects [8, 168]. For these experiments water was used as coolant medium instead of air. The studies led to an identification of recirculation zones inside the strut and do qualitatively agree with the work of Gerlinger and Simson.

### 1.3 Objectives and Outline of the Thesis

As described above, the thermal loads within a scramjet and especially in the combustion chamber are very difficult to quantify experimentally, which illustrates the need for numerical investigations. Therefore, within the framework of the graduate school GRK 1095 the demand for a new numerical solver containing all relevant modules for a complete aerodynamic and thermodynamic investigation of a scramjet combustor was established. To simplify further development and modification, this solver was to be included into the open-source computational fluid dynamics (CFD) software package OpenFOAM. This approach also allows for massive parallelization of simulations without a costly licensing model, as is the case for commercial codes.

The project was realized in cooperation with the Chair of Thermodynamics at the Technical University of Munich, where a suitable thermophysical model library for OpenFOAM had already been developed within previous work [44]. Based on this work, Makowka [101] modified an existing density-based solver [67] by implementing multi-species transport and support of chemical reactions.

Within the present thesis, the solver's capabilities are further extended towards the numerical simulation of conjugate heat transfer. A coupled approach containing both fluid flow and solid body is needed to correctly capture the heat conduction effects inside the solid structure as well as the heat transfer at the solid surfaces due to the flow field. The possibility of transient simulations is maintained by choosing a fully coupled approach. Furthermore, due to the solver's ability to deal with unstructured and hybrid meshes, the need for geometrical simplifications is obsolete.

Before being applied to investigate the lobed strut injector, the new solver has first to be validated using reference data available from literature. Besides ensuring the correct prediction of supersonic flows in general, the focus is laid on features particularly relevant for wall heat transfer, such as boundary layers and their interaction with shock waves. As validation data for supersonic conjugate heat transfer is only scarcely available and often lacks well-defined boundary conditions, additional validation experiments are conducted at the

ITLR supersonic test facility for moderate flow temperatures. Lastly, the newly developed solver is applied to the strut injector at more realistic flow conditions, which correspond to typical combustion experiments at the ITLR test facility. Considering these main objectives, the outline of the present thesis can be summarized as follows:

- I. Extension of the capabilities of the OpenFOAM solver by the implementation of conjugate heat transfer, multi-region support and, if necessary, further modules to enable efficient simulations of conjugate heat transfer problems. The solver development is described in chapter 4.
- II. Validation of the solver regarding all major flow phenomena relevant for the correct prediction of heat transfer. For this purpose data available from both literature and previous studies is used. The validation is presented in detail in chapter 5.
- III. Realization of experiments at the ITLR supersonic test facility to obtain heat transfer information for the lobed strut injector at moderate flow temperatures, which can then be used for a further validation of the numerical code. The corresponding comparison of experimental and numerical data is discussed in the first part of chapter 6.
- IV. Application of the validated solver to investigate the strut injector at hot gas conditions, which are typical for combustion experiments at ITLR. The second part of chapter 6 is dedicated to the evaluation of these simulations.

## 1.4 Publications

Selected results and aspects described within the present thesis have in parts been published previously by the author [18, 38, 39, 52, 99].



To lay the foundation for the investigation of supersonic heat transfer, the physical fundamentals of the flows in question have to be considered first. This chapter provides a short introduction to the physical background and presents the governing equations for compressible, multi-species flows. Subsequently, the basics of heat transfer and heat conduction will be established briefly. The characteristics of high-speed flows as well as viscous effects are discussed, because shock waves, boundary layers and also their interaction play a major role in any investigation of heat transfer in supersonic channel flows.

### **2.1 Governing Equations for Compressible, Viscous Flow**

Any kind of fluid in motion can be physically described by the fundamental laws of conservation. These are the conservation of mass, momentum, and – in case heat transport is considered – energy. Typically the thermal and caloric equations of state are added to these fundamental laws, as they connect the state variables of the investigated flow and close the system of equations. For compressible flows, the laws of conservation represent a set of coupled differential equations, which can be solved analytically only for rare and highly

## 2 Physical Fundamentals

---

simplified cases. This creates the need for numerical simulations, as will be discussed in chapter 4.

The relevant equations are briefly presented below. Their formulation follows the derivations of Anderson [2] and White [188]. Einstein notation, where  $i, j, k = 1, 2, 3$ , is used for most equations in differential form, while bold symbols indicate vectors.

### 2.1.1 Conservation of Mass

Mass cannot be created or destroyed inside a closed system. Out of this principle, it can be derived that the sum of the mass fluxes into a control volume equals the rate of mass change inside the volume. This results in the integral form of the *continuity equation*

$$-\iint_S \rho \mathbf{u} \cdot d\mathbf{S} = \frac{\partial}{\partial t} \iiint_V \rho dV, \quad (2.1)$$

where  $V$  is the control volume and  $S$  represents its surface. Note that equation (2.1) is valid for any kind of flow, no matter if viscous, inviscid, compressible or incompressible. The continuity equation can also be written in differential form, which results in

$$\frac{\partial \rho}{\partial t} + \frac{\partial (\rho u_j)}{\partial x_j} = 0. \quad (2.2)$$

This formulation is valid for a single species or a mixture of species, where  $\rho$  would then represent the density of the mixture. In case of multiple species being transported, transport equations for the individual mass fractions  $Y_n$  of  $N$  different species are required. Also diffusion occurring within mixtures of several species has to be included. Thus, according to Gerlinger [61], equation (2.2) can be written as

$$\frac{\partial (\rho Y_n)}{\partial t} + \frac{\partial (\rho Y_n u_j)}{\partial x_j} = \frac{\partial}{\partial x_j} \left( \rho D_n \frac{\partial Y_n}{\partial x_j} \right) + \dot{\omega}_n \quad (2.3)$$

for each species using Fick's law of diffusion [49]. In this equation,  $\dot{\omega}_n$  denotes a production term due to chemical reactions.

It has to be noted that Fick's law is by definition only valid for binary mixtures. However, it still provides a reasonably good approximation for multi-component

---

## 2.1 Governing Equations for Compressible, Viscous Flow

gases, while being computationally more efficient compared to more complex approaches [32, 43].

To satisfy the conservation of mass, the sum of all the species mass fractions  $Y_n$  has to equal unity. Within numerical simulations this is often realized by obtaining the last mass fraction of  $N$  species using

$$Y_N = 1 - \sum_{n=1}^{N-1} Y_n, \quad (2.4)$$

which, however, results in a slight loss of accuracy. Preferably the species chosen for this approach would be an inert one to avoid significant falsification of chemical reactions. An additional requirement concerns the sum of the production terms  $\dot{\omega}_n$ , which has to be zero to fulfill mass conservation.

### 2.1.2 Conservation of Momentum

The sum of the external forces onto an object or fluid particle is equal to the time rate of momentum change of the object. Also known as Newton's second law, this principle is commonly formulated as

$$\mathbf{F} = \frac{\partial(m\mathbf{u})}{\partial t} = m\mathbf{a}. \quad (2.5)$$

Two different types of forces have to be distinguished. Body forces, including electromagnetic and gravitational effects, are exerted on the fluid inside a control volume  $V$ . Surface forces, on the contrary, act on the surface  $S$  of the control volume and include shear stresses  $\tau_{ij}$  as well as normal stresses  $\tau_{ii}$  due to pressure effects. These forces then equal the change in momentum inside the volume itself, combined with the sum of momentum flow over the control volume surface. This yields the integral form of the *momentum equation*

$$\iiint_V \rho \mathbf{f} dV - \iint_S p d\mathbf{S} + \mathbf{F}_{visc} = \iiint_V \frac{\partial(\rho \mathbf{u})}{\partial t} dV + \iint_S (\rho \mathbf{u} \cdot d\mathbf{S}) \mathbf{u}. \quad (2.6)$$

Equation (2.6) can be converted into a set of three coupled differential equations commonly known as the Navier-Stokes equations, which are

$$\frac{\partial(\rho u_i)}{\partial t} + \frac{\partial(\rho u_i u_j)}{\partial x_j} = -\delta_{ij} \frac{\partial p}{\partial x_j} + \rho g_i + \frac{\partial \tau_{ij}}{\partial x_j}. \quad (2.7)$$

## 2 Physical Fundamentals

---

Assuming a Newtonian fluid, where shear stresses are a linear function of the strain rate, and using Stoke's hypothesis [153], the stress tensor  $\tau_{ij}$  can be written as

$$\tau_{ij} = \mu \left( \frac{\partial u_i}{\partial x_j} + \frac{\partial u_j}{\partial x_i} - \frac{2}{3} \delta_{ij} \frac{\partial u_k}{\partial x_k} \right) \quad (2.8)$$

with the Kronecker delta

$$\delta_{ij} = \begin{cases} 1 & \text{if } i = j \\ 0 & \text{if } i \neq j \end{cases}. \quad (2.9)$$

The dynamic viscosity  $\mu$  is a fluid property, which is a function of the fluid temperature. Within the present thesis, Sutherland's law [159] is used to calculate the dynamic viscosity.

$$\frac{\mu}{\mu_{ref}} = \left( \frac{T}{T_{ref}} \right)^{\frac{3}{2}} \frac{T_{ref} + S}{T + S} \quad (2.10)$$

For the calculation of boundary conditions, the reference values for temperature and viscosity as well as Sutherland's constant  $S$  are taken from White [188]. The values relevant for the present thesis are listed in table 2.1.

Table 2.1: Parameters for Sutherland's law [188]

	$\mu_{ref}$ [kg/(m s)]	$T_{ref}$ [K]	$S$ [K]
Air	$1.716 \cdot 10^{-5}$	273.15	110.4
H <sub>2</sub>	$0.841 \cdot 10^{-5}$	273.15	97.0
He	$1.900 \cdot 10^{-5}$	273.15	79.4

### 2.1.3 Conservation of Energy

Energy can neither be created nor destroyed inside a closed volume, but it can be converted into another form. This is comprised in the first law of thermodynamics, which states that the sum of the work exerted on the fluid

## 2.1 Governing Equations for Compressible, Viscous Flow

---

due to both body and surface forces and the heat added to the control volume equal the energy change of the fluid inside the control volume itself.

$$\begin{aligned} \dot{W}_{visc} + \dot{Q} - \iint_S p \mathbf{u} \cdot d\mathbf{S} + \iiint_V \rho (\mathbf{f} \cdot \mathbf{u}) dV \\ = \iiint_V \frac{\partial (\rho e_t)}{\partial t} dV + \iint_S \rho e_t \mathbf{u} \cdot d\mathbf{S} \end{aligned} \quad (2.11)$$

As supersonic flows are considered, the kinetic energy of the fluid cannot be neglected. Therefore, the total internal energy  $e_t$  is used in equation (2.11) instead of the static internal energy  $e_s$ . In addition, to correctly describe chemically reacting flows also the heat of formation  $h_c$  has to be taken into account. As described in [61], this leads to

$$e_t = e_s + \frac{|\mathbf{u}|^2}{2} + h_c. \quad (2.12)$$

For a mixture of  $N$  different species, which are approximated as ideal gases, the static internal energy  $e_s$  and the heat of formation  $h_c$  can be written as

$$e_s = \sum_{n=1}^N Y_n e_n = \sum_{n=1}^N \left( Y_n \int_{T_{ref}}^T c_{v,n} dT \right) \quad (2.13)$$

and

$$h_c = \sum_{n=1}^N Y_n h_{c,n}. \quad (2.14)$$

Similar to the conservation equations for mass and momentum also the energy equation can be converted into differential form, yielding

$$\frac{\partial (\rho e_t)}{\partial t} + \frac{\partial ([\rho e_t + p] u_j)}{\partial x_j} = \rho u_j g_j + \frac{\partial (\tau_{ij} u_i)}{\partial x_j} - \frac{\partial \dot{q}_j}{\partial x_j}. \quad (2.15)$$

The heat flux  $\dot{q}$  includes both heat conduction and diffusion effects.

$$\dot{q}_j = -\lambda \frac{\partial T}{\partial x_j} - \sum_{n=1}^N (h_{s,n} + h_{c,n}) \rho D_n \frac{\partial Y_n}{\partial x_j} \quad (2.16)$$

## 2 Physical Fundamentals

---

Radiation is not considered within the present thesis, therefore no additional source term has been included in equation (2.16).

The conservation equations are often linked using two dimensionless quantities. The Prandtl number  $Pr$  describes the ratio of viscous and thermal diffusion and is defined as

$$Pr = c_p \frac{\mu}{\lambda} = \frac{\nu}{\alpha} = \frac{\text{viscous diffusion}}{\text{thermal diffusion}}. \quad (2.17)$$

It is a measure for the ratio of velocity boundary layer thickness to thermal boundary layer thickness. The Prandtl number is a fluid property, which depends on pressure and temperature. For air at ambient conditions  $Pr \approx 0.72$ , while for increasing pressure and temperature the value for  $Pr$  also increases. For the present thesis the Prandtl number is set to 0.75 unless stated otherwise. Besides reflecting the increased temperature level for most investigated test cases, this value is also chosen to maintain comparability to previous studies [176].

The second dimensionless quantity is the Schmidt number  $Sc$ , which links the viscous diffusion to the mass diffusion due to species transport.

$$Sc = \frac{\mu}{\rho D} = \frac{\nu}{D} = \frac{\text{viscous diffusion}}{\text{mass diffusion}} \quad (2.18)$$

The Schmidt number is a species property, the values used for the present thesis are listed in table 2.2.

Table 2.2: Species Schmidt numbers [11, 112]

H <sub>2</sub>	He	N <sub>2</sub>	O <sub>2</sub>
0.28	0.22	0.87	0.99

### 2.1.4 Equations of State

To close the system of equations (2.2), (2.7) and (2.15), additional equations connecting  $e$ ,  $p$ ,  $T$  and  $\rho$  are necessary. The most common approach is to consider the fluid as ideal gas and thereby neglect intermolecular forces, which results in the thermal equation of state

$$p = \rho RT, \quad (2.19)$$

---

## 2.2 Heat Conduction and Heat Transfer

with  $R$  being the specific gas constant of the considered species. This is only valid for gases at comparably low pressures or high temperatures, where the distance between the molecules outweighs their size. Taking into account a multi-species flow, equation (2.19) can be written as

$$p = \rho R_m T \sum_{n=1}^N \frac{Y_n}{M_n}, \quad (2.20)$$

using the universal gas constant  $R_m$  and the molecular masses  $M_n$  of the single species.

For ideal gases, the specific heats  $c_p$  and  $c_v$ , and therefore also the enthalpy and the internal energy, are a function of temperature only, which is expressed by the caloric equation of state

$$e = \int_{T_0}^T c_v(T) dT. \quad (2.21)$$

This has already been utilized in enthalpy formulation in equation (2.13) and is usually also exploited within numerical simulations, where the fluid properties can be supplied by temperature-dependent tabulated data.

## 2.2 Heat Conduction and Heat Transfer

The heat conduction inside a solid body with constant density  $\rho$  and constant specific heat capacity  $c$  is described by the three-dimensional heat equation

$$\rho c \frac{\partial T}{\partial t} = \frac{\partial}{\partial x_i} \left( \lambda \frac{\partial T}{\partial x_i} \right) + \dot{q}_v, \quad (2.22)$$

where  $\lambda$  is the heat conductivity of the solid material and  $\dot{q}_v$  denotes any internal heat sinks or sources. The heat conductivity inside the solid body is usually considered to be independent of both temperature and location, which allows for the definition of the thermal diffusivity

$$\alpha = \frac{\lambda}{\rho c}. \quad (2.23)$$

Using this simplification, the heat equation can be reformulated as

$$\frac{\partial T}{\partial t} = \alpha \frac{\partial^2 T}{\partial x_i^2} + \frac{\dot{q}_v}{\rho c}. \quad (2.24)$$

## 2 Physical Fundamentals

---

The heat flux at the solid body surface is related to the temperature gradient perpendicular to the wall inside the surrounding fluid by

$$\dot{q}_w = -\lambda \frac{\partial T}{\partial n} = h (T_f - T_w) . \quad (2.25)$$

Here  $h$  denotes the convective heat transfer coefficient of the fluid,  $T_f$  represents the fluid temperature and  $T_w$  is the temperature of the wall .

If supersonic flows are considered, also the dimensionless Stanton number

$$St = \frac{h}{\rho u c_p} = \frac{\dot{q}_w}{\rho u c_p \Delta T} \quad (2.26)$$

is commonly used for the evaluation of convective wall heat fluxes. However, the choice of suitable reference conditions for the Stanton number remains a disputed topic throughout literature. While fluid velocity and density are often set to free-stream conditions, various approaches exist for the reference temperature. Schlichting and Gersten [139] suggest the adiabatic wall temperature

$$T_{w,ad} = T_\infty \left( 1 + r \frac{\gamma - 1}{2} M_\infty^2 \right) \quad (2.27)$$

as suitable choice when investigating high-speed flows. This formulation introduces the turbulent recovery factor  $r$  at the wall, which is hard to quantify and usually cannot be measured during experiments. Theoretical definitions given in literature vary from constant values of  $r = 0.87$  [139] to variable approaches such as  $r = \sqrt[3]{Pr}$  [188]. For reasons of simplicity, especially in experiments the total flow temperature is often used instead of the adiabatic wall temperature, as it can usually be measured with a manageable amount of effort. Thus, the total flow temperature is also used as reference temperature for all cases investigated within the present work.

### 2.3 High-Speed Flows

In contrast to subsonic flows, where information propagates upstream due to the flow velocity being smaller than the speed of sound, information can only be transported downstream in fully supersonic and hypersonic flows. This causes the appearance of completely different flow features compared to those observed in the subsonic regime. The phenomena which are most relevant for the present thesis will be introduced shortly in the following section.

### 2.3.1 Shock Waves and Prandtl-Meyer Expansion Fans

The most important phenomena regarding supersonic flows are shock waves and expansion fans. Shock waves, which usually occur in the form of oblique shocks as shown in figure 2.1a, are caused by the flow being diverted inwards. This may occur, for example, due to geometric discontinuities or a sudden narrowing of the flow cross section. As in purely supersonic flows no information can propagate upstream, a sudden change in fluid properties takes place, whereas for subsonic flows a gradual adaption to the new flow state would occur.

Shock waves are generally considered isentropic in order to assess them analytically. This implies a constant total temperature, while static pressure, static temperature and density increase over the shock wave. As a result, the Mach number is decreased, which is combined with a loss in total pressure. The intensity of these changes in state variables increases with the angle of the geometrical discontinuity.

For an attached oblique shock wave, the wave angle  $\beta$  is a function of the deflection angle  $\theta$  and the Mach number  $M_1$  upstream of the shock wave. This is expressed by the so-called  $\theta$ - $\beta$ - $M$  relation, where  $\gamma$  is the ratio of the specific heats  $c_p$  and  $c_v$ .

$$\tan \theta = \frac{2}{\tan \beta} \left[ \frac{M_1^2 \sin^2 \beta - 1}{M_1^2 (\gamma + \cos 2\beta) + 2} \right] \quad (2.28)$$

Equation (2.28) provides two solutions for each given set of Mach number and deflection angle: A weak solution, where  $M_2 > 1$ , and a strong solution, where the flow is subsonic downstream of the oblique shock wave. Usually the weak solution is favored, unless an artificial pressure rise is induced downstream of

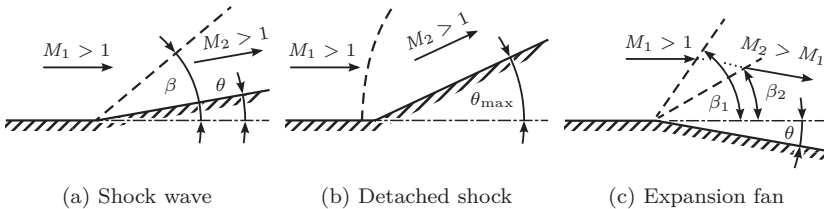


Figure 2.1: High speed flow phenomena, adapted from [2]

## 2 Physical Fundamentals

---

the discontinuity. The Mach number downstream of the oblique shock wave can be calculated by

$$M_2 = \frac{M_{n,2}}{\sin(\beta - \theta)}. \quad (2.29)$$

The index  $n$  denotes the Mach number component normal to the shock wave, which is defined as

$$M_{n,2}^2 = \frac{M_{n,1}^2 + \frac{2}{\gamma-1}}{\frac{2\gamma}{\gamma-1} M_{n,1}^2 - 1} \quad (2.30)$$

with

$$M_{n,1} = M_1 \sin \beta. \quad (2.31)$$

The changes in state variables over the shock wave can then be determined using the normal component of the upstream Mach number,  $M_{n,1}$ .

$$\frac{\rho_2}{\rho_1} = \frac{(\gamma + 1) M_{n,1}^2}{(\gamma - 1) M_{n,1}^2 + 2} \quad (2.32)$$

$$\frac{p_2}{p_1} = 1 + \frac{2\gamma}{\gamma + 1} (M_{n,1}^2 - 1) \quad (2.33)$$

$$\frac{T_2}{T_1} = \frac{p_2}{p_1} \frac{\rho_2}{\rho_1} \quad (2.34)$$

Moreover, equation (2.28) also shows that a maximum deflection angle  $\theta_{max}$  exists, which is a function of the free-stream Mach number. If the geometrical deflection angle  $\theta$  exceeds  $\theta_{max}$ , no solution for an attached oblique shock wave can be found. Instead, the shock detaches from the geometrical discontinuity as shown in figure 2.1b. This fact is often exploited to reduce aerodynamic heating, for example by using blunt leading edges for reentry vehicles, as most of the heat is then dissipated before reaching the solid surface. However, especially for hypersonic vehicles this comes at the price of considerably higher drag, which usually is not a major concern when considering atmospheric reentry.

Equations (2.29) to (2.33) can be simplified considerably in case of a normal shock wave, which corresponds to  $\beta = 90^\circ$ . Here  $M_{n,1}$  equals  $M_1$  and the flow is always subsonic downstream of the shock.

In case of an outwards turning geometrical discontinuity, the flow exhibits an expansion fan. In contrast to shock waves, here the Mach number increases, which results in a decrease of static pressure, static temperature and density. As can be seen in figure 2.1c, an expansion fan is bounded by a Mach line in both upstream and downstream direction. The Mach line angle  $\beta$  is only depending on the corresponding adjacent Mach number.

$$\beta = \arcsin \frac{1}{M} \quad (2.35)$$

The change in state variables across an expansion fan occurs gradually between those two Mach lines, opposed to the abrupt change in case of a shock wave. Thus, to determine the connection between the geometrical angle  $\theta$  and the change in flow Mach number, one has to integrate over a series of infinitesimal expansion waves. This leads to the Prandtl-Meyer function  $\nu$ , which is only depending on the local flow Mach number.

$$\nu(M) = \sqrt{\frac{\gamma+1}{\gamma-1}} \arctan \sqrt{\frac{\gamma-1}{\gamma+1} (M^2 - 1)} - \arctan \sqrt{M^2 - 1} \quad (2.36)$$

Due to the complexity of equation (2.36), the values for the Prandtl-Meyer function are usually extracted from tabulated data sets. The downstream Mach number is then obtained using

$$\nu(M_2) = \theta + \nu(M_1), \quad (2.37)$$

while the remaining changes in state variables are calculated via the isentropic flow relations as listed in appendix A.

### 2.3.2 Viscous Interactions

After the introduction of the main flow characteristics, also viscous effects need to be considered. Especially boundary layers are vital for any kind of wall-bounded flow, and are even more important in case of confined channels. Furthermore, the interaction of such boundary layers with the flow phenomena described above needs to be taken into account.

## 2 Physical Fundamentals

---

### Boundary Layers

In general, within viscous flows a boundary layer develops in the vicinity of a solid surface. It accounts for the fact that the flow velocity has to be equal to zero directly at the surface itself. Bridging the gap between the state values in the wall-near region and the main flow conditions, these boundary layers exhibit characteristic velocity and temperature profiles. The interface in wall normal direction between boundary layer and main flow is often defined at a velocity ratio of

$$\frac{u}{u_\infty} = 0.99, \quad (2.38)$$

where  $u_\infty$  denotes the free-stream velocity. Boundary layers start up laminar at leading edges, before transitioning to turbulent at a location depending on the main flow Reynolds number. This dimensionless quantity describes the ratio of inertial forces and viscous forces.

$$Re = \frac{\rho L u}{\mu} \quad (2.39)$$

$L$  is the characteristic length of the flow in question, in case of boundary layer transition usually the run length along the wall is used. Within a scramjet engine, the Reynolds numbers are sufficiently high to cause transition already in the engine inlet, which is why inside the combustion chamber the assumption of a fully turbulent boundary layer is valid in the majority of cases. This considerably reduces the complexity of numerical simulations, as the transition process itself is not yet fully understood and can only be modeled in a limited way when considering turbulence modeling as described in chapter 4.

Although the conservation equations, as introduced in the previous section, are also valid for the boundary layer region, they can be significantly simplified using an order of magnitude analysis as conducted for example by Anderson [1] or by Schlichting and Gersten [139]. For subsonic and moderately supersonic flows, this results in the static pressure being constant in wall normal direction within the boundary layer, namely

$$\frac{\partial p}{\partial y} = 0. \quad (2.40)$$

However, one has to keep in mind that this is not necessarily the case when dealing with flows at hypersonic Mach numbers, as also shown by Anderson [1]. In this case, also the boundary layer thickness  $\delta$  exhibits a strong dependency

on the Mach number due to compressibility effects, while it only depends on the Reynolds number for incompressible fluids.

This leads to a faster thickening of the boundary layer, similar to the effect of temperature gradients caused by a hot surface. While at higher flow Mach numbers the supersonic part of the boundary layer increases, a subsonic zone always exists directly at the wall. Therefore, even in supersonic flows an upstream propagation of information is possible within these regions.

Two characteristic variables are often used for boundary layer analysis: The dimensionless wall distance

$$y^+ = \frac{y}{\nu_w} \sqrt{\frac{\tau_w}{\rho_w}} = \frac{y}{\nu_w} \sqrt{\frac{\mu_w}{\rho_w} \left( \frac{\partial u}{\partial n} \right)_w} \quad (2.41)$$

and the dimensionless velocity

$$u^+ = \frac{u}{u_\tau} = u \sqrt{\frac{\rho_w}{\tau_w}} = u \sqrt{\frac{\rho_w}{\mu_w \left( \frac{\partial u}{\partial n} \right)_w}}. \quad (2.42)$$

In the viscous sublayer directly at the wall, the simple connection  $u^+ = y^+$  between these two variables exists. Within this region the flow velocity, and thus also the Reynolds number, are so low that the flow is considered to be laminar. Further away from the wall, in the so-called logarithmic region of the boundary layer, von Kármán [178] proposed that

$$u^+ = \frac{1}{\kappa} \ln y^+ + C. \quad (2.43)$$

Here,  $\kappa$  denotes the von Kármán constant, which is typically set to 0.41. Equation (2.43) is commonly referred to as the *logarithmic law of the wall* and is often used in numerical simulations. In theory, these relations are only valid for incompressible flows. For moderately supersonic flows, however, Morkovin's hypothesis essentially states that the dynamics of high-speed boundary layers follow the incompressible pattern [147] and can thus be considered using the same models as for low flow velocities.

### Shock Wave/Boundary Layer Interaction

In case a shock wave impacts on a boundary layer, it causes a thickening of the boundary layer and may even induce boundary layer separation. As depicted schematically in figure 2.2, the impinging shock penetrates the boundary layer

## 2 Physical Fundamentals

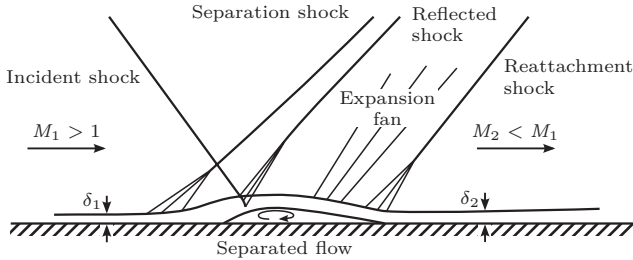


Figure 2.2: Shock wave/boundary layer interaction, adapted from [1, 142]

and induces a pressure rise, which is then relayed upstream by the subsonic part of the boundary layer and results in a local increase of the boundary layer thickness  $\delta$ . The resulting reduction of the flow cross section leads to the formation of small shock waves, which unite to form the separation shock and then cross the incident shock wave.

As the static flow pressure downstream of these waves is increased and thus higher than inside the boundary layer, the flow is bent towards the wall and the boundary layer thickness is reduced again until reattachment. The reduction in  $\delta$  generates an expansion fan, while the reattachment itself produces one more shock wave due to the redirection of the flow. Due to the fact that  $M_2$  is lower than  $M_1$ , the boundary layer thickness  $\delta_2$  is always increased compared to  $\delta_1$  upstream of the shock impact.

When dealing with normal shock waves in internal flows, the interaction with the boundary layer leads to an additional phenomenon, which is described in detail by Matsuo et al. [106]. While a normal shock wave is shown to exist up to around  $M = 1.2$ , for higher Mach numbers the shock first exhibits a curved structure, before it bifurcates due to boundary layer effects. As shown in figure 2.3, for  $M > 1.5$  this leads to a series of shock waves usually referred to as *shock train*. Carroll and Dutton [21] furthermore distinguished between normal shock trains at  $M < 2$  and oblique shock trains for higher Mach numbers. Here, the normal shock components in the center of the flow are replaced by fully oblique shocks, thus eliminating local subsonic zones in the shock train. The more general term *pseudo-shock*, which combines the actual shock train and the following mixing zone, was introduced by Crocco [27].

Pseudo-shocks are especially relevant when dealing with experimental channels such as described in sections 3.1.1 and 3.1.2, where an adaption to ambient pressure by means of a shock train occurs at the channel exit. Although in theory

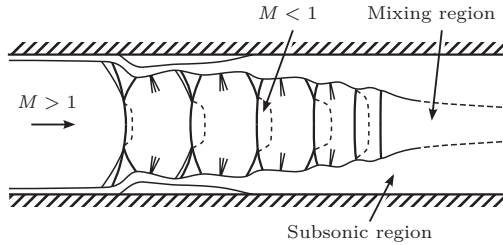


Figure 2.3: Flow structures in a pseudo-shock region, adapted from [106, 186]

a pseudo-shock should be completely symmetrical, experimental investigations have shown an asymmetric behavior [21, 130, 155] at  $M \geq 2$ . This phenomenon has also been observed at the experimental facility used within the present thesis [138, 176]. The onset of the oblique shocks at the top and bottom walls is slightly different, which leads to an inclination of the complete shock train. However, the reasons for this behavior are not yet completely understood. While in experiments small geometrical imperfections might cause a systematic asymmetry, the same phenomenon also occurs in numerical simulations [115, 130, 176], where the perfectly symmetrical numerical grids should theoretically eliminate any geometrical influence.



Experimental investigations are vital for the validation of any new numerical simulation tool. To expand the validation cases found in literature towards the actual strut injector used during the GRK 1095, experiments are conducted at the supersonic facility at ITLR. While the experimental focus was on the fuel injection and the mixing performance in the wake of the injector within previous studies, now the strut surface itself is the subject of investigation. In this chapter the experimental facility as well as the test channels are presented and the test conditions for the experiments are defined. Subsequently, the lobed strut injector and its complex internal and external geometry are described in more detail. The measurement techniques relevant for the experimental investigations are introduced in the second part of the chapter.

### **3.1 Experimental Facility**

The combustion test bench at ITLR is a continuously operating connected tube facility, which is designed for experiments at supersonic flow speed. Spurious radicals in the flow due to vitiation are avoided by using an electrical heater system, thus allowing the reproduction of atmospheric flight conditions.

### 3 Experimental Methods

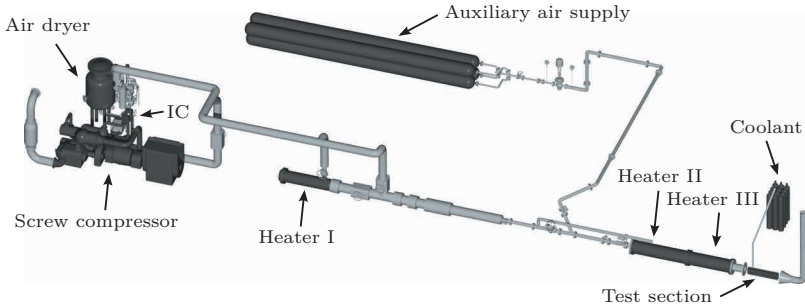


Figure 3.1: ITLR combustion test facility

Figure 3.1 presents an overview of the facility and its components. A screw compressor supplies a continuous air mass flow of up to  $\dot{m} = 1.45 \text{ kg/s}$  at a maximum total pressure of  $p_t = 1 \text{ MPa}$ . At this stage, the relative humidity of the compressed air is still considerably higher than the one corresponding to high altitude flight conditions. Therefore, an air dryer is installed, which reduces the humidity to less than 0.5%. Due to thermal restrictions of the air dryer, an intercooler (IC) is connected upstream. The compressed and dried air is then fed into a three-staged electrical heater system with a maximum total power consumption of 400 kW. Depending on the experimental conditions, this allows for total flow temperatures of up to  $T_t = 1350 \text{ K}$  at the inlet of the test section. At the exit of the test section, the exhaust gas is blown out into the ambience. The auxiliary air supply, which is designed as an emergency reservoir to cool the heating system in case of compressor failure during experiments, can also be used to provide cooling air for components of the test channel. Other gases used as coolant, or as fuel in case of combustion experiments, are provided directly to the test section via additional supply lines.

The operating range of the facility is mainly restricted by the Laval nozzle of the investigated test channel. Depending on the flow conditions upstream, the nozzle limits the mass flow rate throughout the channel. By combining the mass flow rate with the capacity of the electrical heating system, performance charts for the facility can be obtained. Two such charts for Laval nozzles corresponding to  $M = 2.0$  and  $M = 2.5$ , which are investigated within the present thesis, are shown in figure 3.2. Here, the solid lines illustrate the air mass flow rate, while the dashed lines represent the unit Reynolds number. The black marks in figures 3.2a and 3.2b correspond to the chosen experimental conditions. For each Mach number both hot flow and cold flow experiments were conducted at the model combustion chamber, which will be described in

### 3.1 Experimental Facility

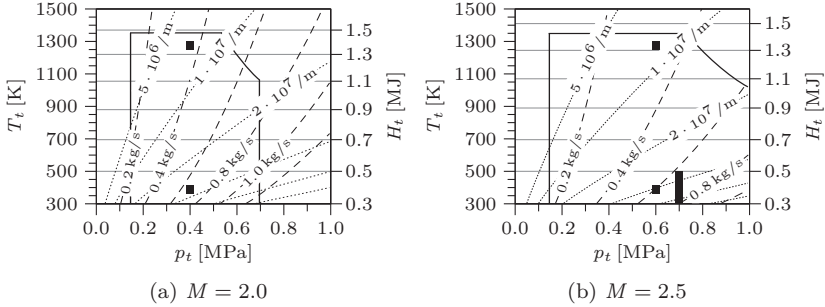


Figure 3.2: Operational range of the facility for different Laval nozzles [138] (dashed lines indicate the air mass flow rate, dotted lines represent the unit Reynolds number)

the following section. In case of  $M = 2.5$  and hot gas experiments, the total pressure upstream of the nozzle is limited to  $p_t = 0.6$  MPa by the capacity of the heater system.

For the modular supersonic test channel as presented in section 3.1.2, experiments were only carried out at  $M = 2.5$  and moderate flow temperatures. Compared to the combustor tests the total pressure for these investigations was increased to 0.7 MPa, which is the nominal design pressure of the  $M = 2.5$  Laval nozzle and provides a higher air mass flow. A summary of the relevant experimental conditions for the main air flow is given in table 3.1.

Table 3.1: Overview of the experimental conditions for the main air flow

	Combustion Chamber				Modular Channel			
	2.0	2.0	2.5	2.5	2.5	2.5	2.5	2.5
$M [-]$	2.0	2.0	2.5	2.5	2.5	2.5	2.5	2.5
$p_t$ [MPa]	0.4	0.4	0.6	0.6	0.7	0.7	0.7	0.7
$T_t$ [K]	390.0	1300.0	390.0	1300.0	350.0	400.0	450.0	500.0
$\dot{m}$ [g/s]	644.9	353.2	580.9	318.2	762.5	713.1	668.4	634.1

#### 3.1.1 Model Combustion Chamber

The ITLR model combustion chamber is used for the experimental investigation of supersonic combustion phenomena and fuel injection strategies. It is manufactured from copper and is water-cooled in order to withstand the high flow temperatures. As shown in figure 3.3, the chamber is segmented into

### 3 Experimental Methods

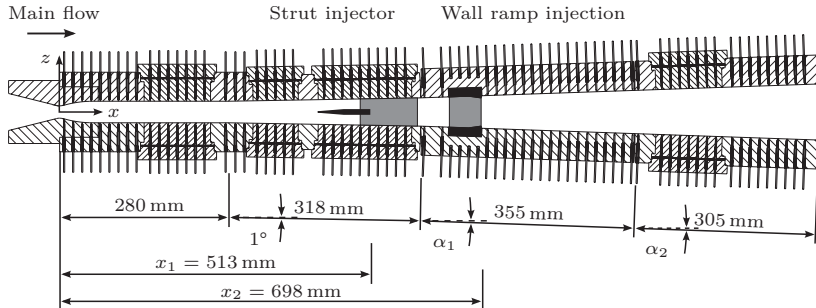


Figure 3.3: Schematic of the model combustion chamber

four parts: The first section features a constant height of 35.4 mm, followed by a second section with an opening angle of  $1^\circ$  with respect to the horizontal center plane. The last two segments exhibit a variable opening angle, which has been set to  $2^\circ$  for the present investigations. The cross section of the model combustion chamber is rectangular with a constant width of 40 mm. At the combustor exit the flow adapts to ambient pressure and is led into the exhaust system.

Fuel is injected via a two staged injection system, consisting of a strut injector as first stage and wall-bound ramp injectors as second stage. These fuel injectors are described in more detail in section 3.1.3. The Laval nozzle insert at the combustor inlet can be exchanged in order to realize different main flow Mach numbers ranging from 1.7 to 2.5. All relevant distances in  $x$ -direction are measured from the critical cross section of this Laval nozzle:  $x_1$  denotes the position of the first stage injection ports and  $x_2$  corresponds to the injection slots of the second stage.

Static pressure taps are arranged along the center line of the top and bottom walls to monitor the wall pressure during experiments. Optical access to the flow is provided via quartz windows in the combustor side walls. These lateral windows, which are marked gray in figure 3.3, are used for schlieren imaging within the present thesis.

#### 3.1.2 Modular Test Channel

In contrast to the model combustion chamber, the modular test channel is designed for experiments at moderate total temperatures. Therefore, it is

## 3.1 Experimental Facility

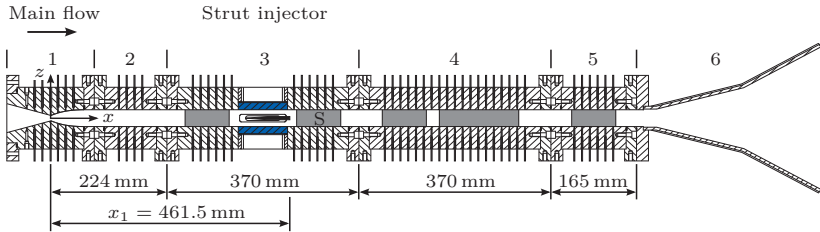


Figure 3.4: Schematic of the modular test channel

manufactured from stainless steel and is not actively cooled during experiments. This limits the maximum temperature to approximately 550 K due to sealings and measurement devices. A schematic of the modular test channel is shown in figure 3.4. The order of the modules 2 to 5 can be interchanged to adjust to experimental requirements. The channel features a constant cross section of 35.4 mm height and 40 mm width, which corresponds to the cross section of the first combustion chamber segment. Again, an exchangeable Laval nozzle insert is installed. A flow Mach number of 2.5 is used for the investigations presented in this thesis.

Compared to the model combustor, the modular channel provides additional optical access at the top and bottom channel walls, as the omission of cooling channels and pipes not only considerably simplifies manufacturing, but also offers space for additional windows. The strut injector used within the model combustor can be mounted in the modular channel as well. Two windows, which are marked blue in figure 3.4, provide the optical access to the top and bottom surfaces of the injector. Due to the fact that the channel is designed for experiments including infrared measurements, these window slots are equipped with sapphire windows, which exhibit a high infrared transmissivity up to a wavelength of  $5\ \mu\text{m}$ . Quartz windows are installed in the channel side walls to allow for schlieren imaging (S) and laser based measurement techniques. Similar to the model combustion chamber, the static wall pressure is monitored using pressure taps along the center line of the top and bottom channel walls.

### 3.1.3 Fuel Injectors

The fuel injection system investigated at the ITLR supersonic facility is based on a two-staged approach. The first stage consists of the aforementioned lobed

### 3 Experimental Methods

---

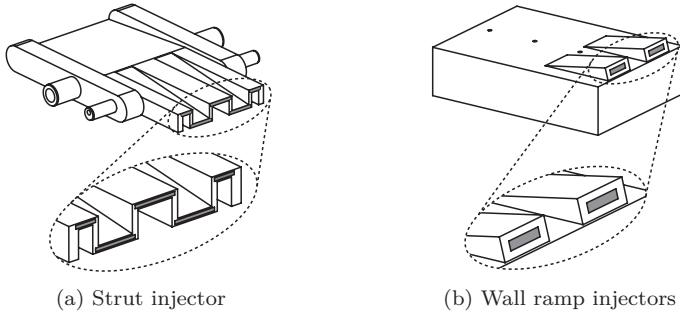


Figure 3.5: Schematics of the fuel injectors

strut injector, as shown in the schematic drawing in figure 3.5a. The strut is positioned horizontally in the center of the flow. A second fuel injection stage is installed further downstream to consume any oxygen left in near-wall regions. A wall-bound double ramp configuration at the top and bottom combustion chamber walls, as depicted in figure 3.5b, is used for this purpose. This staged fuel injection configuration has been investigated in both experimental and numerical studies before [173–176]. Within these investigations, good overall performance and combustion efficiency could be achieved due to the enhanced fuel mixing capabilities of the strut.

The lobed strut injector is made of copper and is coated with gold to prevent hydrogen embrittlement and oxidation. It extends over the whole channel width of 40 mm and is 86 mm long. The strut features a sharp leading edge, followed by a wedge-shaped upstream half of the injector. As shown in figure 3.6a, the lobes start at half length of the injector, where the maximum height of 7 mm is reached, and deepen towards the horizontal injection ports. This leads to the trailing edge geometry presented in figure 3.6b.

The injection ports, which are marked gray in figures 3.5a and 3.6b, are 9.2 mm wide at the three central slots and 4.6 mm wide at the two outer ones, respectively. All slots have a height of 0.7 mm, which results in a total injection cross section of 25.76 mm<sup>2</sup>.

The two outermost lobes are narrower than the center ones, which leads to slightly different flow phenomena regarding flow separation in these regions. Small Laval nozzles are installed directly upstream of the injection slots, which reduce the velocity difference between main flow and fuel by accelerating the fuel up to approximately  $M = 2$ .

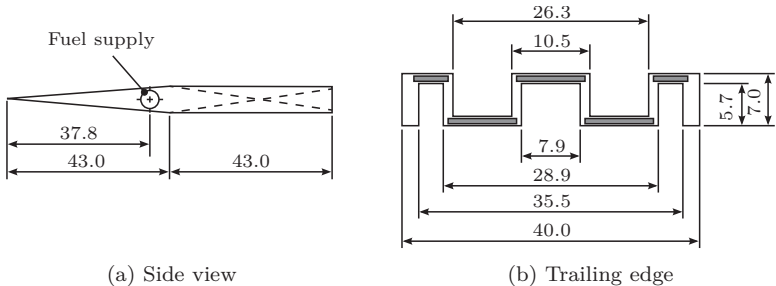


Figure 3.6: Geometry of the strut injector, all dimensions in mm

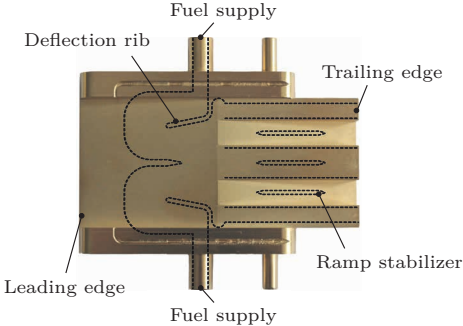


Figure 3.7: Internal flow path of the strut injector

As the injector is exposed to the heat loads imposed by the channel flow, it has to be cooled by the fuel to withstand the extreme thermal conditions inside the combustion chamber. For this purpose, the internal fuel flow path is designed to direct the fuel, which is supplied from the sides of the injector, at first towards the highly stressed leading edge by means of deflection ribs installed at either side of the strut. It is then diverted by 180° towards the trailing edge. The internal flow path is shown schematically by the dashed lines in figure 3.7. The upstream limit of the flow path is located at 14 mm length, a further extension towards the leading edge is impossible due to the small height of the injector. Within the three center lobes small ribs are installed, which support the structural integrity of the strut and are also intended to straighten the flow towards the injection ports. For measurement purposes, the strut can be equipped with two thermocouples to monitor the total temperature of the coolant in the lobed region.

### 3 Experimental Methods

---

A similar, ramped structure is also used for the wall-bound second stage injectors. The ramps are 2.44 mm high at their trailing edge. Together with a ramp length of 21.5 mm, this leads to a ramp angle of  $10^\circ$  relative to the combustor wall. The fuel flow path itself is inclined towards the channel center axis by  $5^\circ$ , therefore the fuel is injected at an angle of  $15^\circ$  with regard to the combustor wall. The injection ports, which are marked gray in figure 3.5b, are rectangular at a height of 1.4 mm and a width of 6.9 mm. This corresponds to a total injection cross section of  $38.64 \text{ mm}^2$  for the second stage.

## 3.2 Measurement Techniques

Within supersonic flows non-intrusive measurement techniques are preferable, as any object inserted into the flow causes a significant alteration of the flow field. Thus either optical and laser-based techniques or wall-bound approaches are widely used in this field of research. The techniques used for the presented experiments are briefly introduced in the following. The air mass flow and the total flow temperature are measured upstream of the Laval nozzle in the subsonic part of the facility, while all other data is obtained directly at the experimental channel.

### 3.2.1 Mass Flow Measurements

The mass flow rate of air supplied by the screw compressor is measured upstream of heater stage II, where a vortex flow meter (*Prowirl 77, Endress+Hauser*) is installed. The measurement uncertainty is given by the manufacturer to be less than 1%. Combining the measured volume flow rate with local pressure and temperature measurements and assuming ideal gas behavior, the air mass flow rate can be calculated using

$$\dot{m} = \frac{p}{RT} \dot{V}. \quad (3.1)$$

where  $R$  is the specific gas constant of air.

### 3.2.2 Temperature Measurements

Standard type K thermocouples from *Omega* are installed to measure different temperatures within the experimental setup. According to the manufacturer, the specific error of these thermocouples is  $\pm 0.4\%$ . However, previous studies

have shown that due to positioning and the use of extension wires a value of  $\pm 2\%$  seems to be more realistic [138].

The total flow temperature is obtained at the exit of heater stage III, where three thermocouples are located in the cross-section of the main air flow. The measured values are then averaged to reduce the uncertainty. Furthermore, the total temperature of the internal flow inside the strut injector is measured at two locations. The position of these thermocouples, however, cannot be determined exactly due to the complex inner geometry of the injector, which may lead to additional uncertainties. For the uncooled modular test channel, also the external wall temperature is measured at different locations along the channel to obtain an averaged reference value, which is used as boundary condition for the numerical simulations.

### 3.2.3 Static Wall Pressure

Static wall pressure measurements are widely used to gain experimental information about channel flows. They allow a general impression of the flow field, including the identification of the position and strength of shock and expansion waves. For each investigated experimental channel, in total up to 112 static wall pressure taps are distributed along the symmetry plane at the top and bottom walls. These taps are connected to seven pressure transducers (*Scanivalve DSA3016*, maximum range up to 0.7 MPa) via tubes. According to the manufacturer, the measurement uncertainty of these transducers is less than  $\pm 0.05\%$  of the full scale, which corresponds to a maximum error of  $\pm 350$  Pa.

By evaluating the static wall pressure distribution information about flow features can be obtained. However, due to the linear distribution of the taps along the channel, three-dimensional effects within the flow cannot be resolved using this technique. Despite a maximum sampling rate of 625 Hz, transient measurements are not possible due to the length of the pressure tubes and the compressibility of the air contained within.

### 3.2.4 Schlieren Imaging

A schlieren imaging system is used to visualize changes in refraction index, which correspond to the presence of a density gradient within the flow. The schematic setup of a standard schlieren system is shown in figure 3.8. A combination of a white light-emitting diode (*Philips Luxeon Rebel*) and a small aperture of 1 mm is used as punctual light source. By positioning the aperture

### 3 Experimental Methods

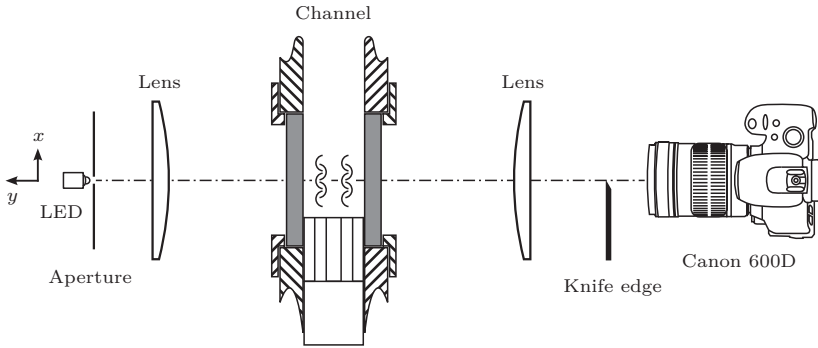


Figure 3.8: Schlieren imaging setup

in the focal point of an achromatic lens ( $f = 1000$  mm,  $d = 100$  mm), the beam is parallelized before being directed through the test volume. A second, identical achromatic lens is then used to focus the beam onto a horizontal knife edge. The density gradients perpendicular to the knife edge are visualized by blocking the diverted part of the beam, thus one-dimensional schlieren are obtained. The image is captured using a *Canon EOS 600D* camera with a maximum resolution of 18 megapixels.

As the presented method creates an integrated image, which visualizes the entire beam path between the two achromatic lenses, it can only be used for cold flow cases or short duration experiments. For long-duration hot flow

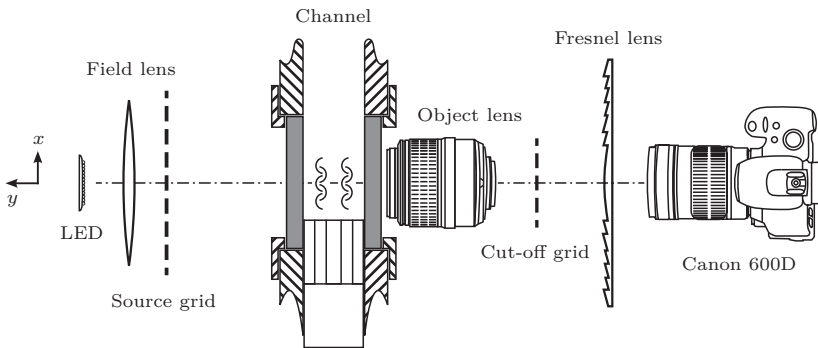


Figure 3.9: Focusing schlieren imaging setup

experiments with  $T_t > 600$  K, the temperature gradients inside the quartz windows cause a change in refraction index, which can block the smaller effects of shock and expansion waves within the flow. Therefore, a focusing schlieren setup as shown in figure 3.9 is used for hot gas experiments, which allows the visualization of only a small volume within a certain depth of focus.

The present setup is an adaption of the work of Kouchi et al. [86] and has been configured and validated for use at the ITLR model combustion chamber [18]. In contrast to the conventional schlieren setup, additional optical parts are required to create a focal plane inside the test volume, namely an object lens has to be used in between the source and the cut-off grids. A detailed description of the focusing schlieren system at ITLR and also of the image post-processing method can be found in [52]. It could be shown that the depth of focus is sufficiently small to eliminate effects caused by the channel windows, and thus allows for schlieren imaging during hot gas and combustion experiments.

### 3.2.5 Laser-Induced Thermal Acoustics

Laser-induced thermal acoustics (LITA) is a laser-based, non-intrusive measurement technique derived by Cummings et al. [28, 29], which has been used successfully at ITLR for shock tubes [50] and supersonic flows [71]. While at ITLR speed of sound measurements were first conducted for free jets [70], recent work by Förster [51] has extended the application range to also include flow velocity measurements and the application of the technique at confined ducts.

For LITA, two laser beams are crossed to create an intensity grating within the electrical field, which results in a density grating in the flow and thus in a periodic disturbance of the refraction index. An additional interrogation beam is then scattered by the grating. The physical properties of the flow can be probed by analyzing the frequency of the signal beam. The beam displays a damped oscillation, where the frequency is a direct function of the fluid speed of sound. Assuming an ideal gas and a known test gas composition, the static flow temperature can then be determined. Considering a moving fluid, also information about the flow velocity can be obtained by evaluating the resulting Doppler shift in the frequency of the signal beam.

Besides the non-intrusive nature of the measurement technique, which renders LITA well suited for supersonic flows, it offers additional advantages. Firstly, point measurements are possible instead of line-of-sight average data acquisition, as for example is the case for schlieren imaging. This is especially useful for

### 3 Experimental Methods

---

the validation of numerical codes. Furthermore, even for a low signal quality as may be the case for locally disturbed or chemically reacting flows, a signal analysis can still be realized, as the measured flow properties only depend on the damping frequency of the signal.

#### 3.2.6 Infrared Thermography

To identify the heat load distribution on the injector, infrared measurements are conducted using the modular test channel as described above in section 3.1.2. A FLIR SC7600 infrared camera is used for the experimental campaign, which is able to detect infrared rays with a wavelength between  $1.5\ \mu\text{m}$  and  $5.1\ \mu\text{m}$ . This range combines short-wavelength and mid-wavelength infrared, where air is nearly completely transmissive and thus does not alter the measurements. Furthermore, sapphire glass is also highly transmissive for these wavelengths and is therefore used as window material within the optical path of the infrared system. The camera technology is based on an InSb detector and is cooled down to 77 K during experiments by an internal Stirling engine. The camera chip provides a maximum resolution of  $640 \times 512$  pixels, the noise-equal temperature difference is given by the manufacturer to be less than 25 mK.

As the experimental infrastructure does not allow to position the camera below the channel, an infrared mirror is installed, which deflects the radiation towards the camera. In order to eliminate reflections caused by the sapphire window, this mirror has to be tilted. For this purpose, and to ease optical alignment, it is attached to a 5-axis mount. Due to the resulting image distortion and the reduction of the field of view, the tilt angle is reduced as little as possible while still avoiding reflection. The optimum inclination is found to be  $3^\circ$ . To account for the tilted view of the injector surface, all data are rectified before post-processing. Additional reflections of the camera background are eliminated using a screen mounted at the camera lens. The resulting experimental setup is shown in figure 3.10. As the gold coating of the injector exhibits a high reflectivity and thereby renders infrared measurements impossible, the injector is painted black to ensure a high and uniform emissivity for the whole surface. The emissivity  $\epsilon$  of the paint is approximately 0.9.

Due to the small size of the strut injector, an in-situ temperature calibration using thermocouples is extremely difficult. Surface thermocouples at the outer surface would cover a significant part of the area of interest to the infrared measurements. They would also cause a disturbance of the channel flow due to both the thermocouple itself and the necessary wiring. Therefore a quantification of the influence of both the sapphire windows and the infrared

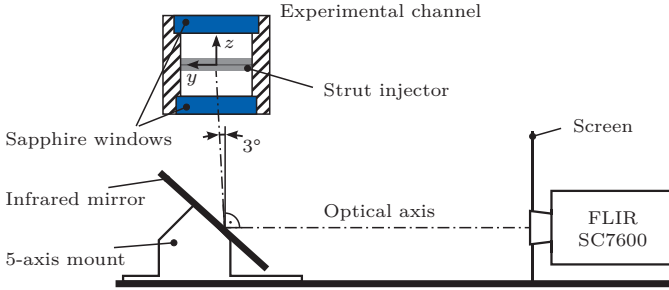


Figure 3.10: Infrared measurement setup

mirror cannot be obtained and no direct temperature data can be extracted from the infrared measurements. Instead a dimensionless surface temperature

$$\Theta = \frac{T - T_{min}}{T_{max} - T_{min}} \quad (3.2)$$

is introduced, which eliminates the emissivity and its remaining uncertainty. Furthermore, the influence of the windows and the mirror is reduced by this difference quotient approach, as they affect all the measured values to the same degree.



Due to the fact that the conservation equations as introduced in chapter 2 can usually not be solved analytically, a numerical approach is inevitable. The underlying theory is discussed within the present chapter, including a brief introduction into turbulence and its numerical modeling. In the second part of the chapter, the OpenFOAM software package is presented, which has been chosen to be the platform for the implementation of the new solver. Subsequently, the solver features are described in detail and further additions to the numerical code for purposes of post-processing and data evaluation are summarized.

### 4.1 Fundamentals

Before going into detail about OpenFOAM and the numerical solver used within the scope of this thesis, the fundamental principle of discretization has to be introduced in brief. Furthermore, turbulence in general and the utilized modeling approach are discussed, as this has direct consequences for the design of the computational grids and the definition of the boundary conditions.

### 4.1.1 Finite Volume Method

In order to allow for a numerical solution of the governing equations as introduced in chapter 2, the partial derivatives have to be approximated by algebraic differences. The simplest approach is using *finite differences*, where a discrete grid is placed on the domain. Difference equations can then be solved at each grid point, which results in a system of equations for the computational domain. However, for this method to be conservative, the equation system has to be formulated based on conserved variables  $(\rho, \rho \mathbf{u}, \rho \mathbf{Y}, e_t)$  instead of primitive variables  $(\rho, \mathbf{u}, \mathbf{Y}, p)$ . This usually requires a transformation of the equations. Furthermore, certain prerequisites regarding differentiability have to be met, which are not necessarily given in case of supersonic flows due to the presence of shock and expansion waves.

Another way to discretize the domain is the use of *finite volumes*, where control volumes are used instead of calculating the variables at grid points. The integral form of the conservation equations (2.1), (2.6) and (2.11) can then be solved for each control volume. In contrast to finite differences, this method is conservative without a transformation of the variables, as a flux leaving one control volume is directly entering the neighboring volume. Using Gauss's divergence theorem, the volume integrals are converted into surface integrals, which can then be replaced by the sum of all cell faces of the control volume. This leaves the calculation of the convective fluxes across the cell faces, where different techniques exist. Regarding supersonic flows a Riemann solver [166] is the most suitable choice, as it is not only able to deal with discontinuities, but also provides an exact solution for the fluxes. At each cell face left and right states are introduced, representing local discontinuities. The flux across the cell face is then computed by solving a Riemann problem at each face. However, Riemann solvers, such as the often used version introduced by Roe [131] or the Harten-Lax-van-Leer-Contact (HLLC) [166] solver, are computationally expensive compared to standard central schemes, which illustrates the need for alternatives.

One such alternative is the central discretization scheme developed by Kurganov and Tadmor [88]. It takes into account the information transport along the direction of sound wave propagation, thus the local speed of sound is the only additional information needed compared to a standard central differencing scheme. Similar to an actual Riemann solver, each cell face is still split into left and right states, but the computational effort is considerably reduced due to the central differencing approach. Two numerical schemes for reconstructing the fluxes are investigated within the present thesis: A total variation diminishing

(TVD) scheme developed by van Leer [170] and the Gamma scheme of Jasak et al. [77], which represents a blend of upwind and central differencing based on a factor  $\Gamma$ . A reasonable margin for this blending factor is  $0.1 \leq \Gamma \leq 0.5$  [77], Gaskell and Lau [58] suggest  $\Gamma = 1/6$  as optimum value. While for higher values of  $\Gamma$  numerical diffusion increases, for low values instabilities may occur, thus a compromise is needed to ensure accuracy and stability of the computations. By default the scheme of van Leer is used for the presented numerical simulations unless noted otherwise.

Within the present thesis, a variation of the explicit Euler scheme is used for time discretization, which is of first order accuracy and only stable for a Courant-Friedrichs-Lewy (CFL) number below unity. As mentioned above, the local speed of sound  $a$  has to be taken into account for the calculation of the time step in case the approach of Kurganov and Tadmor is used. Therefore, the maximum possible time step is obtained using the acoustic CFL condition

$$C = \frac{(|u| + a) \Delta t}{\Delta x} \leq 1. \quad (4.1)$$

### 4.1.2 Turbulence

Turbulence is generally associated with the random and chaotic fluctuation of flow quantities in time and space. While the conservation equations are also valid for turbulent flows, the numerical simulation of turbulence is a challenging topic. As the relevant length scales are extremely small, a computational grid resolving even the smallest eddies would result in enormous numerical costs. Wilcox [190] derived an estimation for the number of grid points  $N$  needed for such a direct numerical simulation (DNS), which depends on the Reynolds number.

$$N_{\text{DNS}} = (0.088Re)^{9/4} \quad (4.2)$$

At the moment DNS is only feasible for relatively simple configurations at small to moderate Reynolds numbers. The numerical simulation of technical applications, especially in the field of supersonic flows, is still not possible with the available computational resources. An alternative approach is a large eddy simulation (LES), where only the large-scale eddies are resolved, while eddies below the grid cell size are modeled. Still, the numerical effort for LES is high and a three-dimensional, transient simulation is inevitable to account for the anisotropic and time-dependent behavior of the simulated eddies. While LES

## 4 Numerical Methods

---

may be a suitable method to obtain accurate comparative data for experiments, it does not yet qualify as a fast and efficient design approach.

Therefore, the most common approach is to consider the Reynolds-averaged Navier-Stokes (RANS) equations, where averaging leads to the creation of additional terms that are interpreted as quantities related to turbulent motion. Closure for these terms is then obtained by a turbulence model, which can be chosen according to the desired accuracy, the complexity of the investigated flow and the numerical resources at hand.

### Reynolds-Averaged Conservation Equations

The process of Reynolds-averaging is based on the assumption that a time-dependent flow variable can be split into a time-averaged and a fluctuating part. Considering the flow velocity as an example, this implies that

$$u = \bar{u} + u', \quad (4.3)$$

which contains the time-averaged part

$$\bar{u} = \frac{1}{\Delta t} \int_{t_0}^{t_0 + \Delta t} u dt \quad (4.4)$$

and the fluctuating velocity  $u'$ . In order to fulfill the conservation of mass, the time-average of the fluctuating part has to be equal to zero. Regarding compressible flows and multi-component gases, it is often beneficial to use a mass-weighted average to simplify the resulting averaged conservation equations. This process is also known as Favre-averaging. This results in

$$u = \tilde{u} + u'', \quad (4.5)$$

where the Favre-averaged velocity  $\tilde{u}$  is defined as

$$\tilde{u} = \frac{\overline{\rho u}}{\bar{\rho}}. \quad (4.6)$$

In contrast to Reynolds-averaging, Favre-averaging additionally accounts for turbulent density fluctuations. Turbulent pressure fluctuations, however, will not be considered within the present thesis. It has to be noted that for Favre-averaging  $\overline{\rho u''} = 0$  applies instead of  $u'' = 0$ , which was required in case of Reynolds-averaging. Applying the averaging process to the conservation equations results in the following equations for the conservation of mass,

momentum, and energy. External body forces are neglected here, as they are not relevant for the present thesis.

$$\frac{\partial \bar{\rho}}{\partial t} + \frac{\partial (\bar{\rho} \tilde{u}_i)}{\partial x_i} = 0 \quad (4.7)$$

$$\frac{\partial (\bar{\rho} \tilde{u}_i)}{\partial t} + \frac{\partial (\bar{\rho} \tilde{u}_i \tilde{u}_j)}{\partial x_j} = -\delta_{ij} \frac{\partial \bar{p}}{\partial x_j} + \frac{\partial}{\partial x_j} (\bar{\tau}_{ij} - \overline{\rho u_i'' u_j''}) \quad (4.8)$$

$$\begin{aligned} \frac{\partial (\bar{\rho} \tilde{e}_t)}{\partial t} + \frac{\partial ([\bar{\rho} \tilde{e}_t + \bar{p}] \tilde{u}_j)}{\partial x_j} &= \frac{\partial}{\partial x_j} (\tilde{u}_i [\bar{\tau}_{ij} - \overline{\rho u_i'' u_j''}]) \\ &+ \frac{\partial}{\partial x_j} \left( -\overline{\rho c_p u_j'' T''} + \bar{\tau}_{ij} u_i'' - \frac{1}{2} \overline{\rho u_j'' u_i'' u_i''} \right) - \frac{\partial \bar{q}_j}{\partial x_j} \end{aligned} \quad (4.9)$$

Compared to equation (2.12), the averaged total internal energy  $e_t$  now also contains the turbulent kinetic energy  $k$ .

$$e_t = e_s + \frac{|\mathbf{u}|^2}{2} + k + h_c \quad (4.10)$$

If one compares these averaged equations to the original ones as introduced in section 2.1, no new terms are created in the continuity equation. For the conservation of momentum, however, compared to equation (2.7) the averaging process additionally yields the turbulent stresses, or *Reynolds stresses*,  $\overline{\rho u_i'' u_j''}$ . This term is often modeled using the Boussinesq approximation [14], which assumes a linear dependency of the form

$$\begin{aligned} \tau_{ij,t} &= -\overline{\rho u_i'' u_j''} = 2\bar{\rho} \nu_t S_{ij}^* - \frac{2}{3} \delta_{ij} \bar{\rho} k \\ &= \bar{\rho} \nu_t \left( \frac{\partial \tilde{u}_i}{\partial x_j} + \frac{\partial \tilde{u}_j}{\partial x_i} - \frac{2}{3} \delta_{ij} \frac{\partial \tilde{u}_k}{\partial x_k} \right) - \frac{2}{3} \delta_{ij} \bar{\rho} k. \end{aligned} \quad (4.11)$$

$S_{ij}^*$  denotes the mean strain rate tensor,  $k$  is the turbulent kinetic energy and  $\nu_t$  is the turbulent momentum diffusivity, also often referred to as turbulent kinematic viscosity.

In addition to the Reynolds stresses in the momentum equation, the averaging of the energy equation results in three more new terms, namely  $\overline{\rho c_p u_j'' T''}$ ,  $\bar{\tau}_{ij} u_i''$  and  $\frac{1}{2} \overline{\rho u_j'' u_i'' u_i''}$ . According to Wilcox [190], the last two terms can be neglected

## 4 Numerical Methods

---

unless hypersonic flows are considered, where they are commonly approximated using

$$\overline{\tau_{ij}u_i''} - \frac{1}{2}\overline{\rho u_j'' u_i'' u_i''} = \bar{\rho} \left( \nu + \frac{\nu_t}{\sigma_k} \right) \frac{\partial k}{\partial x_j}. \quad (4.12)$$

Thus only the turbulent heat flux  $\overline{\rho c_p u_j'' T''}$  remains unknown. Similar to Boussinesq's approach, it can be transformed assuming a linear dependency and introducing the turbulent thermal diffusivity  $\alpha_t$ . However, compared to equation (4.11), this is considerably simplified, as for any scalar quantity  $\Phi$  it is assumed that

$$\overline{u_j'' \Phi''} = -\Lambda \frac{\partial \tilde{\Phi}}{\partial x_j} \quad (4.13)$$

with  $\Lambda$  being a constant. This results in

$$\dot{q}_{j,t} = -\overline{\rho c_p u_j'' T''} = \bar{\rho} c_p \alpha_t \frac{\partial \tilde{T}}{\partial x_j}. \quad (4.14)$$

Lastly, Favre-averaging is also applied to the species transport equation (2.3), which yields

$$\frac{\partial (\bar{\rho} \tilde{Y}_n)}{\partial t} + \frac{\partial (\bar{\rho} \tilde{Y}_n \tilde{u}_j)}{\partial x_j} = \frac{\partial}{\partial x_j} \left( \bar{\rho} D_n \frac{\partial \tilde{Y}_n}{\partial x_j} \right) - \frac{\partial}{\partial x_j} (\overline{\rho u_j'' Y_n''}) + \bar{\omega}_n. \quad (4.15)$$

Here the turbulent diffusion flux  $\overline{\rho u_j'' Y_n''}$  is unknown. Therefore, a turbulent mass diffusivity  $D_t$  is defined analogously to Fick's law [49].

$$\dot{j}_{j,n,t} = -\overline{\rho u_j'' Y_n''} = \bar{\rho} D_t \frac{\partial \tilde{Y}_n}{\partial x_j} \quad (4.16)$$

These three turbulent diffusivities can be connected by defining turbulent equivalents to the Prandtl number and the Schmidt number as introduced in equations (2.17) and (2.18).

$$Pr_t = \frac{\nu_t}{\alpha_t} = \frac{\text{turbulent momentum diffusivity}}{\text{turbulent thermal diffusivity}} \quad (4.17)$$

$$Sc_t = \frac{\nu_t}{D_t} = \frac{\text{turbulent momentum diffusivity}}{\text{turbulent mass diffusivity}} \quad (4.18)$$

By assuming  $Pr_t$  and  $Sc_t$  to be constant, which is an approach widely used in literature due to its simplicity, only  $\nu_t$  and  $k$  remain unknown in the averaged conservation equations. Closure for these variables is achieved by the use of turbulence models. Different types exist, ranging from algebraic zero-equation to more sophisticated two-equation models, which solve two additional coupled differential transport equations. An exception are Reynolds-stress models, which do not assume a proportionality between the turbulent stresses and the mean strain rate and thus are able to take into account anisotropic turbulence. However, this comes at the price of considerably higher numerical costs. Within the present thesis, the two-equation shear-stress transport (SST) model as developed by Menter [109] is used for all numerical simulations, as it has shown to yield good results for supersonic channel flows in previous numerical studies at ITLR [4, 118, 174–176].

It has to be noted that if the turbulent Prandtl number is assumed to be constant, the value for  $Pr_t$  is still subject to discussion throughout literature. Most of the values vary between 0.75 and unity for applications comparable to the one investigated here. An overview of different approaches is given by Kays [81], who states that for large values of the Peclet number  $Pe = RePr$ , e.g. in case of supersonic flows, the turbulent Prandtl number approaches 0.85 within the logarithmic part of the boundary layer. As this is one of the most important flow regions for numerical prediction of wall heat transfer,  $Pr_t = 0.85$  is used within the present thesis unless stated otherwise. The turbulent Schmidt number  $Sc_t$ , which also is a disputed value in literature, is set to 0.6 for all species. This value has also been used in previous numerical simulations of the ITLR model combustion chamber [101]. In the present thesis, however, mixing of different species only occurs in the wake of the injector and does not have a significant influence on the main focus of the work. Thus, possible uncertainties regarding the mixing process due to the assumption of a constant value for  $Sc_t$  are considered to be acceptable.

All equations in the remaining part of this chapter will be Favre-averaged. However, the actual Favre notation is omitted to improve comprehensibility.

### Shear-Stress Transport Model

The SST model represents a combination of two standard two-equation models, namely the  $k$ - $\varepsilon$  model developed by Launder and Sharma [89] and the  $k$ - $\omega$  model introduced by Wilcox [189]. Both models are widely used and well validated, but show weaknesses within certain flow regions. While the  $k$ - $\varepsilon$  model in its standard formulation is not able to completely resolve the boundary

## 4 Numerical Methods

---

layer, the  $k$ - $\omega$  model exhibits a strong dependency on the free-stream value of  $\omega$ . To eliminate these disadvantages, Menter [109] suggested a blending of both models, which applies a  $k$ - $\omega$  formulation in wall-near regions and switches to  $k$ - $\varepsilon$  behavior further away from the walls. The model solves two coupled differential equations, one for the turbulent kinetic energy  $k$  and one for the specific turbulence dissipation rate  $\omega$ . It is linked to the turbulence dissipation rate  $\varepsilon$  by

$$\omega = \frac{\varepsilon}{C_\mu k}. \quad (4.19)$$

Here  $C_\mu$  is a constant, which is usually set to 0.09. For the coupling of the two different models, the transport equation for the turbulence dissipation rate  $\varepsilon$ , as introduced by Launder and Sharma [89], has first to be converted into a formulation based on  $\omega$  using equation (4.19). A blending factor  $F_1$  is then introduced to switch between the two models depending on the flow region, which results in the following transport equations for the SST model.

$$\frac{\partial \rho k}{\partial t} + \frac{\partial \rho u_j k}{\partial x_j} = \tau_{ij} \frac{\partial u_i}{\partial x_j} - \beta^* \rho \omega k + \frac{\partial}{\partial x_j} \left( \rho (\nu + \sigma_k \nu_t) \frac{\partial k}{\partial x_j} \right) \quad (4.20)$$

$$\begin{aligned} \frac{\partial \rho \omega}{\partial t} + \frac{\partial \rho u_j \omega}{\partial x_j} = & \frac{\gamma}{\nu_t} \tau_{ij} \frac{\partial u_i}{\partial x_j} - \beta \rho \omega^2 + \frac{\partial}{\partial x_j} \left( \rho (\nu + \sigma_\omega \nu_t) \frac{\partial \omega}{\partial x_j} \right) \\ & + 2(1 - F_1) \rho \sigma_{\omega 2} \frac{1}{\omega} \frac{\partial k}{\partial x_j} \frac{\partial \omega}{\partial x_j} \end{aligned} \quad (4.21)$$

The model constants  $\beta$ ,  $\beta^*$  and  $\gamma$  as well as the formulation for the blending factor  $F_1$ , which is based on a complex hyperbolic tangent approach, are described in detail in the publications of Menter and his group [109, 110]. The implementation of the model into CFD applications may vary slightly regarding several additional limiters, especially within the production terms of  $k$  and  $\omega$ , to ensure numerical stability.

### Near-Wall Treatment

The resolution of the boundary layer, and especially of the viscous sublayer, is a relevant issue for every numerical simulation, as it determines the accuracy of the gradients at the wall. If the wall region is completely resolved down to a dimensionless wall distance of  $y_1^+ = 1$ , these gradients can be calculated directly using a linear approach between the wall and the first cell.

The wall boundary condition for  $k$  is derived from the fact that the velocity, and also the velocity fluctuations, directly at the wall are zero. As  $k$  is a function of the velocity fluctuations, this yields  $k_w = 0$ . Regarding  $\omega$ , Menter [109] suggests

$$\omega_w = \frac{60\nu_w}{0.075(\Delta y_1)^2}. \quad (4.22)$$

For high Reynolds numbers, as in supersonic flows, the requirement of  $y_1^+ = 1$  leads to a wall normal grid cell extent in the order of  $1 \cdot 10^{-6}$  m to  $1 \cdot 10^{-7}$  m. Thus, this approach is numerically very expensive due to the resulting high number of necessary grid cells. In addition, the reduced size of the cells at the wall leads to a small time step in order to maintain the CFL condition for transient simulations as introduced in equation (4.1). This also increases the total simulation time.

An alternative approach is the use of wall functions, which bridge the viscous sublayer and require the first grid point away from the wall to be located between  $y_1^+ = 30$  and  $y_1^+ = 200$  [162]. Now the shear stress at the wall cannot be calculated exactly, and the logarithmic law of the wall as introduced in section 2.3.2 is used for an approximation instead. An overview of different techniques for the calculation of  $\tau_w$  with wall functions is provided by Bredberg [17]. Within OpenFOAM, the approach of Launder and Spalding [90] is implemented, which determines an effective viscosity at the wall.

For compressible boundary layers, an extension of the standard wall functions can be applied using a velocity transformation introduced by van Driest [169] and described in detail by White [188]. Within the law of the wall, the velocity  $u$  is replaced by an effective velocity  $u_{eff}$  to account for compressibility effects. The effective velocity is calculated using

$$u_{eff} = \frac{u_e}{b} \sin^{-1} \left( \frac{2b^2(u/u_e) - a}{\sqrt{a^2 + 4b^2}} \right) + \frac{u_e}{b} \sin^{-1} \left( \frac{a}{\sqrt{a^2 + 4b^2}} \right), \quad (4.23)$$

where

$$a = \left( 1 + r \frac{\gamma - 1}{2} M_e^2 \right) \frac{T_e}{T_w} - 1 \quad (4.24)$$

and

$$b^2 = r \frac{\gamma - 1}{2} M_e^2 \frac{T_e}{T_w}. \quad (4.25)$$

## 4 Numerical Methods

---

Here, the indices  $e$  and  $w$  denote the edge of the boundary layer and the wall, respectively.

The wall shear stress is then determined using the effective velocity. As stated by Smits and Dussauge [147], the benefit of this method is difficult to determine, although it yields good results for a variety of flows. The experimental inaccuracy is usually higher than the differences between the incompressible and the compressible wall function approach. Furthermore, several simplifications had to be made by van Driest to derive equation (4.23). Besides assuming  $Pr = 1$  in the laminar sublayer, the most restricting ones are a turbulent Prandtl number of unity and the need for the absence of any high pressure gradients.

Within the present thesis, for the vast majority of the numerical simulations the walls are resolved with  $y_1^+ \leq 1$ , as either boundary layers or wall heat transfer are investigated. An exception is the simulation of the flow inside the ITLR model combustion chamber, where the focus is on the validation of the main flow field and thus wall functions may be employed to reduce computational costs. Therefore, this case is used to compare the standard wall functions to an enhanced version containing the van Driest transformation. In addition, a setup using a fully resolved wall is employed for further comparison.

### Free-Stream Values

The free-stream values of  $k$  and  $\omega$  can be calculated by defining a turbulence intensity  $I$  for the main flow, which describes the magnitude ratio of the velocity fluctuations and the mean flow velocity. The turbulent kinetic energy in the free-stream is then calculated using

$$k_\infty = \frac{3}{2} (u')^2 = \frac{3}{2} (u_\infty I)^2 . \quad (4.26)$$

For many numerical simulations of channel flows a value of  $I$  between 2% and 10% is chosen, for the present thesis  $I$  is set to 5%. The corresponding value for  $\omega$  is calculated by

$$\omega_\infty = \frac{k_\infty}{\nu} \left( \frac{\nu_t}{\nu} \right)^{-1} \quad (4.27)$$

with the turbulent to laminar viscosity ratio  $\nu_t/\nu$ . Depending on the free-stream Reynolds number, this ratio can vary between 10 and 100 for duct flows. It is assumed to be 50 for the numerical simulations presented here.

## 4.2 Solver Development

The solver used for all numerical simulations presented in this thesis has been developed in cooperation with the Chair of Thermodynamics at the Technical University of Munich. The basic numerical environment was chosen to be OpenFOAM [78, 187], which is an acronym for *Open Field Operation and Manipulation*. It is an open-source numerical toolbox containing solvers for CFD, but also for a variety of other applications. The software is written in C++, which is, due to its object oriented nature, well suited for the highly modular design of the code. The complete package is distributed under the GNU general public license (GPL), which allows modifications and extensions of the openly accessible source code. Furthermore, in contrast to commercial CFD packages, no licenses are needed. Therefore, even massive parallelization can be realized at the net costs of processor usage time only.

In accordance with OpenFOAM nomenclature conventions, the new solver is referred to as *scramjetFoam* (*SCRf*). The solver is designed for the simulation of supersonic flows [38, 100] with chemical reactions [98, 99, 101] and conjugate heat transfer [39]. It is based on a compressible flow solver originally developed by Greenshields et al. [67], which uses the computationally efficient central discretization scheme of Kurganov and Tadmor [88] as introduced above. The solver is density-based, as the higher dissipation of a pressure-based approach would impede the accurate resolution of shock and expansion waves. Turbulence can be modeled using either RANS, as is the case within the present thesis, LES, or also a hybrid RANS/LES method [101].

The development of SCRf started with OpenFOAM version 1.7, and the final solver is based on version 2.1. The original solver of Greenshields et al. [67] has been modified to include several additional features, which will be discussed in more detail in the following. Moreover, the underlying thermophysical model based on sensible enthalpy has been replaced by a model developed by Ettner [44]. This model is based on total internal energy and, therefore, more suited for supersonic and reacting flows. A summary of the major development steps of *scramjetFoam* is provided in table 4.1.

In order to capture the temperature dependency of the fluid properties, Sutherland's law is used to obtain the dynamic viscosity. The specific heat capacity at constant pressure  $c_p$  and the static enthalpy  $h$  are calculated using the Joint Army-Navy-Air Force (JANAF) thermochemical tables as published by Chase et al. [25]. These polynomials only cover a temperature range between 200 K and 5000 K by design, which is not necessarily sufficient for static temperatures as low as they may occur in supersonic flows, especially when dealing with

## 4 Numerical Methods

---

Table 4.1: Major development steps of *scramjetFoam*

SCRF	OpenFOAM	Changes
v0.61	v1.7	Turbulence modeling is added to the density based, laminar OpenFOAM solver <i>rhoCentralFoam</i> [67].
v0.62	v2.1	Port of <i>scramjetFoam</i> to OpenFOAM v2.1.
v0.70	v2.1	Makowka [101]: Implementation of a modified thermo-physical model [44] based on total internal energy, in addition multi-species transport and chemical reactions are added.
v0.80	v2.1	Implementation of local time-stepping support to accelerate convergence. LTS additionally provides preconditioning for quasi-steady-state simulations, as the variable time step reduces disparities in the time and length scales.
v0.90	v2.1	Implementation of the OpenFOAM multi-region handling into <i>scramjetFoam</i> in preparation for the addition of conjugate heat transfer support.
v1.00	v2.1	Conjugate heat transfer and the corresponding interface boundary conditions are added. The implementation follows <i>multiRegionFoam</i> , which so far is the only standard OpenFOAM solver capable of conjugate simulations. However, it is pressure-based and only suitable for subsonic and non-reacting flows.

experiments conducted in blow-down wind tunnels. Therefore, the polynomial coefficients were adapted to also be valid for static temperatures as low as 50 K using the method and software described by McBride and Gordon [107]. These modified coefficients are listed in appendix B.

### 4.2.1 Multi-Species Transport

Within a multi-species flow, the conservation equation as presented in equation (2.3) has to be solved for each occurring species. Besides the introduction of the species mass fractions  $Y_n$  as new variables, this also requires the calculation of an effective mass diffusivity

$$D_{eff} = D_l + D_t = \frac{1}{\rho} \left( \frac{\mu}{Sc} + \frac{\mu_t}{Sc_t} \right) \quad (4.28)$$

for use in equation (2.3), which takes into account both the laminar and the turbulent mass diffusivities.

### 4.2.2 Chemical Reactions

The implementation of chemical reactions into the solver has been carried out by Makowka [101] based on the work of Ettner [44], and is described there in detail. Chemically reacting flows are not considered within the present thesis.

### 4.2.3 Conjugate Heat Transfer

For conjugate simulations, the numerical domain has to include not only the flow region, but also the investigated solid body. Within the solid body, the three-dimensional Fourier law as introduced in equation (2.22) is solved to determine the temperature distribution. A solver including this approach already exist in OpenFOAM, but due to its pressure-based approach for the fluid region it is only suitable for subsonic flows. Furthermore, it does not include the support of chemical reactions.

Within SCRF, a fluid region can be coupled with any number of solid regions. At the interface between two regions, a mixed boundary condition is applied to iteratively equalize the temperature by evaluating the heat flux across the interface. For steady-state simulation this results in

$$\dot{q}_1 = -\dot{q}_2 \tag{4.29a}$$

$$T_1 = T_2 \tag{4.29b}$$

after convergence. In case of transient simulations, internal iterations may be required to reach convergence for each physical time step. The number of internal iterations depends on the size of the time step, the wall-normal grid resolution, and the ratio of the heat conductivities of both regions.

Effects due to radiation are not taken into account in the present thesis. The physical properties of the solid body are considered to be constant, while the thermal conductivity of the fluid depends on the flow temperature. It is calculated taking into account both the laminar and the turbulent part, similar to the definition of the effective mass diffusivity in equation (4.28).

$$\lambda_{eff} = \lambda_l + \lambda_t = c_p \left( \frac{\mu}{Pr} + \frac{\mu_t}{Pr_t} \right) \tag{4.30}$$

## 4 Numerical Methods

---

The grids of the fluid and solid regions are required to feature matching cells at region interfaces. This results in a higher number of cells than necessarily needed for the solid regions, but avoids data interpolation at the interfaces and thus reduces the numerical effort if unstructured or hybrid meshes are used. For structured grids, however, this may result in higher computational costs, as local refinements directly influence the overall grid resolution and thus imply a considerable increase in the total number of cells.

A fully coupled approach is chosen to maintain the transient capabilities of SCRF, i.e. the variable exchange at the interface and the solution of the Fourier equation for the solid body is conducted at each iteration. To ensure numerical stability, in addition to the CFL number in the fluid region, also the Fourier number

$$Fo = \frac{\alpha \Delta t}{\Delta x^2} \quad (4.31)$$

can be used to limit the maximum time step for the solid regions in case of transient simulations.

### 4.2.4 Local Time-Stepping

When investigating heat transfer in supersonic flows, the time scales of fluid and solid differ considerably. While the flow usually reaches a steady state within a fraction of seconds, it will require several seconds for a solid body to develop a steady-state temperature distribution. Thus a fully coupled, transient calculation would imply enormous computational costs due to the small time step. However, when the focus is only on the steady state itself and not on its transient development, a non-uniform time step can be introduced to create a local time-stepping (LTS) as suggested by Osher and Sanders [123]. As SCRF uses a transient formulation by design, a corresponding variation of the explicit Euler scheme is implemented to allow for such quasi-steady-state simulations. The numerical time step for each cell is determined based on the local acoustic velocity ( $|u(x)| + a(x)$ ), which leads to a transformation of equation (4.1) into

$$\Delta t(x) \leq \frac{\Delta x}{(|u(x)| + a(x))} C_{max}. \quad (4.32)$$

The time uniformity across the domain is nullified by this approach, and transient effects can no longer be correctly predicted. However, as long as a steady-state flow is investigated, the numerical solution converges towards this

---

## 4.3 Additional Developments for OpenFOAM

final steady state nevertheless and does so considerably faster. A detailed run-time comparison of both time-stepping techniques is presented in section 5.2. Using LTS, the fluid region can be coupled to a steady-state simulation of the solid region, which significantly lowers the computational costs for conjugate simulations. When investigating chemical reactions, the use of LTS is not recommended due to the highly transient nature of reacting flows.

Within SCRF, the maximum local wave speed is used to compute the local values for  $\Delta t$ , as it is already available for use in the Kurganov-Tadmor discretization scheme. The time step variable is then smoothed in each iteration, as high local gradients of the time step may lead to numerical instabilities. For the same reason, a damping function is implemented to limit the change of  $\Delta t(x)$  between successive iterations.

Besides accounting for the different time scales of fluid and solid, local time-stepping also acts as preconditioning for the fluid region [171]. By introducing a variable time step in the domain depending on local cell size and acoustic velocity, the stiffness of the equation system is removed and disparities in the characteristic time and length scales are reduced. This enables the simulation of low Mach number regions with a compressible solver. Such regions will, for example, appear inside the strut injector, where the Mach number is expected to be less than 0.5. A similar approach could be used in case of fully transient simulations, where a so-called dual time-stepping method would introduce an internal pseudo-time for each physical time-step. For the internal pseudo time a mechanism like LTS could then be applied without losing accuracy of the physical time.

## 4.3 Additional Developments for OpenFOAM

In addition to the development of *scramjetFoam*, an enhanced wall function is implemented in OpenFOAM. Furthermore, several OpenFOAM tools regarding post-processing have to be modified to be compatible with the new solver, which will be addressed in the second part of this section.

### 4.3.1 Improved Wall Function

Two-dimensional numerical simulations for the ITLR model combustion chamber, which are presented in section 5.5.1, show that the wall functions originally available within OpenFOAM tend to over-predict the temperature gradient directly at the wall. One possible reason for this behavior is the neglect of

## 4 Numerical Methods

---

compressibility effects within the standard wall function. For this reason, an improved wall function is implemented in OpenFOAM, which contains a van Driest transformation for the flow velocity based on equations (4.23) to (4.25).

As discussed in detail in section 5.5.1, this change in wall functions does not have any significant influence on the general velocity profile inside the channel. However, it also does not considerably reduce the over-prediction of the temperature gradient. Still, compared to numerical simulations conducted using a commercial CFD code as employed for previous studies [173–176], the enhanced wall function provides a slightly better agreement in terms of shock positions and general temperature level across the combustion chamber.

### 4.3.2 Changes in Post-Processing Tools

Due to the changes in the thermophysical model, several OpenFOAM tools have to be adapted to restore full functionality for evaluating simulations conducted with *scramjetFoam*. Moreover, as the thermal conductivity  $\lambda$  for the fluid region is calculated directly by the solver, this can be used to simplify post-processing of heat fluxes. A summary of the relevant changes is provided in table 4.2.

Table 4.2: Adapted OpenFOAM tools

Tool	Parameters	Changes
<i>yPlus</i>	$y_1^+$	Correction of the source code, in the original version $y_1^* = \Delta y_1 C_\mu^{1/4} \sqrt{k}/\nu_w$ was calculated instead of $y_1^+ = \Delta y_1 \sqrt{(\tau_w/\rho_w)}/\nu_w$
<i>wallGradT</i>	$(\partial T/\partial n)_w, \dot{q}_w$	Adaptation to the new thermophysical model, additional calculation of the wall heat flux based on the temperature gradient and the thermal conductivity $\lambda$ of the fluid at the wall
<i>wallShearStress</i>	$\tau_w$	Adaptation to the new thermophysical model

## CHAPTER 5

---

### Solver Validation

---

Before being applied to simulate the heat loads onto the strut injector, the new solver *scramjetFoam* has to be validated. For this purpose, a set of test cases is investigated, which covers the range from basic supersonic flows and boundary layer simulations to the application of the solver to supersonic channel flows containing obstacles. In the following, the results of these test cases are presented and evaluated, thus proving the suitability of the newly developed solver. The validation cases are selected as follows:

- I. Flow over a  $15^\circ$ -wedge at  $M_\infty = 2.5$
- II. Flow over a flat plate
  - a) Adiabatic plate at  $M_\infty = 2.0$
  - b) Adiabatic plate at  $M_\infty = 4.5$
  - c) Isothermal plate at  $M_\infty = 6.0$
- III. Shock wave/boundary layer interaction at  $M_\infty = 5.0$
- IV. Channel flow inside the ITLR model combustion chamber at  $M = 2.0$  and  $M = 2.5$

## 5 Solver Validation

---

The presented reference cases have been chosen to allow a thorough validation of the solver considering the relevant flow phenomena for conjugate heat transfer. The test cases I to III are well established in literature, for case I even an analytical solution exists. Numerical reference data for cases I, IIb and IIc is provided by the Archive of NASA's National Program for Application-Oriented Research in CFD (NPARC), where results obtained with the Wind-US code are available online for a wide range of validation cases. For test cases IIa and III also numerical data from literature, but obtained with other solvers, is used as reference. Case IV has been extensively investigated both experimentally and numerically directly at ITLR within previous projects.

### 5.1 15°-Wedge

A turbulent, supersonic flow over a wedge is considered as first test case in order to verify the correct simulation of basic supersonic flow phenomena. The wedge angle is set to  $\theta = 15^\circ$  and the free-stream Mach number of the incoming flow is  $M_\infty = 2.5$ . For an ideal gas with a specific heat ratio of  $\gamma = 1.4$ , an analytical solution for the flow conditions downstream of the shock wave can be calculated using the oblique shock relations as presented in section 2.3.1. In addition to the analytical solution, also numerical reference data from the NPARC validation archive [121] is available.

#### 5.1.1 Numerical Setup

Figure 5.1 shows the two-dimensional computational domain for the wedge flow. The origin of the coordinate system is positioned directly at the leading edge of the wedge. The numerical mesh consists of approximately 19 000 grid cells with a dimensionless wall distance at the wedge of  $y_1^+ \leq 1$ , which results in a height for the first cell at the wall of  $2.5 \cdot 10^{-6}$  m.

The flow enters the domain via the inlet at fixed static flow conditions for  $p$ ,  $T$  and  $u$ , which are derived from the total flow conditions of the reference case. A symmetry plane is used at the bottom of the domain upstream of the wedge to guarantee a homogeneous incoming flow at the wedge itself. For the upper domain boundary a free-stream condition is applied, which is valid as the shock wave only crosses the domain boundary at the outlet. Table 5.1 provides an overview of all relevant boundary conditions.

Turbulence is modeled using the SST model. At the domain inlet a turbulence intensity of  $I = 5\%$  is applied. All simulations are conducted using second order

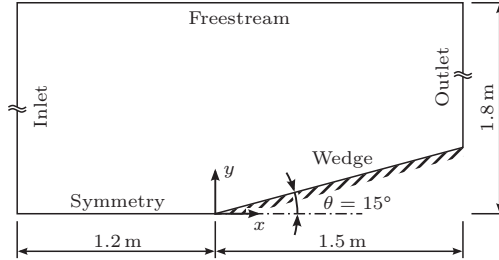


Figure 5.1: Flow over a 15°-wedge, numerical setup

accuracy schemes in space and first order accuracy in time. Transient time discretization using the Euler scheme and local time-stepping are compared to prove that the use of LTS does not imply a loss in result quality. For calculations using LTS, a considerably lower computational time is expected, even though a maximum CFL number of 0.2 has to be ensured for stability reasons. Compared to the fully transient simulations with  $C_{max} = 0.4$ , this implies a reduction of the maximum possible time step by 50%.

Table 5.1: Flow over 15°-wedge, boundary conditions

	$p_s$	$T_s$	$u$
Inlet	101.30 kPa	288.89 K	851.75 m/s
Outlet	$\partial p / \partial n = 0$	$\partial T / \partial n = 0$	$\partial u / \partial n = 0$
Wedge	$\partial p / \partial n = 0$	$\partial T / \partial n = 0$	0.00 m/s
Freestream	$\partial p / \partial n = 0$	$\partial T / \partial n = 0$	851.75 m/s

### 5.1.2 Results

A shock angle of  $\beta = 36.95^\circ$  is obtained from the analytical solution, which corresponds to a Mach number of  $M = 1.873$  downstream of the shock. Using this Mach number, the static pressure ratio over the shock wave can be calculated to  $p_s/p_\infty = 2.468$ . Figure 5.2 shows the comparison of the analytically obtained pressure ratio and the numerical results of both the NASA reference data and the simulations using SCRF. Regarding the wedge surface good agreement of numerical and analytical results is achieved, as presented in figure 5.2a. The position and the magnitude of the pressure rise are captured well by both codes. Small oscillations can be observed in all the numerical data downstream

## 5 Solver Validation

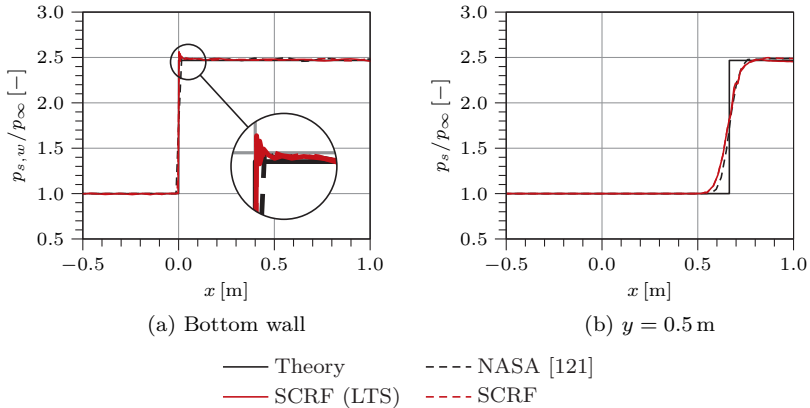


Figure 5.2: Flow over a  $15^\circ$ -wedge, pressure ratio  $p/p_{\infty}$  at different locations

of the shock, which are caused by the discretization schemes and cannot be avoided. These oscillations are most pronounced directly at the shock, where an overshoot of static pressure is observed as shown in the magnified part of figure 5.2a. When comparing the results for SCRF with and without the use of LTS, differences are only observed within the oscillating region of the solution. Both the shock position and its magnitude are captured correctly. However, using LTS provides a reduction of 78 % in computational time despite the lower maximum CFL number.

Considering a cut through the flow field along a line at  $y = 0.5$  m as shown in figure 5.2b, a characteristic phenomenon for numerical simulations can be observed. While the analytical solution represents a sharp discontinuity in the pressure ratio, the numerical results exhibit a smeared shock wave. This is due to the discretization of the flow into volumes of a certain size and the resulting finite resolution of the domain. However, for SCRF again no significant deviations between the transient calculations and the one using LTS can be observed.

In addition to the evaluation of the static pressure, also the predicted shock wave angle is determined. Figure 5.3 shows a contour plot of the Mach number distribution. The black dashed line represents the averaged numerical shock wave, which is used for a graphical estimation of the approximate shock angle. Due to the slight widening of the shock wave towards the outlet of the domain this graphical method is not completely exact, but it is still sufficient for the

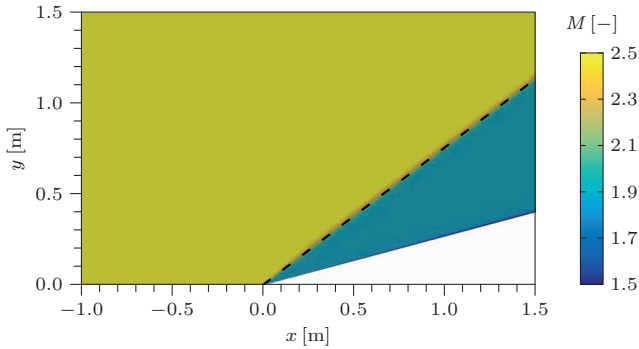


Figure 5.3: Flow over a 15°-wedge, Mach number distribution (averaged shock wave is indicated by dashed black line)

present purpose. The shock angle  $\beta$  is found to be approximately  $37.2^\circ$ , which is identical for both the transient and the LTS simulations. This agrees well with the analytical value of  $\beta = 36.95^\circ$ .

Based on these results, a correct prediction of shock waves by the solver is verified. In addition, it is shown that the use of a local time-stepping technique does indeed speed up convergence considerably. At the same time, the good overall result accuracy is maintained.

## 5.2 Flat Plate

Not only the correct capture of main flow phenomena like shock and expansion waves has to be ensured for the numerical simulation of conjugate heat transfer, but also the accurate prediction of the boundary layer at the investigated surface is critical. Therefore, turbulent flows over a flat plate are considered as second test case.

Different flow Mach numbers are investigated, and both adiabatic and isothermal plates are taken into account. As for the wedge flow, results of simulations with and without LTS are compared to extend the validation of the local time-stepping. Furthermore, the influence of the turbulent Prandtl number and of different interpolation schemes for flux reconstruction is investigated.

### 5.2.1 Numerical Setup

The two-dimensional numerical setup is shown in Fig. 5.4. In terms of boundary conditions, it is similar to the one of the wedge flow as presented above in section 5.1. Again, a short symmetry plane upstream of the plate is used to realize a homogeneous flow at the leading edge of the plate, while a free-stream boundary is defined at the upper border of the domain. This numerical setup is identical for all three investigated Mach numbers, only the value of  $\Delta y_1$  is adapted to the respective flow Mach number to ensure  $y_1^+ \leq 1$  for all simulations.

### 5.2.2 Adiabatic Plate, $M_\infty = 2.0$

The flow over an adiabatic flat plate with a free-stream Mach number of  $M_\infty = 2.0$  is evaluated first. This case has been experimentally investigated by Coles [26], in addition numerical data obtained with the DLR Tau code by Wollenhaupt [192] is available for comparison. The relevant boundary conditions for this validation case are listed in table 5.2.

Reference data is available for both the velocity and the thermal boundary layer profiles at a distance of  $x = 0.546$  m along the flat plate. Moreover, the local skin friction coefficient

$$c_{f,x} = \frac{\tau_w}{\frac{1}{2}\rho u_\infty^2} = \frac{2\mu_w}{\rho u_\infty^2} \left( \frac{\partial u}{\partial n} \right)_w \quad (5.1)$$

has been determined [26, 192]. It is a measure for the velocity gradient perpendicular to the wall, and is thus well suited for the analysis of boundary layer simulations.

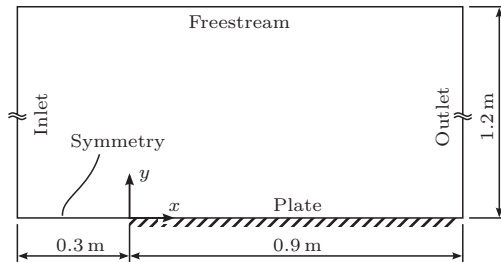


Figure 5.4: Flow over a flat plate, numerical setup

Table 5.2: Flow over adiabatic flat plate at  $M_\infty = 2.0$ , boundary conditions

	$p_s$	$T_s$	$u$
Inlet	12.44 kPa	169.56 K	517.33 m/s
Outlet	$\partial p/\partial n = 0$	$\partial T/\partial n = 0$	$\partial u/\partial n = 0$
Plate	$\partial p/\partial n = 0$	$\partial T/\partial n = 0$	0.00 m/s
Freestream	$\partial p/\partial n = 0$	$\partial T/\partial n = 0$	517.33 m/s

Figure 5.5 shows the dimensionless velocity and static temperature profiles in the boundary layer at  $x = 0.546$  m, which corresponds to a local Reynolds number of  $Re_x = 6.3 \cdot 10^6$  and is located well downstream of boundary layer transition from laminar to turbulent. Thus, a fully turbulent approach like the SST turbulence model can be used. For both profiles reasonable agreement to the numerical reference data is obtained, while the experimental measurements exhibit an offset to all numerical simulations. This is probably due to uncertainties within the experimental flow conditions and the measurement of the flow profiles, as the data cannot be reproduced exactly by neither SCRF nor Tau.

Regarding the thermal boundary layer, a slight deviation is observed compared to the numerical reference data, which is not visible for the velocity boundary layer. This is due to the fact that the turbulent Prandtl number is set to unity

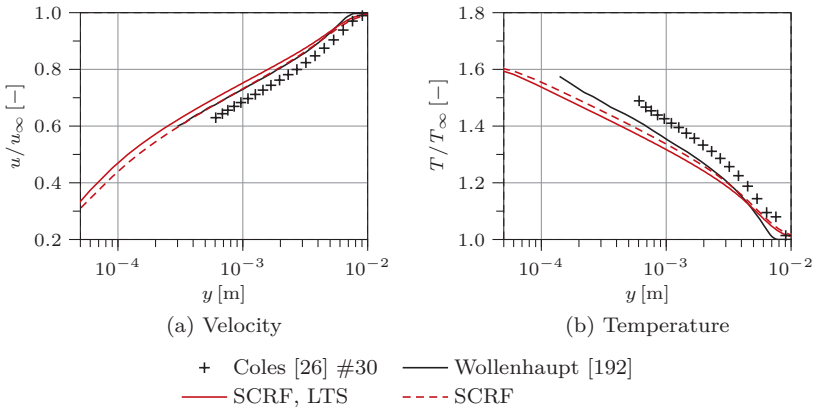


Figure 5.5: Flow over an adiabatic flat plate at  $M_\infty = 2.0$ , boundary layer profiles at  $x = 0.546$  m

## 5 Solver Validation

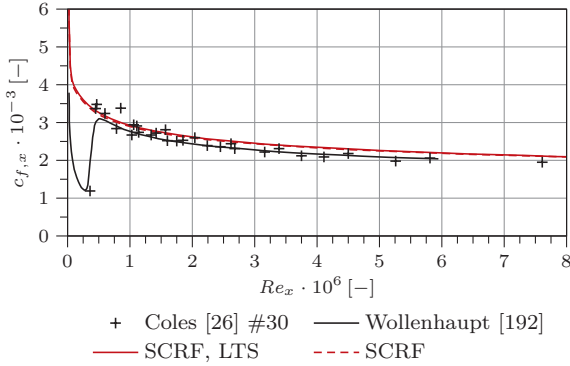


Figure 5.6: Flow over an adiabatic flat plate at  $M_\infty = 2.0$ , skin friction coefficient

in the simulations of Wollenhaupt [192], while for SCRF a value of  $Pr_t = 0.85$  was used. This effect is investigated in more detail in the following section.

In contrast to the wedge flow discussed in section 5.1, here the profiles obtained from the transient calculation and those from the simulation using LTS are not completely identical. However, the deviation between the two approaches is small. It is probably due to the fact that quasi-steady-state simulations exhibit no fluctuations at all when converged, while for the transient calculations small oscillations remain near the wall. Therefore, it can be concluded that the use of LTS still yields acceptable results. This is supported by the distribution of the local friction coefficient along the plate as shown in figure 5.6. Here, no deviation at all is found between the transient and the steady-state calculation, which implies that the velocity gradient directly at the wall is predicted identically.

A good agreement compared to the reference data is achieved for the fully turbulent section of the plate. The laminar and the transitional region near the leading edge cannot be reproduced due to the choice of the SST turbulence model, which is not able to predict transition in its standard version. Capturing these effects requires a suitable transition model as was used by Wollenhaupt, which is not yet available for *scramjetFoam*.

### Influence of the Turbulent Prandtl Number

Since the value of the turbulent Prandtl number in case of an approximation by a constant is debated in literature, the influence of a change in  $Pr_t$  is evaluated

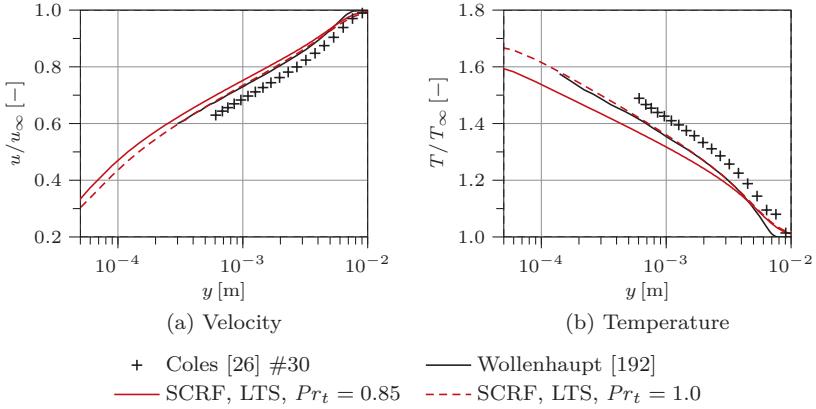


Figure 5.7: Flow over an adiabatic flat plate at  $M_\infty = 2.0$ , influence of  $Pr_t$  on the boundary layer profiles at  $x = 0.546$  m

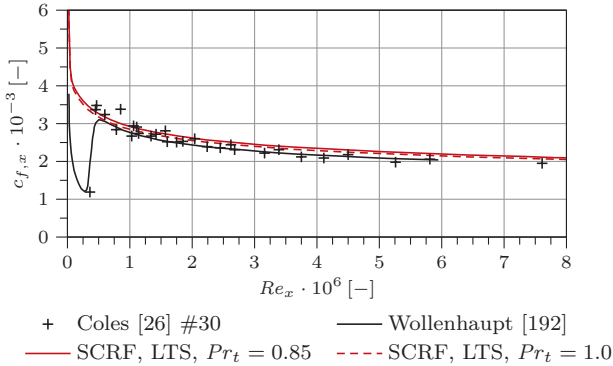


Figure 5.8: Flow over an adiabatic flat plate at  $M_\infty = 2.0$ , influence of  $Pr_t$  on the skin friction coefficient

for the current validation case. As discussed in section 4.1.2, a standard value of  $Pr_t = 0.85$  is set for all simulations within the present thesis. Figure 5.7 shows the effect of a change to  $Pr_t = 1$ , which was used for the reference calculations of Wollenhaupt [192]. Only quasi-steady-state simulations are considered for the detailed evaluation of the influence of both the turbulent Prandtl number

## 5 Solver Validation

---

and the numerical settings, as they proved to deliver comparable results to the transient calculations.

The influence of a change in  $Pr_t$  on the velocity boundary layer is small. It is caused by a change in turbulent enthalpy transport. However, for the thermal boundary layer the deviation between SCRF and the simulations using Tau vanishes nearly completely, except for the very edge of the boundary layer. Compared to the lower value of  $Pr_t$ , a rise in adiabatic wall temperature is observed, as the turbulent thermal diffusivity is reduced. This results in a lower turbulent heat flux perpendicular to the wall.

Regarding the skin friction as presented in figure 5.8, a change of  $Pr_t$  exhibits no significant influence. This agrees with the fact that the velocity profile inside the boundary layer, and therefore also the velocity gradient at the wall, only show minor deviations, as compressibility effects are still small at the investigated Mach number.

### Influence of the Flux Reconstruction Scheme

Besides the effect of the value of  $Pr_t$ , also the influence of different numerical schemes for the flux reconstruction is investigated. As already discussed in section 4.1.1, two schemes are investigated: The TVD scheme of van Leer [170] and the Gamma scheme [77]. Different blending constants are evaluated for the Gamma scheme, including  $\Gamma = 1$ , which is not recommended due to a high amount of numerical diffusion. However, high values of  $\Gamma$  support numerical stability and are therefore suited for the start-up phase of complex calculations before switching to lower values.

Figure 5.9 depicts the boundary layer profiles for the different numerical settings, including three values for  $\Gamma$ . As expected, for  $\Gamma = 1$  significant deviations are found compared to the other numerical simulations, which are due to the increase in numerical diffusion. To put the seemingly better fit to the experimental data for  $\Gamma = 1$  into perspective, the aforementioned uncertainties in the experimental measurements have to be taken into account.

Thus, despite being beneficial to ensure a stable start-up of simulations, the accuracy of the results for  $\Gamma = 1$  is not considered satisfactory in comparison with the other simulations. For lower values of  $\Gamma$ , the results agree well with the scheme of van Leer and the numerical reference data. However, it can also be seen that a decrease in  $\Gamma$  below 0.5 does not lead to a change in results any more. Since the risk of numerical instabilities increases with lower  $\Gamma$  [77], an optimum range of  $1/6 \leq \Gamma \leq 1/2$  is determined.

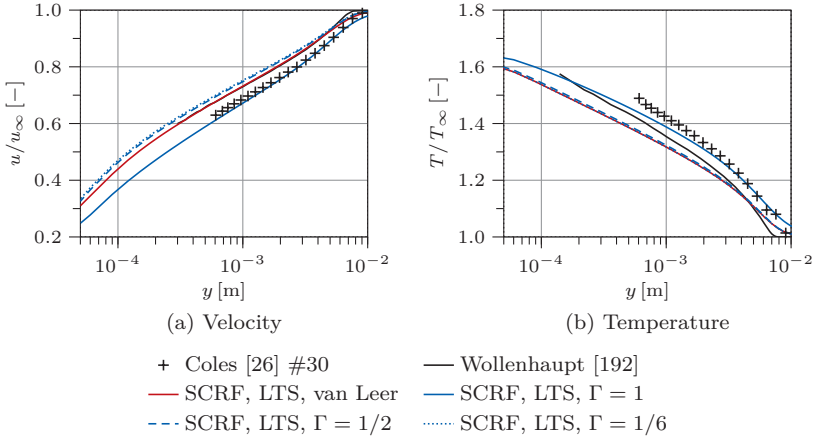


Figure 5.9: Flow over an adiabatic flat plate at  $M_\infty = 2.0$ , influence of the flux reconstruction scheme on the boundary layer profiles at  $x = 0.546$  m

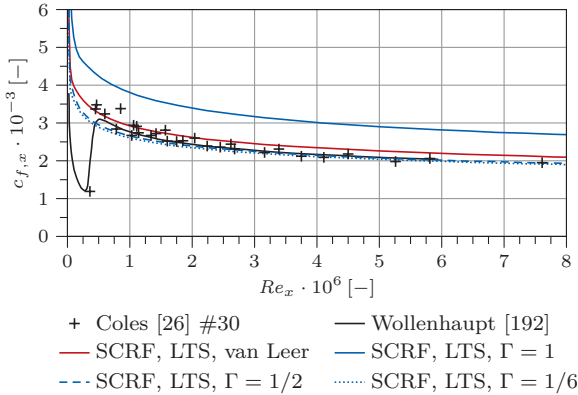


Figure 5.10: Flow over an adiabatic flat plate at  $M_\infty = 2.0$ , influence of the flux reconstruction scheme on the skin friction coefficient

A similar conclusion is obtained from the skin friction distribution as shown in figure 5.10. Again the results for  $\Gamma = 1$  are off, while no difference in results is found when comparing blending factors of  $1/2$  and  $1/6$ . Compared to van Leer's

## 5 Solver Validation

---

scheme, the Gamma scheme predicts slightly lower skin friction, but both the results for  $\Gamma = 1/2$  and  $\Gamma = 1/6$  are in the range of the experimental data.

### 5.2.3 Adiabatic Plate, $M_\infty = 4.5$

To expand the results of  $M_\infty = 2.0$  to higher Mach numbers, a second adiabatic flat plate at  $M_\infty = 4.5$  is investigated. Again experimental reference data of Coles [26] is available, numerical simulations have been conducted by NASA [120] using the Wind-US code. Due to the increased Mach number and the significantly lower density, the unchanged boundary layer profile location at  $x = 0.546$  m now corresponds to a local Reynolds number of  $Re_x = 3.7 \cdot 10^6$ . A detailed list of boundary conditions is provided in table 5.3.

The extremely low static temperature of only 60 K is caused by the experimental setup of Coles [26], where the total temperature was fixed at approximately 305 K independently of the flow Mach number. This illustrates the importance of a low-temperature modification of the polynomials used for the calculation of the thermophysical properties, as was described in section 4.2.

The velocity and thermal boundary layer profiles are shown in figure 5.11. Excellent agreement with both experimental and numerical data is obtained for the velocity profile. Regarding the temperature profile, in the outer part of the boundary layer the data agrees well. However, similar to the investigation at  $M_\infty = 2.0$ , SCRF predicts a lower adiabatic wall temperature. This is probably again caused by the difference in turbulent Prandtl number, since also the numerical reference data of NASA is presumed to have been obtained at  $Pr_t = 1$ . This issue will be discussed in more detail in the following section.

The skin friction distribution, as presented in figure 5.12, also exhibits good agreement of both numerical simulations. Due to the experimental approach of Coles [26], where the measurement devices were installed at three different stations downstream of the plate leading edge to capture the whole length of

Table 5.3: Flow over adiabatic flat plate at  $M_\infty = 4.5$ , boundary conditions

	$p_s$	$T_s$	$u$
Inlet	0.67 kPa	60.47 K	703.29 m/s
Outlet	$\partial p / \partial n = 0$	$\partial T / \partial n = 0$	$\partial u / \partial n = 0$
Plate	$\partial p / \partial n = 0$	$\partial T / \partial n = 0$	0.00 m/s
Freestream	$\partial p / \partial n = 0$	$\partial T / \partial n = 0$	703.29 m/s

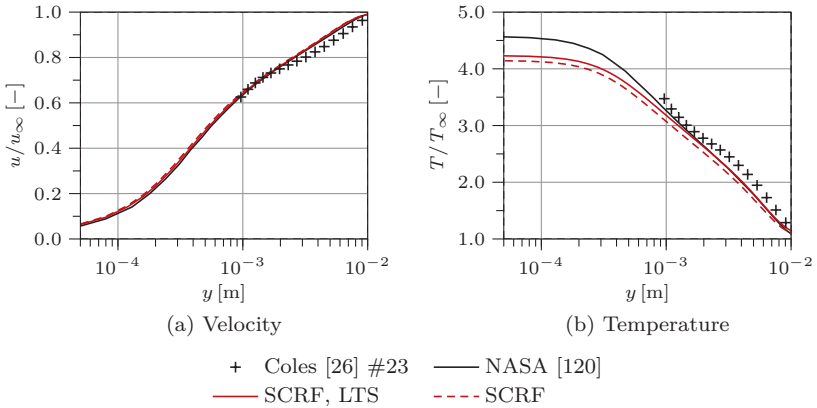


Figure 5.11: Flow over an adiabatic flat plate at  $M_\infty = 4.5$ , boundary layer profiles at  $x = 0.546$  m

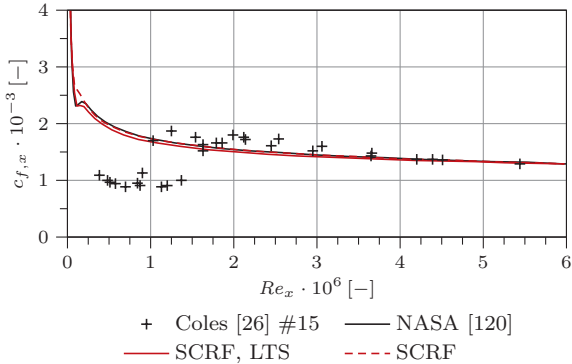


Figure 5.12: Flow over an adiabatic flat plate at  $M_\infty = 4.5$ , skin friction coefficient

the plate, the transitional region was measured slightly different by each device. This leads to an apparent duplication and shifting of the experimental data in figures 5.12, 5.14 and 5.16. However, this only affects the transition from laminar to turbulent flow at up to  $Re_x = 2 \cdot 10^6$ . As neither the computations of NASA nor the ones conducted with SCRf use a transition model, the

## 5 Solver Validation

experimental data in this region is not matched. For the fully turbulent part of the plate at higher local Reynolds numbers, however, the experimental measurements of all three measurement stations confirm the prediction of the numerical simulations.

### Influence of the Turbulent Prandtl Number

To verify the reason for the recurring deviation of the thermal boundary layer profile, the turbulent Prandtl number is varied again for SCRF. The resulting boundary layer profiles are shown in figure 5.13.

While the velocity profile matches well, the adiabatic wall temperature obtained with SCRF for a higher turbulent Prandtl number approaches the one predicted by NASA. This finding implies, that, although not documented within the reference case description [120], Wind-US indeed applies a turbulent Prandtl number of unity. Furthermore, the adiabatic wall temperature predicted for  $Pr_t = 1$  exceeds the one for  $Pr_t = 0.85$ , which has already been observed for the adiabatic plate at  $M_\infty = 2.0$ . However, here the effects are limited to the inner boundary layer, the outer part remains mostly unchanged and matches the experimental data for both values of  $Pr_t$ .

Due to the fact that the velocity near the wall is not affected by a change in turbulent Prandtl number at  $M_\infty = 4.5$ , the same is the case for the local skin

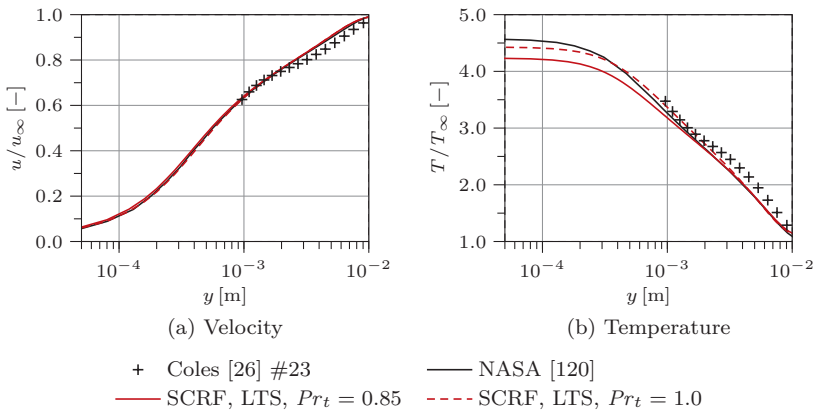


Figure 5.13: Flow over an adiabatic flat plate at  $M_\infty = 4.5$ , influence of  $Pr_t$  on the boundary layer profiles at  $x = 0.546$  m

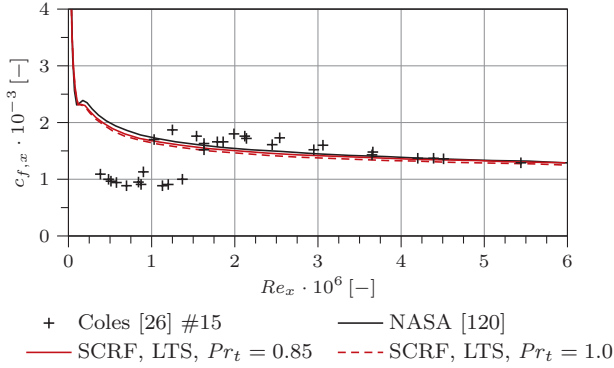


Figure 5.14: Flow over an adiabatic flat plate at  $M_\infty = 4.5$ , influence of  $Pr_t$  on the skin friction coefficient

friction, which is presented in figure 5.14. This confirms the findings for  $c_{f,x}$  of the similar test case at  $M_\infty = 2.0$ . Furthermore, it leads to the conclusion that an accurate prediction of the main flow field is still possible using the default value of  $Pr_t = 1$ .

If the thermal boundary layer is relevant, however, a detailed evaluation of the turbulent Prandtl number is recommended. Even a small change in  $Pr_t$  can lead to a significant alteration in wall temperature. Furthermore, it will have an influence on the wall heat flux in case of non-adiabatic walls.

### Influence of the Flux Reconstruction Scheme

Lastly, also for  $M_\infty = 4.5$  the influence of the flux reconstruction scheme is evaluated. To maintain comparability to the previous investigations at  $M_\infty = 2.0$ , identical coefficients for the Gamma scheme are chosen. The resulting boundary layer profiles are depicted in figure 5.15. Deviations are only observed for  $\Gamma = 1$ , while values of 0.5 and smaller are able to reproduce the simulations using the scheme of van Leer regarding both the velocity and the thermal boundary layer. For the low values of  $\Gamma$ , the results are also in better accordance with the reference simulations.

Similar to the simulation at  $M_\infty = 2.0$ , the skin friction coefficient is overpredicted for  $\Gamma = 1$ . Figure 5.16 shows that all other schemes match the reference

## 5 Solver Validation

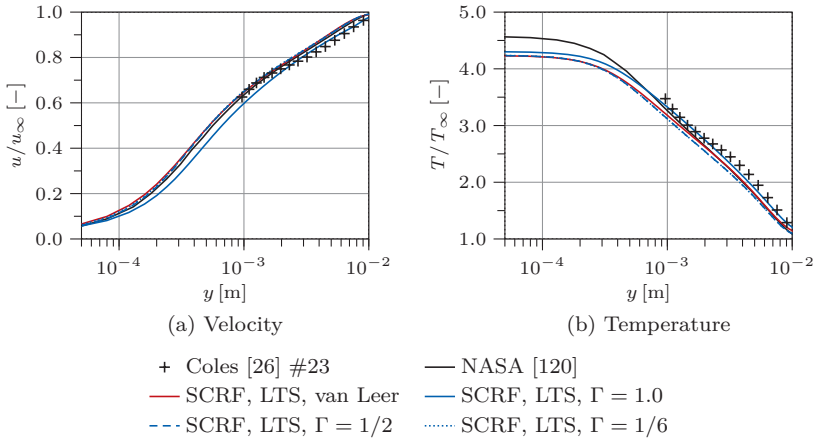


Figure 5.15: Flow over an adiabatic flat plate at  $M_\infty = 4.5$ , influence of the flux reconstruction scheme on the boundary layer profiles at  $x = 0.546$  m

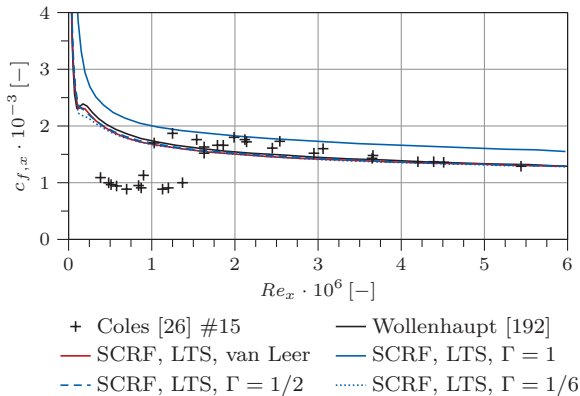


Figure 5.16: Flow over an adiabatic flat plate at  $M_\infty = 4.5$ , influence of the flux reconstruction scheme on the skin friction coefficient

data, and especially the reference simulations, very well. Virtually no difference is found between  $\Gamma = 1/2$  and  $\Gamma = 1/6$ , which agrees with the results for the boundary layer profiles. This shows that, independently of the flow Mach

number, the value of  $\Gamma$  can be chosen between  $1/6$  and  $1/2$  without a loss of accuracy. Lower values than  $1/6$  were found to result in severe numerical instabilities, which has also been stated by Jasak et al. [77]. Furthermore, they do not provide any further benefit in terms of accuracy. Therefore, within the present thesis a standard value of  $\Gamma$  will be  $1/2$  in case the Gamma scheme is used.  $\Gamma = 1$  will only be applied during start-up of the simulations to improve stability, before switching to lower values for the remaining part of the simulations.

### 5.2.4 Isothermal Plate, $M_\infty = 6.0$

Isothermal walls are of special interest for the numerical investigation of heat transfer, as they represent a technically relevant boundary condition. Furthermore, due to the presence of a heat flux across the wall, this type of boundary condition is particularly relevant for the investigation of the strut injector and the surrounding channel flow as discussed in chapter 6. Therefore, an isothermal flat plate at  $M_\infty = 6.0$  is considered in addition to the adiabatic plates discussed above. Experimental heat transfer data of Bertram et al. [9] is used for comparison, the experiments were conducted for a temperature ratio of  $T_w/T_t = 0.6$ . A full list of boundary conditions is given in table 5.4.

In addition, numerical data obtained by Dilley [36] is available, including both skin friction and heat transfer distributions. As these simulations were conducted using a transition model, only the fully turbulent part of the boundary layer can be compared to SCRF. The skin friction distribution along the plate is shown in figure 5.17. Simulations have been conducted for both  $Pr_t = 0.85$  and  $Pr_t = 1$ , as Dilley [36] does not specify the value used for his calculations. Furthermore, numerical reference data is only available up to a local Reynolds number of  $Re_x = 12 \cdot 10^6$ .

Apart from the transitional region, the skin friction coefficient is predicted within the correct range by SCRF independently of the turbulent Prandtl

Table 5.4: Flow over isothermal flat plate at  $M_\infty = 6.0$ , boundary conditions

	$p_s$	$T_s$	$u$
Inlet	2.21 kPa	65.04 K	969.94 m/s
Outlet	$\partial p/\partial n = 0$	$\partial T/\partial n = 0$	$\partial u/\partial n = 0$
Plate	$\partial p/\partial n = 0$	320.00 K	0.00 m/s
Freestream	$\partial p/\partial n = 0$	$\partial T/\partial n = 0$	969.94 m/s

## 5 Solver Validation

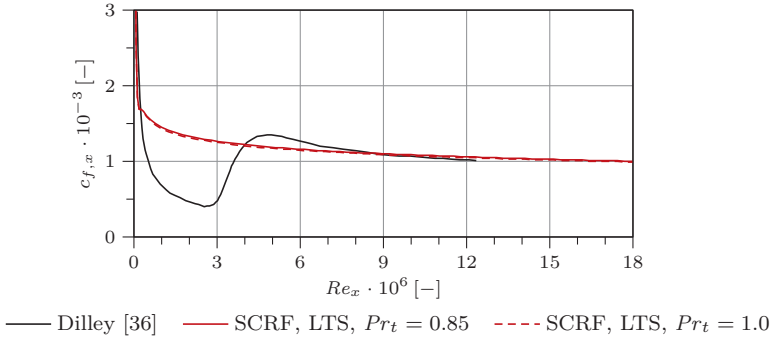


Figure 5.17: Flow over an isothermal flat plate at  $M_\infty = 6.0$ , skin friction coefficient

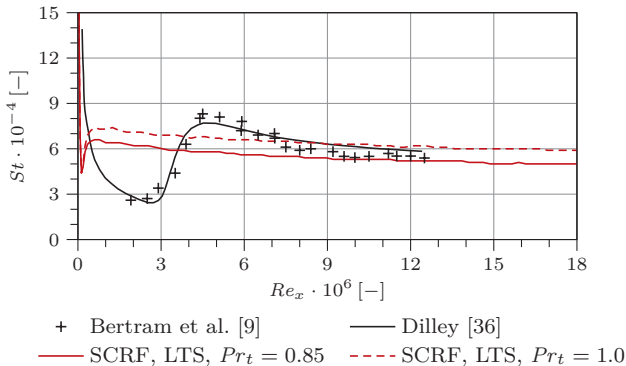


Figure 5.18: Flow over an isothermal flat plate at  $M_\infty = 6.0$ , Stanton number

number, which confirms the results obtained for the adiabatic plates. In addition, the Stanton number as introduced in equation (2.26) is evaluated. The distribution of  $St$  along the plate is presented in figure 5.18, where a clear influence of  $Pr_t$  on the results is visible.

In the fully turbulent region both turbulent Prandtl numbers do not exactly match the reference data, but they delimit the experimental Stanton number range with acceptable accuracy. While for  $Pr_t = 1.0$  the numerical data is reproduced better, for  $Pr_t = 0.85$  the results are in closer agreement with the experimental data. This suggests that the assumption of a turbulent Prandtl

---

## 5.3 Shock Wave/Boundary Layer Interaction

number below unity is indeed more physically correct, and furthermore backs the surmise that the numerical simulations of Dilley were conducted using  $Pr_t = 1.0$ . However, the results also show the limitations of the constant turbulent Prandtl number approach in terms of overall result accuracy.

### 5.2.5 Computational Costs for Transient and LTS Simulations

The computational costs of LTS and fully transient simulations are compared in figure 5.19 for the flat plate cases. Here, the ratio of computational time using LTS to the computational time for a transient simulation is plotted. The values for the supersonic flow over the wedge are included for the sake of completeness. The convergence criteria are identical for all investigated cases. Even with the lower maximum CFL number for LTS, as discussed in section 5.1, a substantial run-time reduction between 55 % and 78 % can be realized. Since the accuracy of the results obtained from LTS calculations has been verified, all further simulations will use the local time-stepping approach.

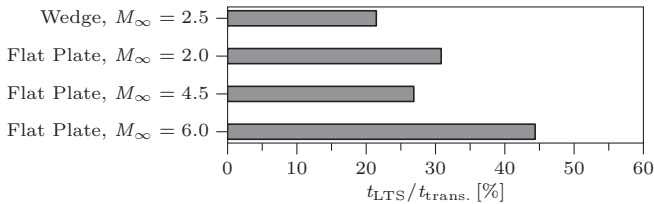


Figure 5.19: Computational cost reduction of test cases using LTS

For numerical simulations including conjugate heat transfer, the reduction in computational costs is expected to be higher by several orders of magnitude due to the need to simulate several seconds of flow in case of transient calculations. For the cases presented so far, typically a few milliseconds of simulated physical time are sufficient to achieve full convergence, which roughly corresponds to the flow passing through the domain at least two times.

## 5.3 Shock Wave/Boundary Layer Interaction

When investigating supersonic flows, and especially when dealing with channel flows, the interaction of shock and expansion waves with a boundary layer is a

## 5 Solver Validation

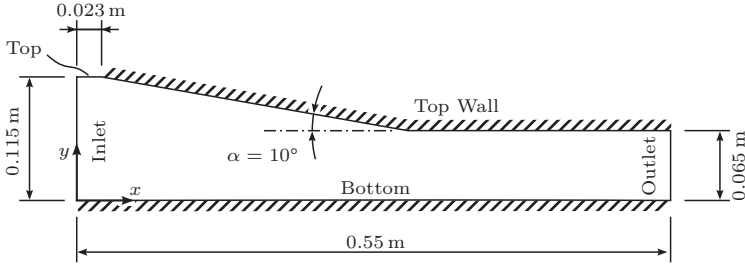


Figure 5.20: Shock wave/boundary layer interaction, numerical setup

relevant issue. A suitable two-dimensional test case has been examined experimentally by Schülein et al. [140], who later published additional results [141] for the same case. They investigated the impact of an oblique shock wave, which was created by inserting a shock generator plate into the flow, onto a flat plate boundary layer at  $M_\infty = 5.0$ . The experimental data set includes shadowgraphs, pressure measurements and skin friction as well as Stanton number distributions. Numerical simulations for this setup have been conducted by Fedorova and Fedorchenko [46] and by Lindblad et al. [95]. Both studies used the Wilcox  $k-\omega$  turbulence model [189], but employed different CFD codes. Lindblad also investigated different algebraic Reynolds stress models based on the  $k-\omega$  formulation. To ensure comparability of the modeling approach, the discussion in the present section is limited to two-equation models. A schematic of the numerical setup is shown in figure 5.20.

The leading edge of the top wall serves as shock generator and is positioned such that the resulting shock wave impinges onto the bottom target plate at  $x = 350$  mm. Due to the short duration of the experiments, the walls can be considered to be approximately isothermal at 300 K. A symmetry plane is imposed at the top to ensure a smooth inflow at the shock generator leading edge. A detailed list of boundary conditions is provided in table 5.5.

Table 5.5: Shock wave/boundary layer interaction at  $M_\infty = 5.0$ , boundary conditions

	$p_s$	$T_s$	$u$
Inlet	4.07 kPa	68.33 K	828.50 m/s
Outlet	$\partial p / \partial n = 0$	$\partial T / \partial n = 0$	$\partial u / \partial n = 0$
Top Wall, Bottom	$\partial p / \partial n = 0$	300.00 K	0.00 m/s

### 5.3 Shock Wave/Boundary Layer Interaction

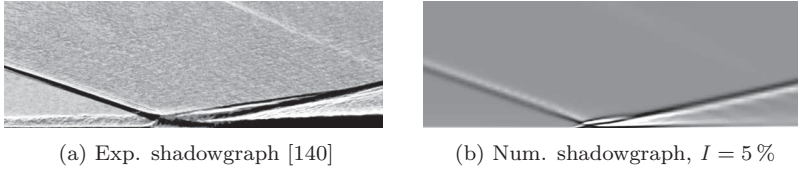


Figure 5.21: Shock wave/boundary layer interaction at  $M_\infty = 5.0$ , shadowgraph images

As the prediction of skin friction and Stanton number is heavily depending on the initial turbulence intensity  $I$ , simulations were conducted for two different values of  $I$ , namely 5% and 1%. While the first value corresponds to the standard setting for turbulent channel flows, the second one better represents low-turbulence wind tunnel conditions.

A general overview of the resulting flow field can be obtained from shadowgraphs, which represent the second derivative of the refraction index, and thus of the density within the investigated flow. Figure 5.21a shows the experimental data, which is compared to the numerical shadowgraph as presented in figure 5.21b. The angles of both the incident shock wave and the reflected shock are correctly reproduced, also the characteristic thickening of the boundary layer at the point of impact is present in the numerical results. The turbulence intensity at the inlet is found to have only negligible effect on the overall flow field.

For a more detailed analysis of the flow, the static wall pressure distribution along the target plate is evaluated. Figure 5.22 presents the results obtained with SCRF, which agree well with both the experimental and parts of the numerical reference data. As explained in chapter 2, the initial pressure rise occurs slightly upstream of the actual impact position, which is correctly predicted by the simulation. The pressure levels upstream and downstream of the shock impact are also accurately reproduced. A deviation is observed compared to the data of Lindblad et al. [95], where boundary layer separation occurs further downstream and also the static pressure level after reattachment is underestimated. Similar to the results for the general flow field, the level of turbulence intensity at the inlet is not found to have a major influence on the pressure distribution.

Figure 5.23 shows the distribution of the local skin friction coefficient along the target plate. Here, a significant influence of the inlet turbulence level is observed. Besides slightly changing the onset of boundary layer thickening and recirculation upstream of the shock impact, also the overall level of skin

## 5 Solver Validation

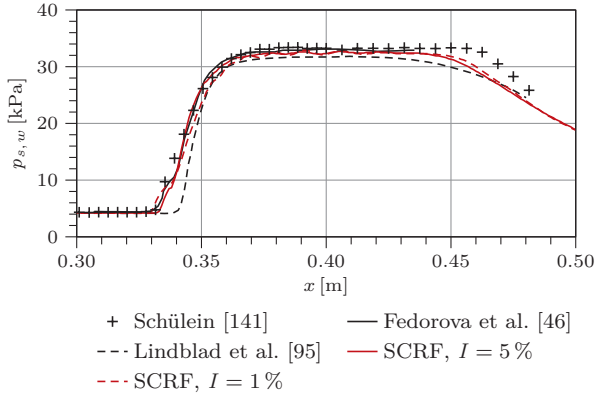


Figure 5.22: Shock wave/boundary layer interaction at  $M_\infty = 5.0$ , static wall pressure distribution

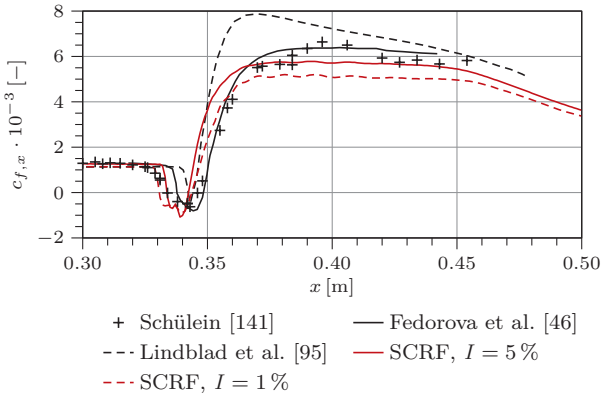


Figure 5.23: Shock wave/boundary layer interaction at  $M_\infty = 5.0$ , skin friction coefficient

friction is affected. When comparing the different numerical simulations, it is evident that both the size and the position of the separation zone are differing between the codes. This issue cannot be identified by only evaluating the static wall pressure as shown in figure 5.22. Lindblad et al. [95] predict a smaller separation zone with an overshoot in skin friction downstream, which would

### 5.3 Shock Wave/Boundary Layer Interaction

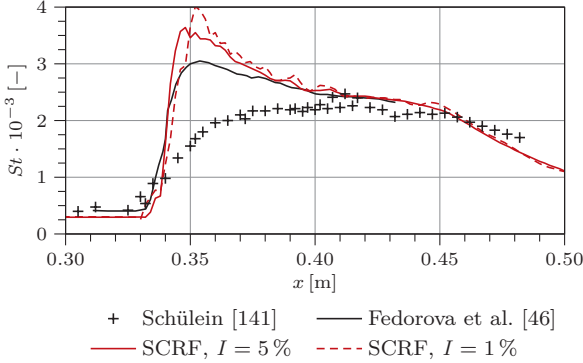


Figure 5.24: Shock wave/boundary layer interaction at  $M = 5.0$ , Stanton number

usually be attributed to the  $k-\omega$  turbulence model. However, Fedorova and Fedorchenko [46], who use the same turbulence model, obtain better results with a more pronounced separation region, which leads to the conclusion that this is either caused by the numerical code itself, or the initial turbulence settings of the simulations must have been different. The simulations using SCRf predict a larger separation zone slightly more upstream. This can be expected, as the SST model is known to overestimate boundary layer separation [110]. The overall skin friction level is matched for  $I = 5\%$ , while for a lower initial turbulence intensity the level of the experimental data is not reached.

Regarding the heat transfer at the target plate as shown in figure 5.24, severe discrepancies between numerical simulations and experimental data are observed, which are most pronounced around the shock impact location. The Stanton number magnitude is overestimated by the numerical simulations in the area between 0.34 m and 0.4 m, while for the rest of the domain reasonable results are obtained. This overshoot at the direct location of the shock wave/boundary layer interaction is a common issue [37], and is most likely caused by the use of two-equation turbulence models. It has also been observed for similar applications, and is attributed by some authors [117, 163] to a local overproduction of turbulent kinetic energy.

Despite the discrepancies in Stanton number for the separation region, the velocity and temperature profiles inside the boundary layer are generally matched well downstream of the shock impact location. Figure 5.25 shows the relevant profiles in comparison to the experimental data. Numerical reference data is only available for the velocity profiles. Significant deviations with

## 5 Solver Validation

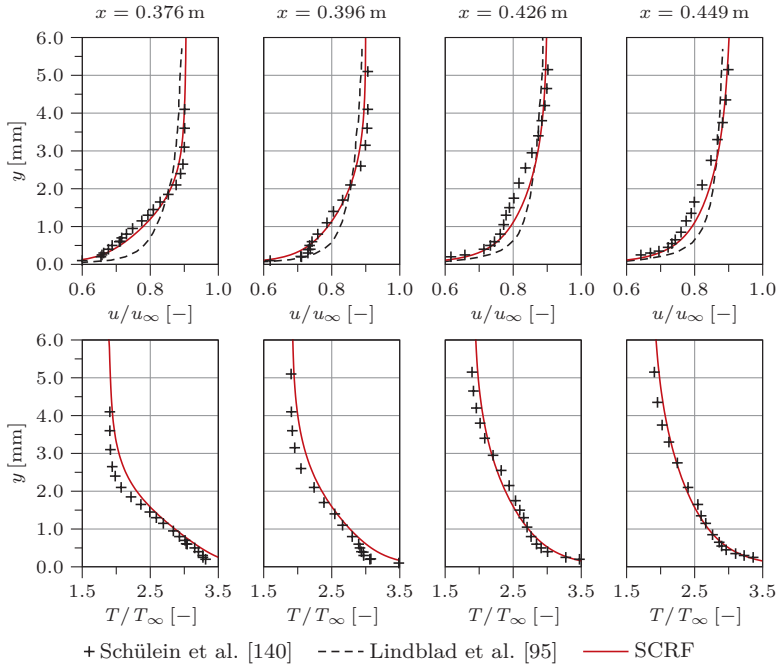


Figure 5.25: Shock wave/boundary layer interaction at  $M_\infty = 5.0$ , boundary layer profiles downstream of the shock impact location

respect to the experimental data are only found for the temperature profiles directly downstream of the shock impact at  $x = 0.376 \text{ m}$  and  $x = 0.396 \text{ m}$ . With increasing distance from this part of the plate, the deviations diminish more and more. Compared to the simulations of Lindblad et al. [95] with the  $k-\omega$  model, the choice of the SST model for SCRf shows clear benefits. Here, the velocity in the near-wall region of the boundary layer agrees noticeably better with the experimental measurements. The use of a more sophisticated Reynolds stress model could provide comparable results [95], but would cause significantly higher computational costs.

Using the data presented in figure 5.25, the velocity boundary layer thickness at the evaluated locations is determined. A comparison to the experimental values is provided in table 5.6. The boundary layer thickness is overestimated directly downstream of the shock impact, which confirms the larger separation zone

## 5.4 Intermediate Summary: Numerical Settings

Table 5.6: Shock wave/boundary layer interaction at  $M_\infty = 5.0$ , boundary layer thickness  $\delta$  at selected cross sections

	$x = 0.376$ m	$x = 0.396$ m	$x = 0.426$ m	$x = 0.449$ m
Schülein et al. [140]	2.651 mm	3.364 mm	4.466 mm	4.837 mm
SCRf	3.050 mm	3.650 mm	4.400 mm	4.550 mm

as identified based on the skin friction distribution. Further downstream, the boundary layer thickness approaches the experimental data, which is combined with better agreement of both skin friction and Stanton number in this region. Towards the end of the domain, the boundary layer is predicted to be slightly thinner by the CFD.

## 5.4 Intermediate Summary: Numerical Settings

Based on the previous validation cases, several findings regarding the numerical settings can be summarized. This leads to the setup for the following simulations. Firstly, the use of local time-stepping provides a considerable reduction of the computational costs, while at the same time producing comparable results to the fully transient simulations. Secondly, despite the influence of the constant value for the turbulent Prandtl number on the adiabatic wall temperature, a value of  $Pr_t = 0.85$  yields reasonable results for all validation cases and will thus be maintained.

Lastly, no significant deviation is found between the use of van Leer's scheme and the Gamma scheme, as long as  $\Gamma \leq 1/2$ . However, preliminary studies for the ITLR combustion chamber [118] have shown that van Leer's scheme, although being numerically more efficient, is prone to numerical instabilities near the walls when using a coarse mesh with wall functions. Therefore, in the following it is only used in case of resolved walls with  $y_1^+ \leq 1$ . The Gamma scheme with  $\Gamma = 1/2$  is employed for all simulations using wall functions.

## 5.5 Model Combustion Chamber

To expand the solver's range of application towards supersonic channel flows, the ITLR model combustion chamber is considered next for validation. Only non-reacting conditions are taken into account. To maintain comparability to the experimental reference data, the outer geometry of the strut injector

## 5 Solver Validation

Table 5.7: Overview of numerical simulations for the ITLR model combustor

$T_t$	Wall function	Air inj.	2D		3D	
			$M = 2.0$	$M = 2.5$	$M = 2.0$	$M = 2.5$
390 K	Standard [90]	yes	-	-	X	X
1300 K	-	no	X	X	-	-
1300 K	Standard [90]	no	X	X	X	X
1300 K	Standard [90]	yes	-	-	X	X
1300 K	v. Driest [169]	no	X	X	-	-

is included nevertheless. A flattened version is used for the two-dimensional simulations, for the three-dimensional test cases both the strut and the wall ramp injectors are modeled accurately without any geometrical simplifications.

Table 5.7 provides an overview of the presented simulations, parts of which have been conducted in the framework of a diploma thesis at ITLR [118]. Mach numbers of 2.0 and 2.5 are evaluated. Furthermore, the accuracy of the numerical wall-treatment is assessed for the two-dimensional setup by comparing fully resolved simulations to calculations using wall functions. Both the standard wall functions and the enhanced version as discussed in section 4.3.1 are investigated.

For the three-dimensional simulations not only the hot gas flow, which corresponds to the standard experimental conditions, but also a cold flow was taken into account to allow for a comparison to conventional schlieren imaging. This technique exhibits an increased field of view compared to the focusing schlieren system, and thus provides a better overview of the general flow field. For the comparison to the schlieren imaging, air is injected at the trailing edge of the strut, while only the main air flow is considered for the rest of the simulations.

The numerical domain for the three-dimensional simulations is displayed in figure 5.26. The channel side wall is blanked for reasons of clarity. Only half of the combustion chamber is modeled by exploiting symmetry along the vertical center plane (marked blue in figure 5.26). For the two-dimensional simulations, the symmetry plane and the channel side wall are collapsed and the wall ramps are omitted. The cross sections at  $x = 0.4$  m and  $x = 0.6$  m mark the locations where flow profiles are extracted for evaluation.

The critical cross section of the Laval nozzle is defined to be the domain inlet. Sonic flow conditions corresponding to the total temperature and total pressure during experiments are prescribed. The inlet boundary conditions for all investigated cases are listed in table 5.8. Both the walls and the injector are set

## 5.5 Model Combustion Chamber

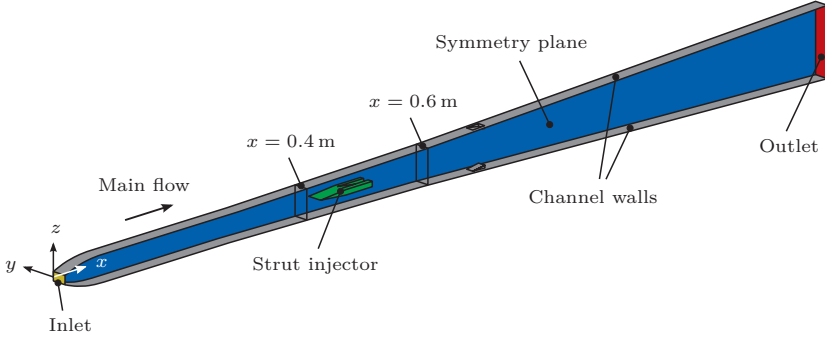


Figure 5.26: ITLR model combustor, numerical domain

Table 5.8: Inlet conditions for ITLR model combustor

	$p_t$	$p_s$	$T_t$	$T_s$	$u$
$M = 2.0$	0.4 MPa	0.217 MPa	390 K	336.6 K	356.72 m/s
$M = 2.0$	0.4 MPa	0.217 MPa	1300 K	1122.04 K	651.29 m/s
$M = 2.5$	0.6 MPa	0.326 MPa	390 K	336.6 K	356.72 m/s
$M = 2.5$	0.6 MPa	0.326 MPa	1300 K	1122.04 K	651.29 m/s

to  $T_w = 300$  K for the cold gas conditions. In case of the hot gas simulations, the channel walls are considered to be isothermal due to water-cooling during experiments and are set to  $T_w = 400$  K. The strut injector is assumed to be at 600 K, as it is directly exposed to the hot gas while being internally cooled in the experiments. A constant backpressure of  $p = 96$  kPa is applied at the channel outlet to account for the adaptation to ambient pressure in the experimental channel.

### 5.5.1 Two-Dimensional Simulations

Besides evaluating the flow profiles at two locations inside the combustor, the two-dimensional simulations are used to address the issue of wall treatment. As listed in table 5.7, several approaches, including different wall functions, are investigated and compared to numerical reference simulations conducted by Vellaramkalayil [176]. These simulations were performed using the commercial CFD software CFD++. A finer resolution of the combustor walls and the

## 5 Solver Validation

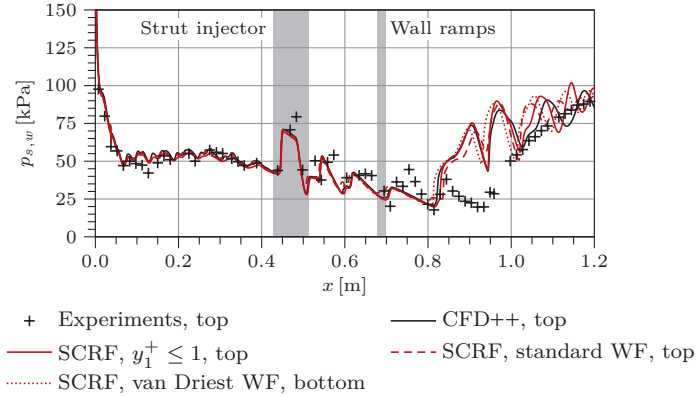


Figure 5.27: ITLR model combustor (2D), static wall pressure for  $M = 2.0$

injector to avoid the use of wall functions was not considered for the reference cases due to limited computational resources.

Figures 5.27 and 5.28 show the static wall pressure distributions for  $M = 2.0$  and  $M = 2.5$ , respectively. In addition to the reference simulations, also experimental data [176] is included. Note that for selected simulations with SCRF the bottom wall pressure is displayed, as for these cases the inclination of the combustor exit shock train is inverted compared to the other simulations. As already discussed in section 2.3.2, the shock train exhibits an asymmetrical behavior despite the symmetrical geometry of the combustion chamber. While the shock train is usually inclined in the experiments due to small geometrical irregularities, a varying inclination is observed in the numerical simulations despite the completely symmetrical grid. This does not affect the flow profile locations at  $x = 0.4$  m and  $x = 0.6$  m, but has a significant influence on the static wall pressure towards the channel exit.

For  $M = 2.0$ , the simulations agree well for both codes. The onset of the shock train is predicted similarly, but not all of the shock train features can be resolved due to the geometrical simplifications. The difference in the pressure oscillations towards the combustor exit indicates a slightly different prediction of the boundary layer separation. At  $M = 2.5$ , the static pressure level upstream of the shock train is reduced due to the higher flow velocity. Furthermore, the shock train onset is shifted upstream to  $x = 0.75$  m. Again all the simulations yield similar results for the different wall treatment approaches.

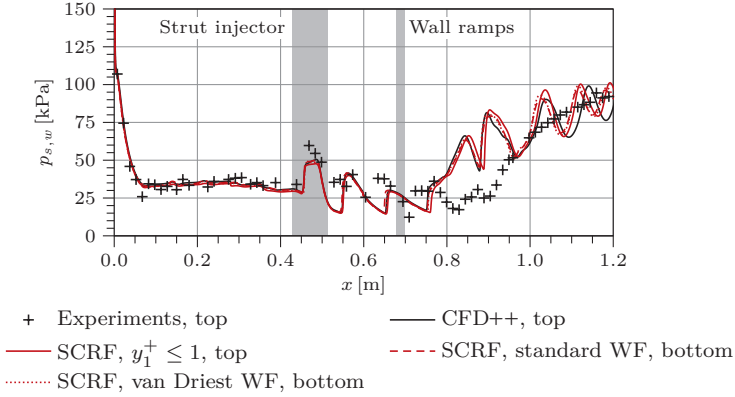


Figure 5.28: ITLR model combustor (2D), static wall pressure for  $M = 2.5$

A comparison of the temperature and velocity profiles at  $x = 0.4\text{m}$  and  $x = 0.6\text{m}$  for  $M = 2.0$  is shown in figure 5.29. As can be seen in figure 5.29a, regarding the temperature profile of the undisturbed flow upstream of the injector at  $x = 0.4\text{m}$ , the use of any wall function with SCRF leads to a considerably higher flow temperature in the vicinity of the walls. In the center of the flow, the temperature level is within the range of the reference simulations again. Resolving the walls down to  $y_1^+ \leq 1$  reduces the temperature gradient at the wall, but at the same time slightly lowers the general temperature level in the center of the combustor. Independently of the chosen wall treatment, good agreement is achieved for the velocity profile as presented in figure 5.29b.

A similar behavior is found further downstream, where the influence of the strut injector can be observed at  $x = 0.6\text{m}$ . Shock and expansion waves, which originate at the strut, are propagating through the flow field. As shown in figure 5.29c, this leads to a distorted temperature profile with an increase in static temperature in the wake of the injector. While the use of standard wall functions results in the highest temperature near the top and bottom walls, accounting for compressibility effects with a van-Driest-correction, as introduced in section 4.3.1, slightly reduces the temperature within this region. Again the avoidance of wall functions results in a lower near-wall temperature, which coincides better with the reference simulations at this location. The corresponding velocity profile, which is depicted in figure 5.29d, is only slightly affected by the change in wall treatment. Here, the standard wall functions predict a slightly thicker boundary layer compared to all other approaches.

## 5 Solver Validation

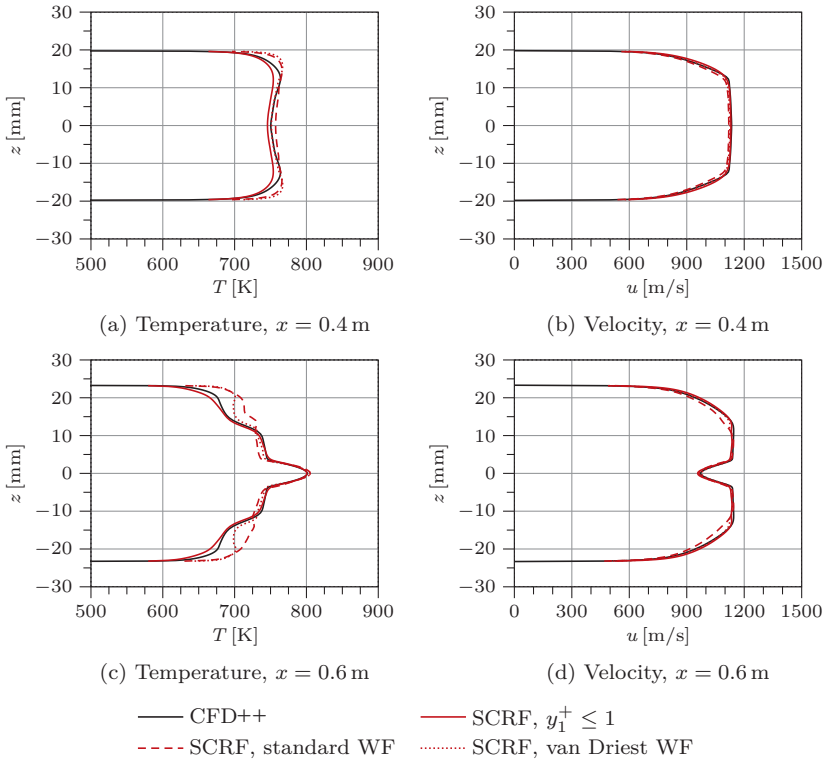


Figure 5.29: ITLR model combustor (2D), flow profiles for  $M = 2.0$

As shown in figure 5.30a for  $M = 2.5$ , the effect of an increase in Mach number on the temperature profile of the undisturbed flow is correctly predicted. Now the static temperature in the center of the flow is lower compared to the vicinity of the walls. Similar to the results for  $M = 2.0$ , both wall functions result in an about 5% higher temperature near the walls, while matching the reference data for the core flow. A contrary effect regarding the wall-near region is achieved when avoiding wall functions. However, these deviations are not reflected in the undisturbed velocity profile as depicted in figure 5.30b, where all data agrees well.

Besides the issues already discussed, the disturbed flow at  $x = 0.6$  m exhibits an additional phenomenon compared to the flow field at  $M = 2.0$ . Figures 5.30c

## 5.5 Model Combustion Chamber

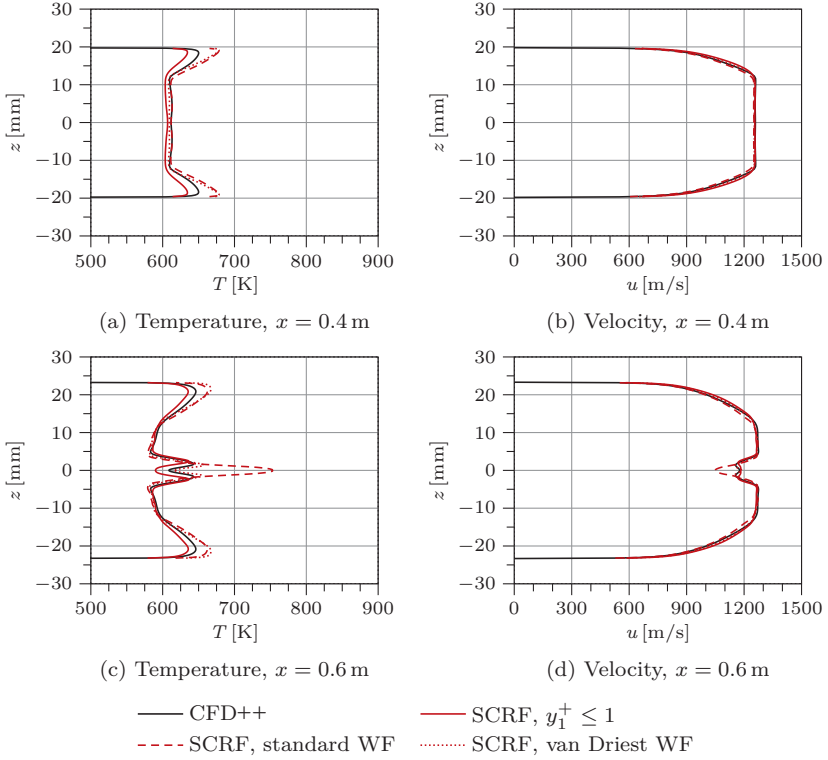


Figure 5.30: ITLR model combustor (2D), flow profiles for  $M = 2.5$

and 5.30d show that the shock system is shifted slightly for the different wall treatments. This results in considerable deviations of temperature and velocity inside the core flow between the different wall treatment approaches. While the standard wall function predicts a shock crossing to be located directly upstream of the investigated plane, which results in higher temperature and lower velocity, this crossing is located further downstream for all other simulations.

Based on these findings, it is concluded that the use of wall functions for highly compressible flows in SCRf cannot be recommended for the investigation of heat transfer due to the pronounced uncertainty in the wall temperature gradient. It has to be noted that the reference data is also a numerical simulation, and thus not necessarily completely accurate, but considering all results a clear trend

## 5 Solver Validation

---

of SCRF to overestimate wall-near temperatures when using wall functions is observed. The implementation of a compressibility correction into this wall function does affect the location of the shock pattern inside the channel, but has only little effect on the temperature gradient at the wall. Yet, it is shown that the modification tends to match the general flow pattern slightly better, and the results are closer to simulations without wall functions as well as to the reference data. This comes at the price of an increase in computational costs due to the more complex formulation of the wall function itself. For a detailed prediction of heat transfer, however, it is inevitable to ensure a wall resolution of  $y_1^+ \leq 1$ .

### 5.5.2 Three-Dimensional Simulations

In addition to the two-dimensional investigations presented above, three-dimensional simulations of the combustion chamber are conducted to investigate the effects of the lobed strut injector onto the flow field in more detail. The standard wall functions are used to minimize computational costs for these complex simulations, as the main focus is on the general flow field.

#### Investigation of the Cold Combustor Flow

To evaluate the overall flow field inside the combustion chamber, experimental schlieren images were first obtained for cold flow conditions at  $T_t = 390$  K using a conventional schlieren setup. Compared to the focusing schlieren setup used at higher temperatures, the conventional setup provides advantages regarding both field of view and sensitivity. Thus, it allows a more detailed comparison to the numerical simulations.

In order to maintain comparability to the hot gas conditions as discussed in section 5.5.2, where the internal cooling of the strut cannot be deactivated, air is also injected for the cold flow conditions in both the experiment and in the numerical simulation. A combination of numerical and experimental schlieren for both investigated Mach numbers is shown in figure 5.31. The main flow inside the combustor is nearly symmetrical with respect to the  $x$ - $y$ -plane, therefore only the upper half of the flow is considered for the schlieren images. The lower halves of the figures represent the mirrored experimental schlieren for the upper channel half. On the left of the images, the trailing edge of the strut injector is visible. The leading edge of the wall ramp injectors can be seen at the top and bottom channel walls on the right hand side.

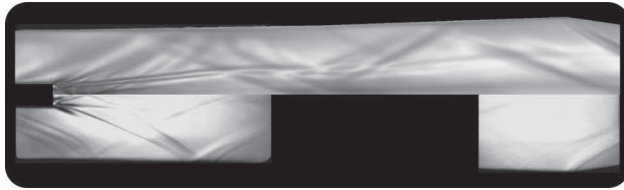
(a)  $M = 2.0$ (b)  $M = 2.5$ 

Figure 5.31: ITLR model combustor, composite of numerical (top half) and experimental (bottom half, mirrored) schlieren images at  $T_t = 390$  K with activated air injection

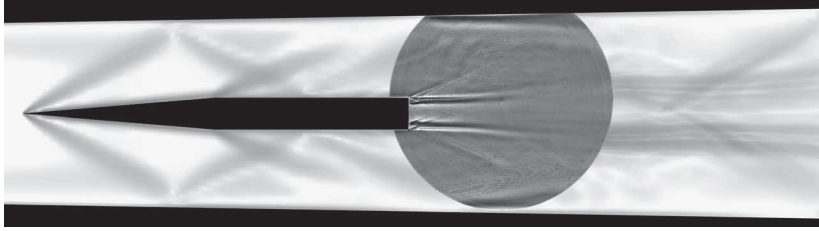
The shock and expansion system originating at the trailing edge is predicted well by the numerical simulations. Also the bow shock of the wall ramps is correctly reproduced. Comparing the different Mach numbers, the reduction of the shock inclination angles due to the higher flow velocity is visible in both the experimental and the numerical data. For  $M = 2.5$ , the shock system in the wake of the injector is stretched axially and the shock impact locations at the top and bottom walls are shifted further downstream. This leads to the conclusion that the main flow features are correctly captured by the numerical simulations independently of the flow Mach number.

### Investigation of the Hot Combustor Flow

A more extensive validation of the combustor flow field is conducted for  $T_t = 1300$  K, which corresponds to the standard experimental conditions for combustion tests. Before going into detail about the flow profiles, at first again schlieren images and also the static wall pressure distributions are evaluated. In contrast to the schlieren images presented above for  $T_t = 390$  K, which were obtained with a conventional schlieren setup, for the hot gas conditions a focusing schlieren system as described in section 3.2.4 has to be used. To

## 5 Solver Validation

---



(a) Flow field around the injector, experimental data is displayed in the circle



(b) Detailed view, experimental data is displayed in the bottom half

Figure 5.32: ITLR model combustor, composite of focusing schlieren and numerical schlieren images ( $\partial\rho/\partial z$ ) at  $M = 2.5$  and  $T_t = 1300$  K with activated air injection

eliminate the influence of the temperature gradients, the depth of focus is designed to be within the range of the combustor width. Figure 5.32a presents an overview of the flow field around the strut injector by means of a composite image containing both numerical and experimental schlieren. The field of view of the experimental setup is limited to the circle downstream of the strut.

The flow field visible in the experimental data blends in well with the numerical simulation, especially the dispersion of the coolant air stream injected through the strut matches well. A more detailed view of the trailing edge is shown in figure 5.32b, where the experimental data is depicted in the lower half of the domain and the numerical schlieren are shown in the upper half section. Due to the limited sensitivity of the experimental setup, discrepancies regarding the shock system occur directly at the trailing edge. The intensity of the density gradients varies most in this region, and weaker waves cannot be resolved by the focusing schlieren setup. However, the features visible in the experimental images are correctly reproduced by the numerical simulations.

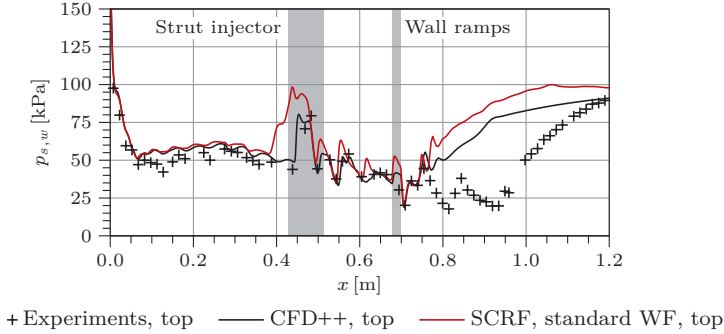


Figure 5.33: ITLR model combustor (3D), static wall pressure for  $M = 2.0$

The static wall pressure distributions for the hot gas conditions at  $M = 2.0$  and  $M = 2.5$  are shown in figures 5.33 and 5.34, respectively. The bottom wall pressure is shown in case the shock train inclination is inverted. Compared to the two-dimensional results shown in figures 5.27 and 5.28, in the three-dimensional simulations the onset of the shock train is located further upstream between  $x = 0.70$  m and  $x = 0.75$  m. This is caused by the wall ramps, which were neglected for the two-dimensional studies. They induce additional shocks and thus support flow separation.

For  $M = 2.0$ , a significant deviation between the simulations occurs at the strut injector. In contrast to the reference data, SCRF predicts flow separation slightly upstream of the injector, combined with a local increase in static wall pressure. Due to the geometrical simplification of the strut, the same effect is not observed in the two-dimensional simulations. When increasing the flow Mach number to  $M = 2.5$ , the separation zone at the strut vanishes as can be seen in figure 5.34. Here, both codes predict similar results around the injector and also match the experimental data.

The shock train inclination is inverted for SCRF at  $M = 2.5$ , but this does not affect the onset point. It is located further upstream in the three-dimensional study, but still does not influence the flow profile at  $x = 0.6$  m, which is chosen for a detailed evaluation. While the overall pressure level is identical up to around  $x = 0.65$  m, SCRF exhibits a slightly higher pressure at the combustion chamber exit compared to the reference simulations. This indicates a shorter and more intense shock train, and it also matches the nominal combustor exit pressure of  $p = 96$  kPa better. The reason might be the more flexible exit boundary condition in CFD++. Instead of the fixed value condition used for

## 5 Solver Validation

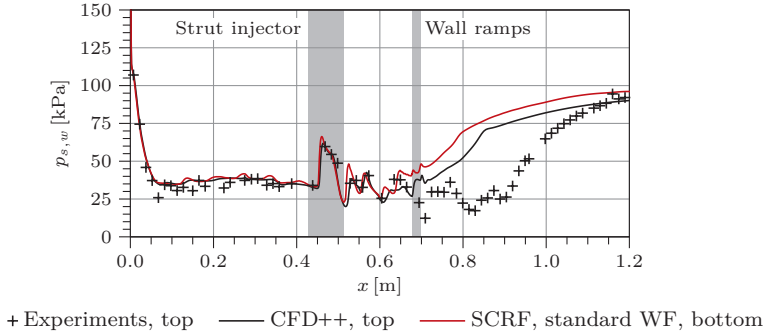


Figure 5.34: ITLR model combustor (3D), static wall pressure for  $M = 2.5$

SCRF, CFD++ uses a wave transmissive boundary condition. It does not apply the ambient pressure directly at the outlet plane, but introduces a buffer zone instead to avoid a reflection of shock waves which might cross the exit plane.

In addition to the static wall pressure, also the same two cross-sections as for the two-dimensional analysis are investigated. This enables a comparison of the undisturbed region upstream of the strut and the flow affected by the lobed trailing edge further downstream. The flow profiles for  $M = 2.0$  are depicted in figure 5.35. The left side of each comparison represents the data obtained with SCRF, and on the right side the corresponding reference data [176] is shown.

In general, the findings of the two-dimensional investigations are confirmed here. The temperature level for SCRF is increased due to the wall functions, which is combined with a lower velocity in the combustor. The cooler region in the center of the flow, as observed in figure 5.35a, is due to a slightly different position of the oblique shock system inside the combustor. The large separation region, which has been identified using the static wall pressure, is already clearly visible in the velocity plot at  $x = 0.4$  m presented in figure 5.35b. Also the full extent of the flow separation can be seen here, as the separation bubble is even more pronounced in the corners due to the sharp combustor edges.

When considering the flow field downstream of the strut as shown in figures 5.35c and 5.35d, the effects of the lobed trailing edge are observed in the distributions of both temperature and velocity. Apart from the mentioned shift in absolute level between the two numerical codes, the streamwise vorticity in the wake of the injector is causing the expected characteristic flow pattern in both cases.

## 5.5 Model Combustion Chamber

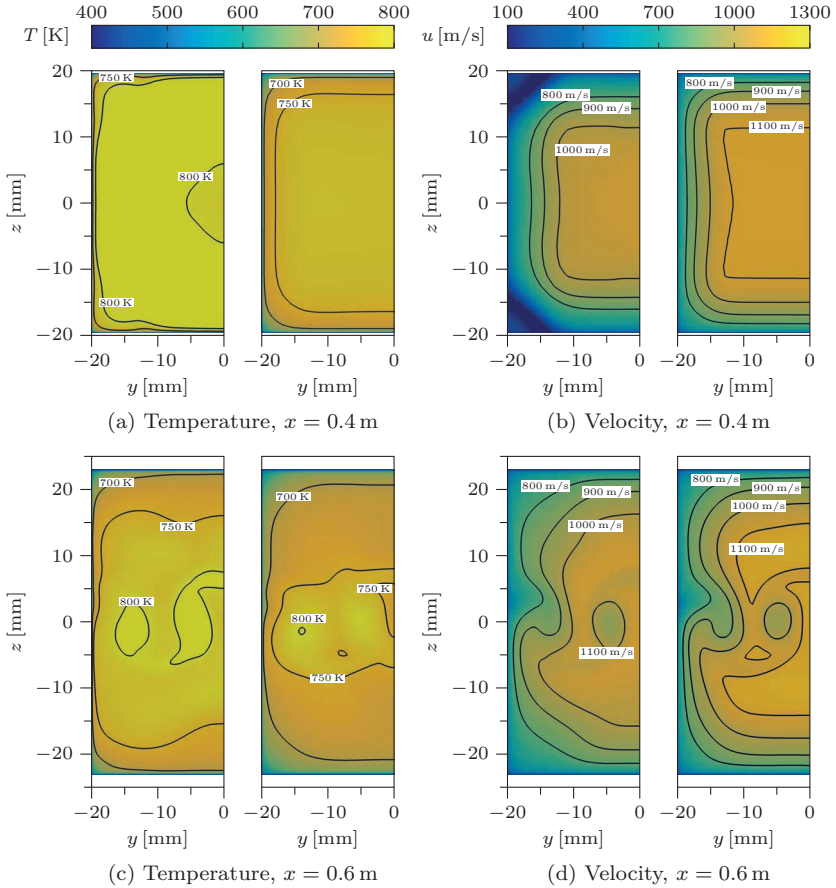


Figure 5.35: ITLR model combustor (3D), flow profiles for  $M = 2.0$  (left: SCRF, right: CFD++)

As depicted in figures 5.36a and 5.36b, the separation region upstream of the strut is not present anymore for  $M = 2.5$  due to the increase in flow velocity, the smaller critical Laval nozzle cross section and the corresponding decrease in mass flow. The oblique shock system seems to be positioned similarly for both simulations, a central shock crossing is not observed at the chosen position for either simulation. Downstream of the

## 5 Solver Validation

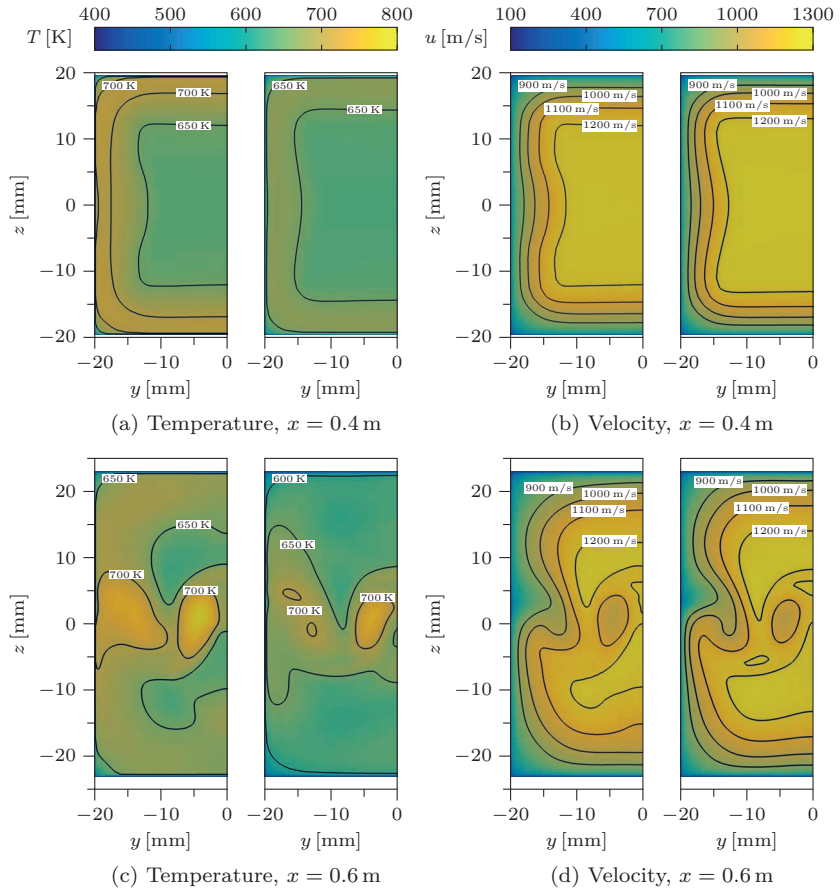


Figure 5.36: ITLR model combustor (3D), flow profiles for  $M = 2.5$  (left: SCRF, right: CFD++)

injector, the temperature and velocity fields as shown in figures 5.36c and 5.36d are similar to the ones predicted for  $M = 2.0$  in terms of vortex shape. The swirl, however, is slightly more pronounced for the higher Mach number. Despite the over-prediction of the temperature level near the walls for SCRF, both codes agree even better for  $M = 2.5$ , as the velocity field is predicted to be nearly identical not only in shape, but also in absolute values.

## 5.6 Summary

The capabilities of *scramjetFoam* have been demonstrated for a variety of validation cases available from both literature and in-house experiments. Several key aspects of supersonic flows and heat transfer have been shown to be reproduced correctly by the solver for different flow Mach numbers. This includes boundary layers and shock waves as well as their interaction. Also channel flows were considered, as they are especially relevant for the conjugate simulations described in the following chapter. Altogether, SCRF was found to perform well for these validation cases, and is thus considered a suitable tool for the numerical simulations of supersonic flows. Besides the capabilities discussed above, *scramjetFoam* also exhibits a very good scaling behavior on high performance computing architectures, as shown in appendix D for the High Performance Computing Center in Stuttgart (HLRS).

Regarding solver settings and mesh requirements, two key findings have been obtained as a result of the validation: Firstly, while the use of wall functions might be highly beneficial in terms of computational costs, it is solely recommended in case only the general flow field is investigated. Besides the obvious lack of grid resolution near the walls, also the formulation of the standard wall functions causes deviations in the wall normal gradients, as it does not consider all relevant aspects of highly compressible flows. Secondly, numerical convergence and reasonable results for coarse grids using wall functions can only be achieved with the Gamma scheme and coefficients of  $\Gamma \leq 0.5$ . For fine resolved meshes, the higher order van Leer scheme proved to be at least just as stable as the Gamma scheme. Therefore, van Leer's scheme is the recommended choice for wall-resolved simulations and will be used for the following conjugate studies.



---

## Investigation of Thermal Loads onto the Lobed Strut Injector

---

After the validation of the main features, the solver is now applied to investigate the lobed strut injector. This chapter is divided into two major parts: The first half presents a comparison of experimental and numerical data for moderate flow conditions. In the second part, numerical simulations for the injector at hot gas conditions are discussed, which represent a direct match to the flow conditions during combustion experiments at ITLR. The effectiveness of the internal cooling is assessed and the applicability of the newly developed solver to realistic problems is demonstrated. Finally, the results are compared to surface degradation features observed at experimental hardware.

### 6.1 Test Matrix and Numerical Setup

An overview of the investigated flow conditions is given in table 6.1. Experimental data obtained with the modular test channel as introduced in section 3.1.2 is available for moderate flow conditions. During the experiments, the total temperature is varied between 350 K and 500 K in steps of 50 K. Both uncooled and cooled cases are evaluated, where air is used as standard coolant. In addition, the effect of a change to helium as coolant is also investigated for

## 6 Investigation of Thermal Loads onto the Lobed Strut Injector

Table 6.1: Overview of investigated cases for strut injector

		$T_t$	400 K		450 K	500 K		1300 K*
		$p_t$	0.7 MPa		0.7 MPa	0.7 MPa		0.6 MPa
		exp.	exp.	num.	exp.	exp.	num.	num.
Cu	uncooled	X	X	X	X	X	X	X
	Air	X	X	X	X	X	X	X
	Helium	–	X	–	–	X	X	–
	Hydrogen	–	–	–	–	–	–	X
Fe	uncooled	–	–	X	–	–	X	–
	Air	–	–	X	–	–	X	–

\* Simulations are conducted using the model combustion chamber geometry.

selected conditions. It represents hydrogen more closely, which is used for internal cooling during combustion tests. All experiments and simulations correspond to a main flow Mach number of 2.5.

Numerical simulations are only conducted for 400 K and 500 K due to the high numerical costs. In addition, a total temperature of 1300 K is investigated using the combustor geometry instead of the modular channel. This represents the standard test conditions for combustion experiments, and is thus considered a baseline application case for the new solver. For the modular channel, the nozzle design pressure  $p_t = 0.7$  MPa is applied, while for the hot gas conditions only  $p_t = 0.6$  MPa can be realized due to restrictions of the experimental heater system.

Besides the standard strut injector made of copper, also an alternative injector made of stainless steel is considered for the numerical simulations to evaluate the influence of the injector material on the surface temperature. Stainless steel is chosen due to its low thermal conductivity of only 15 W/(m K) compared to 400 W/(m K) for copper. This is expected to lower the influence of the channel wall temperature, as the heat conduction inside the solid is considerably reduced.

In order to minimize computational costs for the conjugate simulations, only the relevant section of the channel containing the strut injector is considered for the parameter studies. The numerical domain for the modular test channel is shown in figure 6.1. The symmetry plane has been blanked for clarity. For the hot gas calculations using the combustor geometry, the numerical setup is adapted to represent a divergent duct with top and bottom wall angles of  $1^\circ$  each. Only half of the channel is modeled by exploiting symmetry with respect to the  $x$ - $z$ -plane.

## 6.1 Test Matrix and Numerical Setup

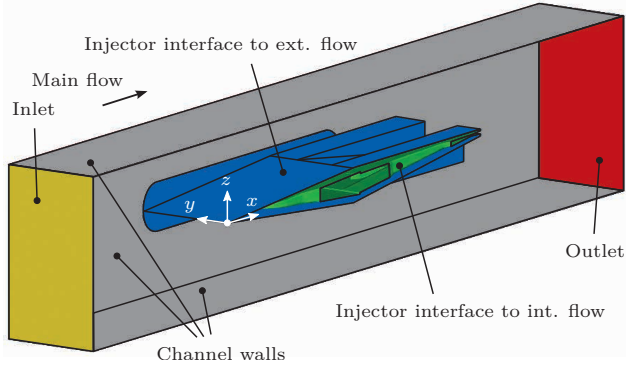


Figure 6.1: Numerical domain

A hybrid mesh is used, as a structured grid would be more difficult without a simplification of the internal coolant flow path. The domain is split into a fluid region, which contains both the main flow and the internal flow path of the strut, and a solid part representing the strut itself. Both regions consist of approximately 11.5 million grid cells, where the comparably high number of cells for the solid region is caused by the complex geometry and the direct interface condition. It requires the cells at the injector surface to be identical to those of the fluid region, as discussed in section 4.2.3. Taking into account the results of the validation cases, a dimensionless wall distance of  $y_1^+ \leq 1$  is ensured for the first cell at every wall.

Accurate inlet conditions for the investigated segment at the relevant total flow temperatures are obtained by conducting a separate simulation for the channel inlet section, which contains the Laval nozzle. Three-dimensional flow profiles are then extracted at a defined interface and imposed onto the segmental simulations as fixed inlet conditions. For the modular channel, this interface is set at  $x = 330$  mm. This corresponds to a position 45.5 mm upstream of the strut leading edge. The segmental domain itself is 180 mm long, thus placing the outlet far enough downstream of the trailing edge to avoid direct interactions. Regarding the combustor geometry, the interface is located at  $x = 380$  mm, i.e. 47 mm upstream of the leading edge. In contrast to the use of a simple block profile as inlet condition, this method allows to correctly capture the boundary layer thickness at the segment inlet.

Exemplary for the resulting inlet conditions, the static temperature distribution at the inlet interface is shown in figure 6.2 for the different investigated main flow

## 6 Investigation of Thermal Loads onto the Lobed Strut Injector

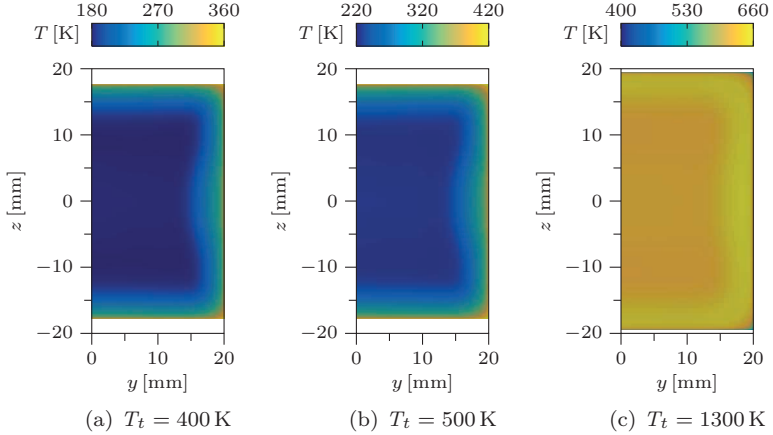


Figure 6.2: Static temperature distribution at the domain inlet for different flow conditions

conditions. Between total temperatures of 400 K and 500 K, only the overall level of static temperature changes. The thermal boundary layer thickness is in the order of a few millimeters, which emphasizes the importance of the separate inlet simulations. At hot gas conditions, the walls are cooler than the flow, which – combined with the supersonic Mach number – results in a local static temperature overshoot near the walls before the central flow temperature is reached. The boundary layer thickness remains in the same order of magnitude for all cases.

Zero gradient conditions are applied at the segment outlet for all variables to account for the remaining part of the channel. The channel walls are considered to be isothermal. For this purpose, an averaged surface temperature along the relevant part of the channel was obtained experimentally and is imposed as boundary condition for the simulations. This results in  $T_w = 360$  K for  $T_t = 400$  K and  $T_w = 420$  K for  $T_t = 500$  K, respectively. For the hot gas simulations using the model combustion chamber geometry, a constant wall temperature of 400 K is applied to represent the water-cooling of the walls during experiments. This corresponds to the standard boundary conditions as already used for the validation in section 5.5.

To distinguish the flow conditions of the internal and external flow fields, the index  $i$  is used to indicate the coolant flow in the present chapter. The coolant is supplied from the side of the injector at a total temperature of  $T_{t,i} = 300$  K.

## 6.2 Moderate Flow Conditions

Table 6.2: Properties of the investigated coolants at  $T = 300$  K [93]

	$\dot{m}$ [g/s]	$c_p$ [J/(kg K)]	$\lambda$ [W/(m K)]	$\dot{m}c_p$ [W/K]
Air	18.03	1006.4	0.0264	18.15
Helium	7.11	5193.2	0.1560	36.92
Hydrogen	4.76	14 313.0	0.1867	68.13

Small Laval nozzles are integrated into the injector ramps, thus the coolant Mach number inside the supply line can be calculated based on the ratio of the supply pipe cross section and the critical cross section of the Laval nozzle. This is not entirely correct, as the flow is not adiabatic due to the heat fluxes at the injector surface. However, the experimentally obtained values for total pressure and total temperature cannot directly be set as numerical boundary conditions for *scramjetFoam*. The combination of a subsonic inflow, the following Laval nozzle, and the variable main flow pressure at the injection ports only allows a stable simulation if the coolant mass flux is specified by means of defining a constant inflow velocity and temperature. The resulting inflow Mach number is 0.252 for diatomic gases such as air and hydrogen and 0.245 for monoatomic gases like helium.

Table 6.2 summarizes the properties of the investigated coolants. It also lists the respective mass flow rates through the injector and the resulting heat capacity rates  $\dot{m}c_p$ , which illustrate the superior cooling capabilities of helium and hydrogen despite the lower mass flow rates. The hydrogen mass flow rate corresponds to a rather high fuel equivalence ratio of approximately 0.5, which is close to the maximum value investigated during combustion experiments at ITLR.

For the simulation of the uncooled injector, the fuel supply port at the side wall is closed. Instead of neglecting the domain inside the injector, which would raise the question of a suitable boundary condition at the inner wall of the strut, the internal fluid region is still included in the simulation. This also corresponds more closely to the experimental setup.

## 6.2 Moderate Flow Conditions

Before investigating the strut at combustor conditions, the experiments conducted for the modular test channel are evaluated and compared to numerical

## 6 Investigation of Thermal Loads onto the Lobed Strut Injector

---

simulations. Besides providing additional validation of the solver, this investigation is also used to identify characteristic phenomena along the injector surface and for a first assessment of the internal flow field.

### 6.2.1 External Channel Flow

The external flow around the strut is discussed first, as the flow features directly influence the heat loads onto the injector. It has been found that the experimental channel operates at the verge of blocking in case the injector is inserted, thus it has to be ensured that the flow field is still supersonic downstream of the strut. Comparability to the combustor flow evaluation, which will be discussed later, would otherwise be lost. For this purpose, experimental schlieren images were obtained. The images corresponding to an external flow total temperature of 500 K are exemplary presented in figure 6.3. The trailing edge of the injector is not located in the field of view of the schlieren system due to geometrical constraints, but it is included on the left side of figures 6.3a and 6.3b to improve clarity. A pronounced oblique shock system is observed, thus indicating a supersonic channel flow. However, a slight asymmetry is found, which indicates the presence of small geometrical irregularities and may cause deviations in the comparison to the numerical results. In case of air injection, increased turbulent effects are clearly visible in the wake of the injector, but the main shock structure remains unchanged.

In addition to the schlieren images, also the static wall pressure distribution along the center line at the top wall is evaluated. Here, the axial coordinate  $x$  is measured from the critical cross section of the Laval nozzle. The numerical data combines both the inlet simulation and the actual segment calculation. As shown in figure 6.4, the numerical simulations are a good match to the experimental data in the inlet section of the channel.

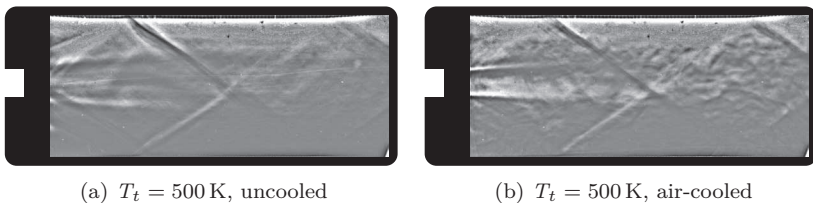


Figure 6.3: Experimental schlieren images of the flow field downstream of the uncooled and the air-cooled injector

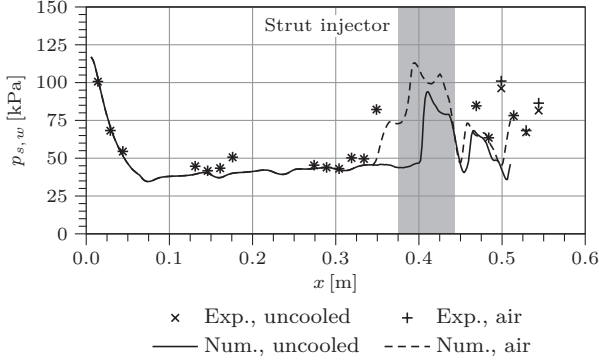


Figure 6.4: Static wall pressure along the top wall,  $T_t = 500$  K

While in experiments the uncooled and the cooled cases only differ slightly in magnitude downstream of the trailing edge, the numerical simulations predict a different behavior. Only the cooled case exhibits a pressure rise upstream of the injector, which is not as pronounced in strength as in the experiments. In case of an uncooled injector, i.e. no fluid injected at the trailing edge, no upstream influence is visible. Both cases converge again downstream of the strut, but still at a lower level than the experimental data. This implies that the coolant injection is sufficient to cause upstream effects inside the channel in the numerical simulation. For a further assessment of the flow field, the numerical data is evaluated in more detail.

Figure 6.5 shows the Mach number distribution along the vertical center plane of the channel and at selected cross-sections perpendicular to the channel main axis. While for the uncooled case a smooth flow field inside the channel is predicted, flow separation occurs at the channel corners as soon as the internal cooling is activated. The separation zone begins upstream of the leading edge and extends up to mid-length of the injector. The onset of the separation bubble causes a pre-injector shock and results in a lower overall level of the flow Mach number, which explains the increased static wall pressure for this case. Based on these findings, it is presumed that the separation bubble is present for all cases in the experiments, probably promoted by small manufacturing and assembly imperfections. For an ideally smooth channel as in the numerical simulations, this effect only appears if coolant is injected.

The same phenomenon is not expected in case of the combustor geometry at hot gas conditions and  $M = 2.5$  due to the divergent duct and the resulting

## 6 Investigation of Thermal Loads onto the Lobed Strut Injector

---

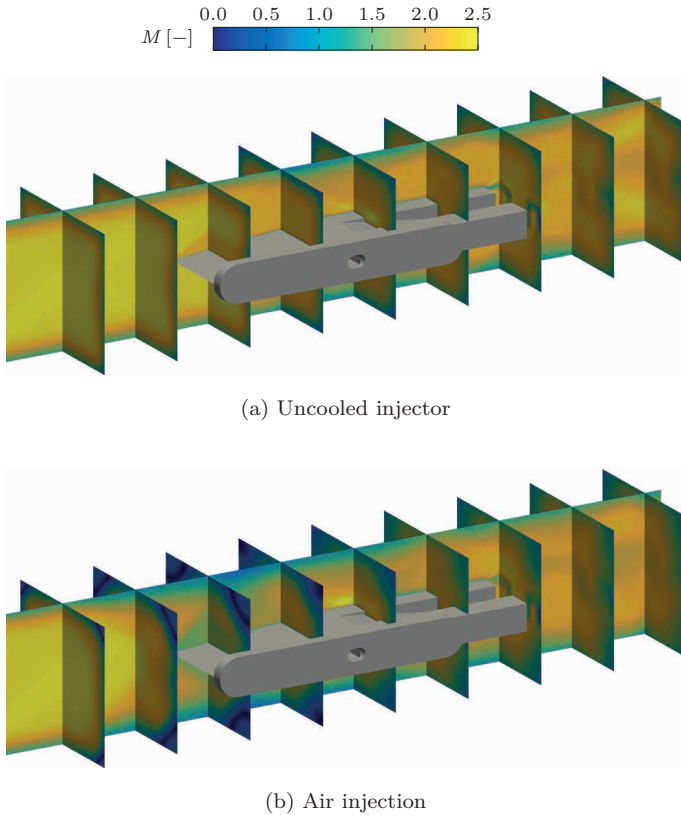


Figure 6.5: Mach number distribution of the external flow,  $T_t = 500$  K

increase in cross section. However, even for the combustor upstream effects have been observed for numerical simulations at lower Mach numbers and higher mass flow rates, as already discussed in section 5.5.2.

To provide further validation, LITA measurements for local Mach numbers and static temperatures were conducted at two axial locations along the channel for a total temperature of 500 K [51], and are compared to the numerically predicted distributions. At each measurement location, a set of points on the vertical center line of the channel was probed. Typically 30 measurements were conducted at each single point and were then averaged.

In addition, also one standard error of the mean, i.e.

$$\sigma_{\text{mean}} = \frac{1}{\sqrt{N}}\sigma \quad (6.1)$$

in case of  $N$  measurements, is shown in figure 6.6 for each data point.

The first data set was obtained 75.5 mm upstream of the injector leading edge. Note that the numerical data for this location is extracted from the separate inlet simulation, as the domain containing the injector section does not extend this far upstream. The second set of measurements was taken 28.5 mm downstream of the trailing edge, which corresponds to  $x = 114.5$  mm. Both air injection through the strut and external flow only were investigated at this location. The results for the flow Mach number and the static temperature profiles are shown in figure 6.6.

For the undisturbed flow at  $x = -75.5$  mm, good agreement between numerical simulation and experimental data is achieved for both Mach number and static temperature. Downstream of the strut, the numerical simulations predict a higher flow Mach number in case no coolant is injected, while the general trend of the profile is still matched. This agrees with the evaluation of the static wall pressure, which is higher for the experiments. As soon as air is injected, the numerically predicted Mach number decreases. As discussed above, this is caused by flow separation occurring at the channel corners and the resulting increase of the leading edge shock strength. Compared to the experiments, however, the average Mach number is still higher. Similar results are obtained when comparing the static temperature data downstream of the strut. For external flow only, the overall level is shifted towards lower temperatures in the numerical simulations.

Activating the internal flow then leads to a decrease of the overall deviation. While the LITA measurements show a local temperature dent caused by the coolant at around  $z = 4$  mm, the numerical prediction does not exhibit a similar phenomenon. As the focus of the simulations is not on the mixing process, but on the injector surface and its surroundings, the wake region of the injector exhibits a comparably low grid resolution. While this is expected to influence the accuracy of the mixing prediction and the coolant jet width, the inverse trend in static temperature is not presumed to be connected to the grid resolution. However, to rule out an influence of the numerical mesh, the grid is locally refined in the wake of the strut. To maintain a reasonable total number of grid cells, the internal injector flow is replaced by an averaged inlet boundary condition at the coolant injection ports. Furthermore, wall functions are employed, as the focus now is on the general flow field. The refined simulation

## 6 Investigation of Thermal Loads onto the Lobed Strut Injector

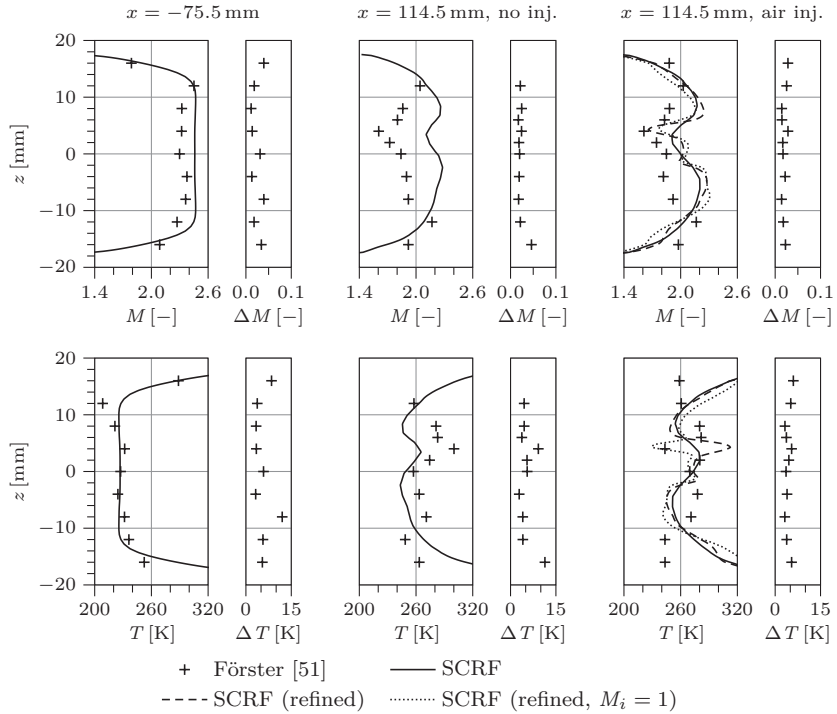


Figure 6.6: Comparison of numerical simulations and LITA measurements upstream and downstream of the strut,  $T_t = 500 \text{ K}$

exhibits a more pronounced local change in static temperature, as can be seen by the dashed line in figure 6.6. However, instead of the experimentally determined decrease, still a temperature increase is predicted.

The reason for this behavior is found to be the coolant injection condition: While the original geometry of the strut features small Laval nozzles at the trailing edge to accelerate the coolant, these nozzles seem to degrade during the experiments. To account for this effect, a sonic inflow condition is imposed at the injection ports for the refined grid. This boundary condition has already been used in previous numerical studies [176], where the internal geometry of the strut was not considered. It results in an increased coolant mass flow, which is injected at lower velocity. The corresponding static temperature distribution

is represented by the dotted line in figure 6.6, and it indeed shows a pronounced local temperature decrease.

Since the actual degradation of the Laval nozzles cannot be quantified exactly, the original geometry will be used for all coupled simulations within the present thesis. However, this finding has to be taken into account for future simulations, especially when combustion is to be considered. Since the fuel mass flow may vary considerably depending on the degree of deformation, this will have a significant influence on the combustion process.

### 6.2.2 Internal Flow Field

Besides the external channel flow, also the characteristics of the internal flow field are relevant for the evaluation of the cooling mechanism. Figure 6.7 shows a representative air flow through the internal flow path for an external flow at  $T_t = 500$  K. Data is extracted at the horizontal center plane of the injector where possible. The inclined flow field inside the ramps is projected onto the same plane. The major internal flow characteristics, such as recirculation zones, are found to be independent of the external flow conditions, only the temperature varies due to the change in induced heat loads.

Two distinct recirculation zones can be identified on account of the Mach number distribution and the stream vectors inside the injector as presented in figure 6.7a. The first one is located directly at the leading edge, and extends towards the side of the strut up to the supply line connection. The flow is not able to fully follow the geometry during the redirection towards the leading edge and the following deflection by  $180^\circ$  towards the trailing edge. The second major recirculation zone appears upstream of the ramps. Due to the high momentum of the coolant, the majority of the fluid is concentrated in the center of the injector before being distributed into the single ramps. This results in a large eddy towards the side of the injector. Both these recirculation zones are in good agreement with the work of Gerlinger and Simson [65, 143], who numerically investigated a similar injector with a slightly simplified internal flow path and a blunt leading edge.

Additional flow features can be observed at the impinging of the internal flow onto the ribs, which are stabilizing the ramps. While at the center ramp the flow impinges directly onto the stabilizer, the flow in the outer ramps impacts onto these ribs under an angle and thus causes further swirls. These features have a direct impact on the total temperature distribution inside the injector, as shown in figure 6.7b. A significant increase in total temperature is observed

## 6 Investigation of Thermal Loads onto the Lobed Strut Injector

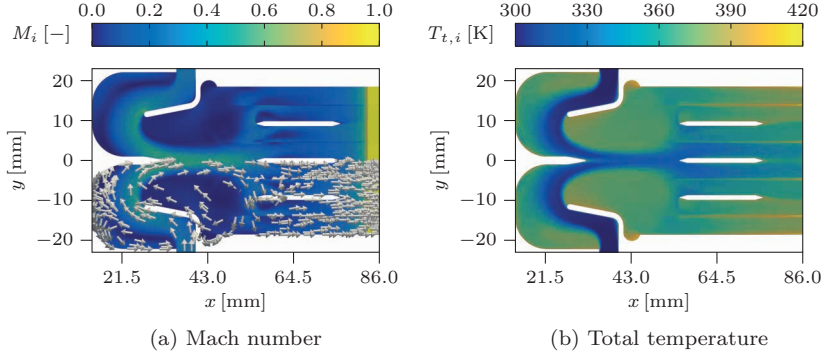


Figure 6.7: Top view of the internal air flow,  $T_t = 500$  K

at the recirculation zones, which is due to the longer local residence time of the flow. This may prove critical at the leading edge, which, at least for hot gas conditions, is suspected to be exposed to the highest heat loads.

The center region of the coolant flow remains comparably cool throughout the whole domain, while especially the flow in the outermost ramps features a considerable increase in total temperature. This is caused by two effects: At the outer ramps the ratio of coolant mass flux to overall wetted surface is decreased due to the smaller width of the ramps. In combination with the isothermal channel walls at  $T_w = 420$  K, this reduces the cooling effect and increases the flow temperature compared to the other ramps. Furthermore, the coolant mass flux is not distributed equally along the injection ports, instead the center ramp exhibits an increased mass flux due to the more direct flow path.

Figure 6.8 shows the area-specific mass flux along the horizontal center lines of the injection ports. The flow conditions correspond to the internal flow field presented above. For the center ramp the specific mass flux is found to be increased by about 15%. Also the wake of the ramp stabilizers is still visible in the profiles of the three middle ramps, which results in an inhomogeneous distribution even along the single injection ports.

### 6.2.3 Injector Surface

After identifying the main features of both the external and internal flow fields, the injector surface is investigated. The influence of the external flow conditions,

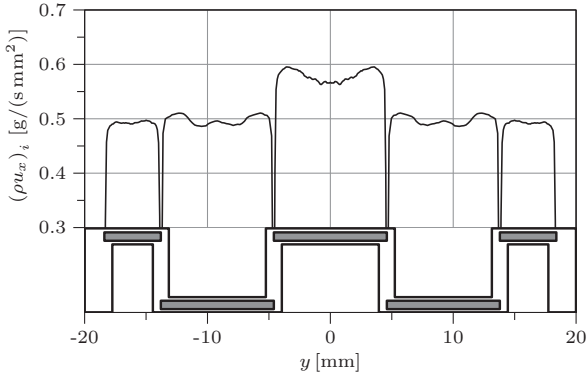


Figure 6.8: Computed area-specific air mass flux along the horizontal center line of the injection ports,  $T_t = 500$  K

the coolant medium and the injector material is assessed using a combination of experimental and numerical data sets. For the present section, the evaluation of the numerical data sets is limited to the bottom surface of the injector to maintain comparability to the experiments. The numerical prediction of the external flow field is additionally taken into account where necessary. A more detailed assessment of the internal flow and the temperature distribution inside the solid body is conducted in section 6.3 for the hot gas conditions.

### Influence of the External Flow Temperature

Firstly, the influence of the external flow total temperature on the injector is evaluated. All results are visualized using the dimensionless surface temperature  $\Theta$  as defined in equation (3.2). Figure 6.9 provides an overview of the experimental data for the copper injector and compares both the uncooled cases and the effect of air as coolant.

A significant influence of the external flow total temperature is observed regarding the uncooled injector, which is presented on the left side of figure 6.9. While a pronounced hot spot at the center of the leading edge is observed for all cases, the general distribution of the dimensionless surface temperature is more homogeneous for lower values of  $T_t$ . When the total temperature of the external flow is increased towards 500 K, the effect of the channel side walls becomes visible: As the channel is not insulated against ambient, the temperature difference between the flow and the channel walls increases, and

## 6 Investigation of Thermal Loads onto the Lobed Strut Injector

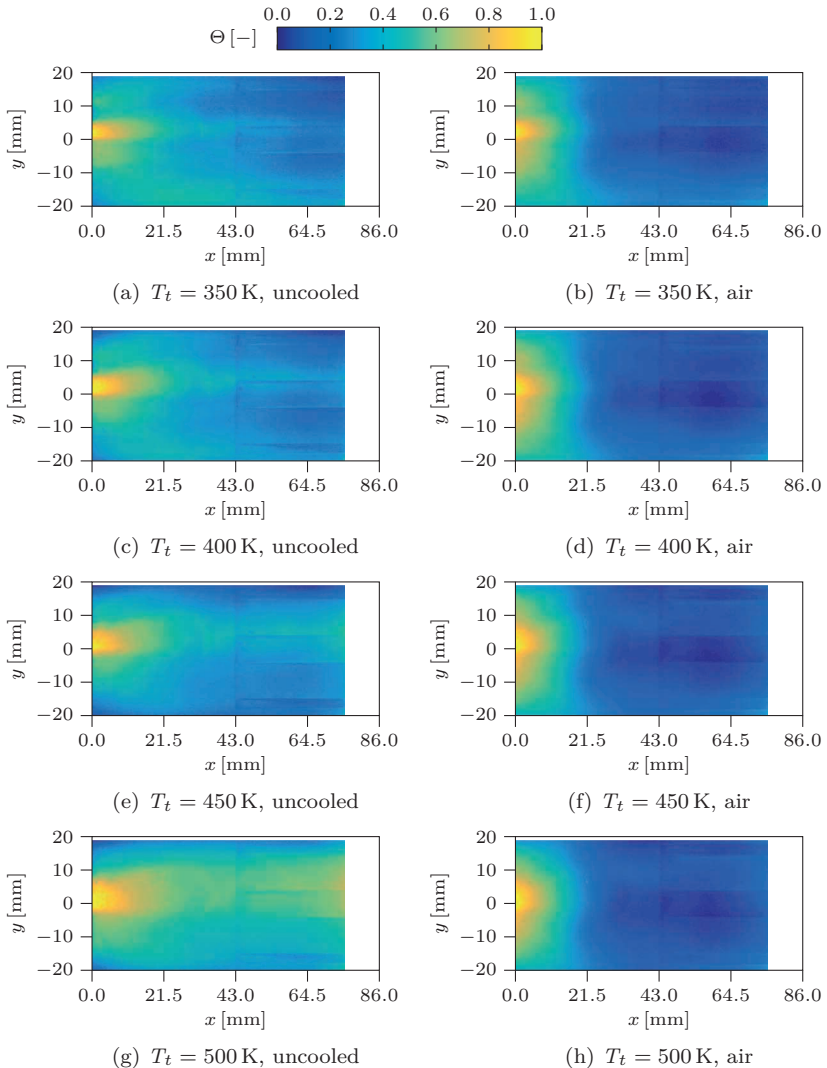


Figure 6.9: Influence of the total flow temperature on the dimensionless surface temperature, experimental data for the uncooled and the air-cooled injector

the walls begin to cool the injector. Thus the center of the injector exhibits a higher dimensionless temperature, which also increases towards the trailing edge. This phenomenon is most pronounced for  $T_t = 500$  K.

When the internal flow path is activated by supplying air as coolant through the injector, the influence of the external flow total temperature is nearly eliminated, as can be seen on the right side of figure 6.9. The leading edge hot spot is still observed for all cooled cases, but a clearly cooler region is detected in the center of the injector between  $x = 50$  mm and  $x = 75$  mm. Taking into account the findings presented in section 6.2.2, this is caused by an increased percentage of coolant passing through the center ramp. In addition, the impingement on the vertical stabilizer of the ramp provides further enhancement of the cooling. However, these features are independent of the surrounding flow conditions, as the location of the hot and cold zones does not vary with temperature.

At external flow total temperatures of 400 K and 500 K, the dimensionless surface temperature obtained during experiments is compared to numerical simulations, as presented in figure 6.10. The figures on the left side repeat the experimental distributions of the dimensionless surface temperature as already introduced in figure 6.9. The corresponding numerical data is provided on the right side.

Qualitative agreement is achieved for the cooled cases. The leading edge hot spot and the enhanced cooling at the center of the strut are correctly predicted by the numerical simulations. The effect of the isothermal boundary condition at the channel walls is also visible, as the sides of the injector exhibit an increased dimensionless temperature. Since the injector is cooled, the walls are at a higher temperature and thus heat the outer injector regions. Regarding the uncooled cases, deviations between experiments and simulations are observed: The hot spot is not present in the numerical data, instead the trailing edge of the injector seems to be the hottest region at the investigated external flow temperatures. Furthermore, the general level of  $\Theta$  along the surface is increased at  $T_t = 400$  K. However, it has to be taken into account that the uncertainty in  $\Theta$  increases with a decreasing maximum temperature difference  $T_{max} - T_{min}$ . As shown in appendix C.1, the uncertainty is approximately twice as large at  $T_t = 400$  K compared to  $T_t = 500$  K. At this higher total flow temperature, the general distribution of the dimensionless temperature approaches the experimental data, where leading and trailing edges exhibit higher values than the lateral parts of the strut.

To further investigate the reason for the presence or absence of the hot spot at the leading edge, more details of the external flow field in this region have to be taken into account. Figure 6.11 shows a numerical composite of the main

## 6 Investigation of Thermal Loads onto the Lobed Strut Injector

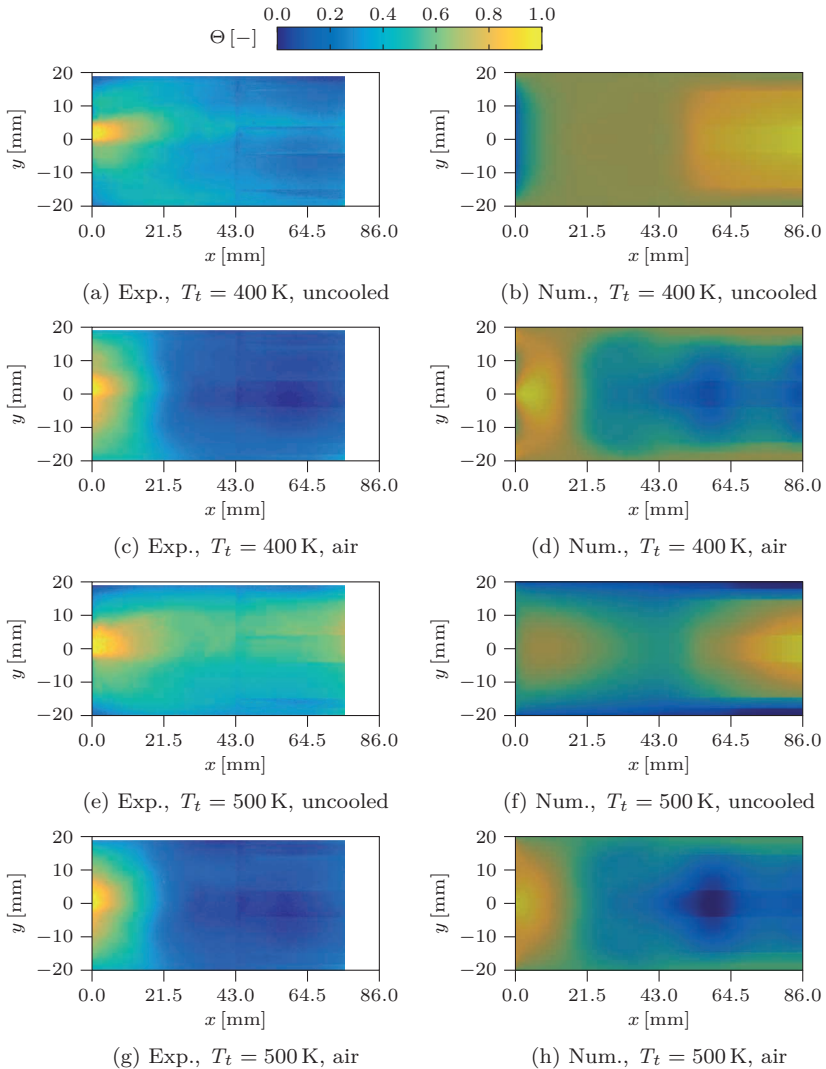


Figure 6.10: Influence of the total flow temperature on the dimensionless surface temperature, comparison of experimental and numerical data

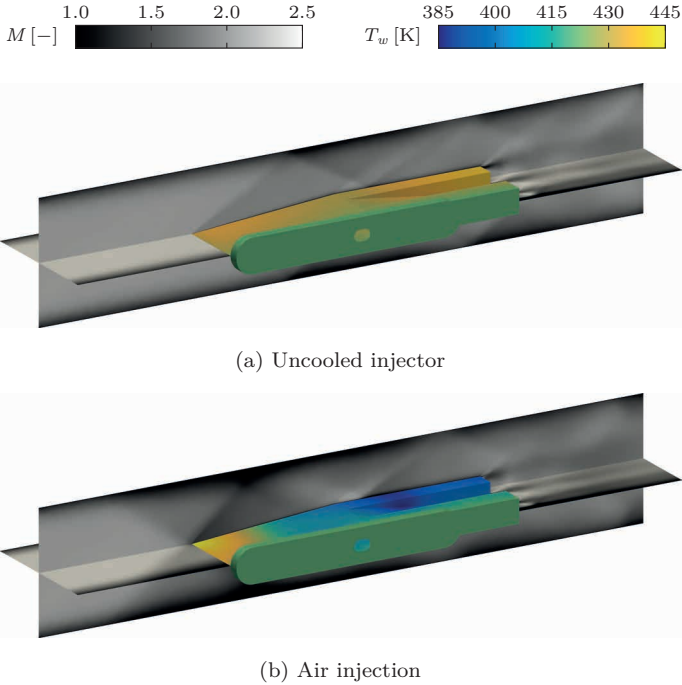


Figure 6.11: Mach number distribution of the external flow and injector surface temperature,  $T_t = 500$  K

flow Mach number in the horizontal and vertical center planes of the channel as well as the surface temperature along the injector.

As discussed above, flow separation occurs for the cooled case. The resulting pre-injector shock leads to an increased leading edge shock strength, and thus a higher leading edge temperature despite of the cooling. Furthermore, a central shock intersection is present directly upstream of the leading edge, which causes the pronounced hot spot. For  $T_t = 400$  K, as shown in figure 6.10d, the shock waves downstream of the intersection are also directly visible at the injector surface, as they result in a higher local temperature in the impact region. While for the cooled cases the maximum surface temperature, i.e. the highest values of  $\Theta$ , occur near the leading edge, the distribution for the uncooled injector is different. Since the leading edge shock is reduced in strength, the impact of the reflected shock at mid-length initiates a second hot zone at the surface.

## 6 Investigation of Thermal Loads onto the Lobed Strut Injector

---

This implies that at these moderate total temperatures the reduction in Mach number and the associated rise in static temperature due to the reflected shock are more significant than the heat loads caused by the leading edge shock itself. However, in the aft region of the strut, cooling mechanisms are more efficient, thus the phenomenon can be observed more clearly for the uncooled injector. In case of internal cooling, only a moderate increase of dimensionless surface temperature is visible between  $x = 65$  mm and  $x = 80$  mm.

### Influence of the Coolant Medium

Until now only air as coolant has been evaluated. However, during combustion experiments the injector is cooled by the fuel, i.e. hydrogen, which exhibits considerably a higher specific heat capacity and heat conductivity. Hydrogen cannot be used during tests at moderate temperatures because of safety precautions. Instead, helium is investigated due to its similar thermophysical properties.

Figure 6.12 presents a comparison of the experimental and numerical results for air- and helium-cooled injectors at  $T_t = 500$  K. While the experimental distribution of  $\Theta$  remains nearly unaltered for a change in coolant medium, the numerical data exhibits changes mainly in the vicinity of the side wall. This is caused by the lower minimum temperature level in case of helium, whereas the walls remain at the same boundary condition, and thus the near-wall parts of the strut are at relatively higher values of  $\Theta$  compared to the air-cooled case. In general, the center region of the strut is still cooled best, and a change in coolant does not improve cooling of the leading edge.

The presumed insufficient effect of the internal cooling mechanism on the leading edge is also supported by the numerical temperature distribution along the bottom surface, which is shown in figure 6.13. The data corresponds to the distributions of  $\Theta$  as presented figures 6.12b and 6.12d. The leading edge temperature is identical for both cases. It is only cooled by heat conduction in the solid fore part of the strut. A major part of the cooling effect in this region seems to be due to the contact area to the channel side walls, as otherwise a change in medium should also imply a change in leading edge temperature. This is expected to be observed even more clearly for the hot gas conditions, which will be discussed later.

In summary, the increased heat exchange capabilities of fluids like helium lead to a generally better cooling of the center region, but do not benefit the leading edge cooling at this moderate total temperature level. However, it has to be kept

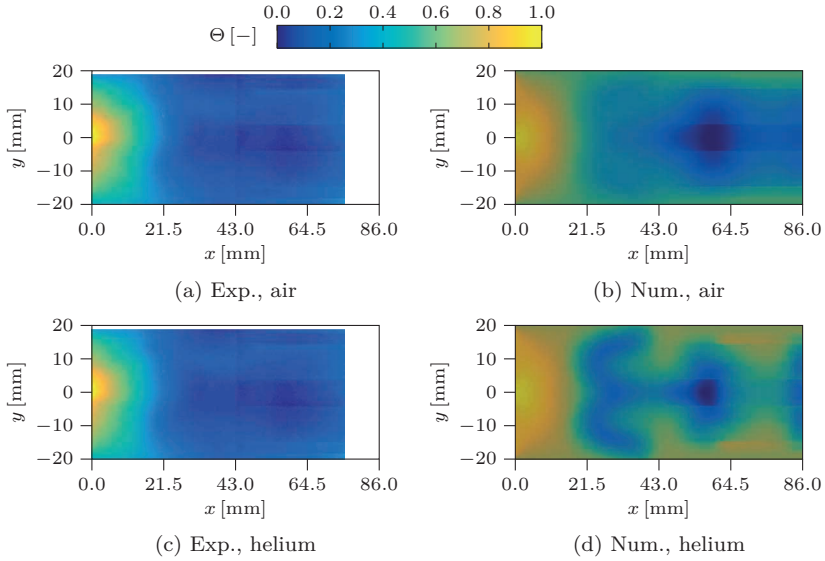


Figure 6.12: Influence of the coolant medium on the dimensionless surface temperature,  $T_t = 500$  K

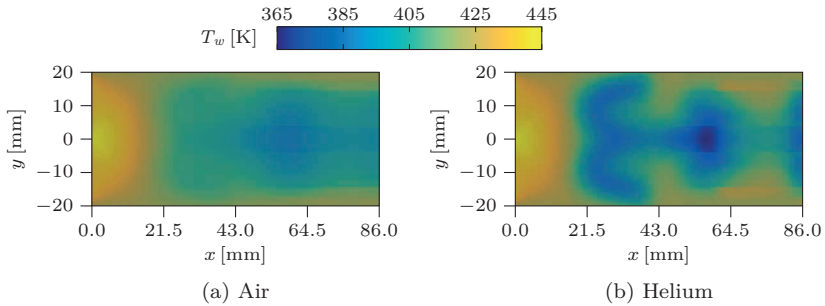


Figure 6.13: Influence of the coolant medium on the numerical surface temperature,  $T_t = 500$  K

in mind that, in case of such light-weight gases, the cooling effect is achieved at an about 60% lower mass flux compared to the one of air for the present cases. This is especially relevant for the application in aerospace, where every additional kilogram of mass implies higher operational costs.

## 6 Investigation of Thermal Loads onto the Lobed Strut Injector

### Influence of the Injector Material

Besides the variation of the coolant medium, also a second injector material with a significantly lower thermal conductivity is investigated numerically. Stainless steel is selected for this purpose. Figure 6.14 presents the comparison of the copper and steel injectors at an external flow total temperature of  $T_t = 500$  K. The corresponding data for  $T_t = 400$  K is shown in appendix C.2, as it is not discussed here.

As expected, the stainless steel injector features a more inhomogeneous dimensionless surface temperature distribution due to the lower thermal conductivity. The hottest part of the injector still is the aft region for the uncooled case, but additional phenomena can be observed. The expansion fan originating a mid-length of the injector causes a slightly cooler region at the surface directly downstream, which is not as sharply delimited in case of the copper strut. Furthermore, the cooling influence of the walls is limited to a smaller part of the injector sides, which leads to a generally increased level of  $\Theta$ .

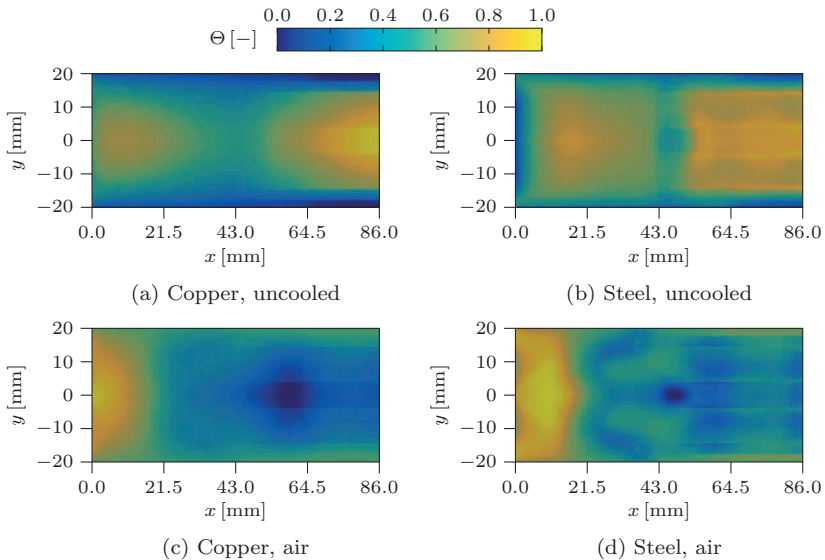


Figure 6.14: Influence of the injector material on the dimensionless surface temperature,  $T_t = 500$  K

If the internal air flow is activated, the flow path and the deflection ribs in the front part of the injector are clearly discernible in the dimensionless surface temperature. Heat conduction from well cooled to poorly cooled areas is considerably reduced compared to copper, also the absolute surface temperature minimum is located further upstream. The coolant is accelerated to supersonic speed directly at the trailing edge and thus exhibits a lower static temperature, which is also reflected on the surface. As previously discussed, the diagonal shock waves traveling across the leading edge are causing a characteristic pattern at the surface. This is even more clearly visible for stainless steel, together with a relatively hotter front region compared to the rest of the strut.

### 6.3 Hot Flow Conditions

After obtaining an impression of the general flow field and the behavior of the injector surface for different coolants and materials, flow conditions representative for the ITLR model combustion chamber are applied. The external flow total temperature is raised to  $T_t = 1300$  K, while the total pressure is lowered to  $p_t = 0.6$  MPa. However, it has to be kept in mind that the actual total temperature at the leading edge of the injector is lower due to the heat losses at the cooled combustor side walls, which are set to  $T_w = 400$  K.

Three cases are investigated in detail: No internal cooling, an internal air flow and the use of hydrogen as coolant. While the internal air flow corresponds to idle conditions during experiments, the hydrogen case represents the cooled injector for actual combustion tests. Similar to the simulations at moderate conditions as discussed above, a separate inlet simulation is conducted to obtain inlet boundary conditions at the combustor segment containing the strut injector.

#### 6.3.1 External Combustor Flow

In contrast to the modular channel, no change in the main flow field is observed for the combustor geometry, as was expected due to the wider cross-section and the resulting lower blockage effect of the strut injector. Figure 6.15 shows the Mach number distribution in the vertical center plane of the combustor. In addition, again selected cross-sections perpendicular to the combustor length axis are presented.

## 6 Investigation of Thermal Loads onto the Lobed Strut Injector

---

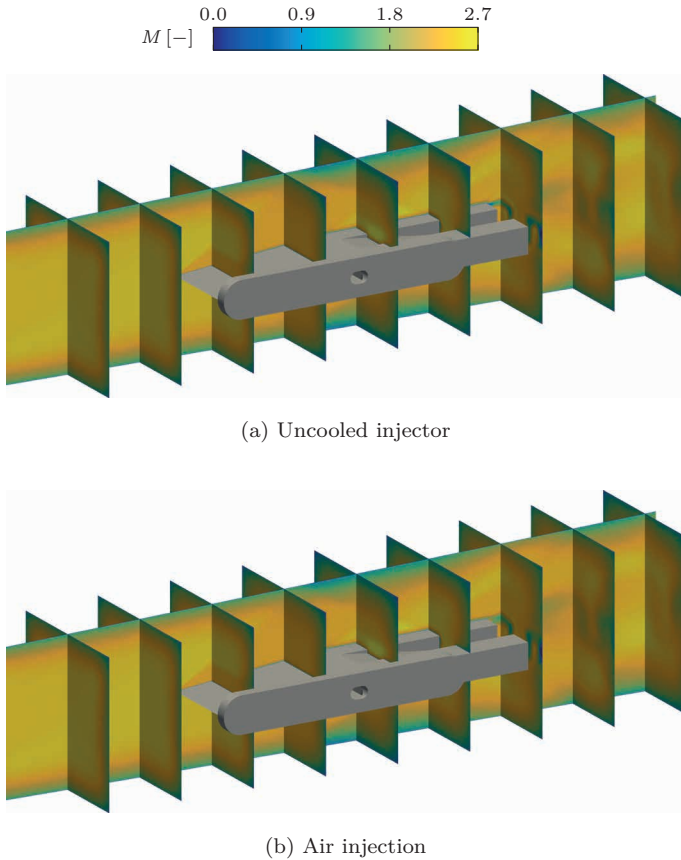


Figure 6.15: Mach number distribution of the external flow,  $T_t = 1300$  K

Without coolant injection, the results are very similar to the corresponding case at  $T_t = 500$  K as presented in figure 6.5. The slightly higher maximum Mach number is caused by the divergent duct and the resulting higher expansion ratio. However, the activation of the internal cooling does not cause any flow separation. Instead, the flow field remains nearly unchanged except for the coolant injection in the wake of the injector.

Besides the increased cross section of the combustion chamber, also the reduction in mass flow due to the higher total temperature leads to a more stable

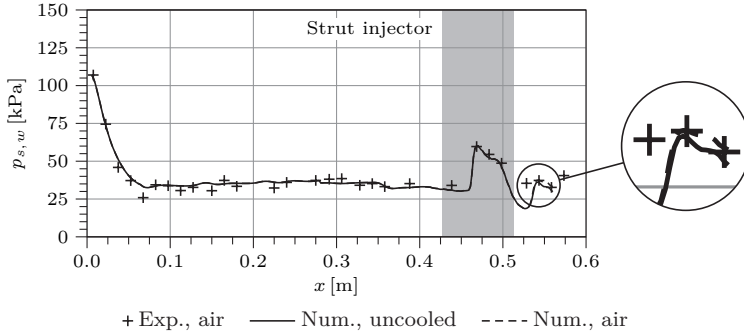


Figure 6.16: Static wall pressure along the top wall,  $T_t = 1300$  K

external flow field. A change in coolant medium does not alter these results, as also for hydrogen no numerically predicted flow separation is observed.

Regarding the static wall pressure distribution as shown in figure 6.16, good agreement between the experimental data and the numerical simulation is obtained. Again the numerical results represent a combined plot of the inlet and the segment simulations. Experimental data is only available for the cooled injector, as the complete deactivation of the cooling at hot gas conditions would damage the strut. The effect of the coolant is reduced to the wake of the injector as shown in the magnified section of figure 6.16. Here, a slight increase in static wall pressure is observed in case the internal flow path is activated. Therefore, the influence of the external flow on the injector is considered to be constant for all investigated hot gas cases.

### 6.3.2 Internal Flow Field

A horizontal cut through the internal flow field along the center plane of the strut is depicted in figure 6.17 for both air (subfigures a and b) and hydrogen (subfigures c and d). Again, the flow inside the ramps is projected onto the center plane. The major recirculation zones remain unchanged compared to the moderate flow conditions shown in figure 6.7. Also the flow characteristics inside the ramps do not change. When using hydrogen instead of air, only the Mach number inside the recirculation zones is slightly increased.

However, differences occur regarding the total temperature inside the injector, as can be seen in figures 6.17b and 6.17d. Compared to the moderate flow

## 6 Investigation of Thermal Loads onto the Lobed Strut Injector

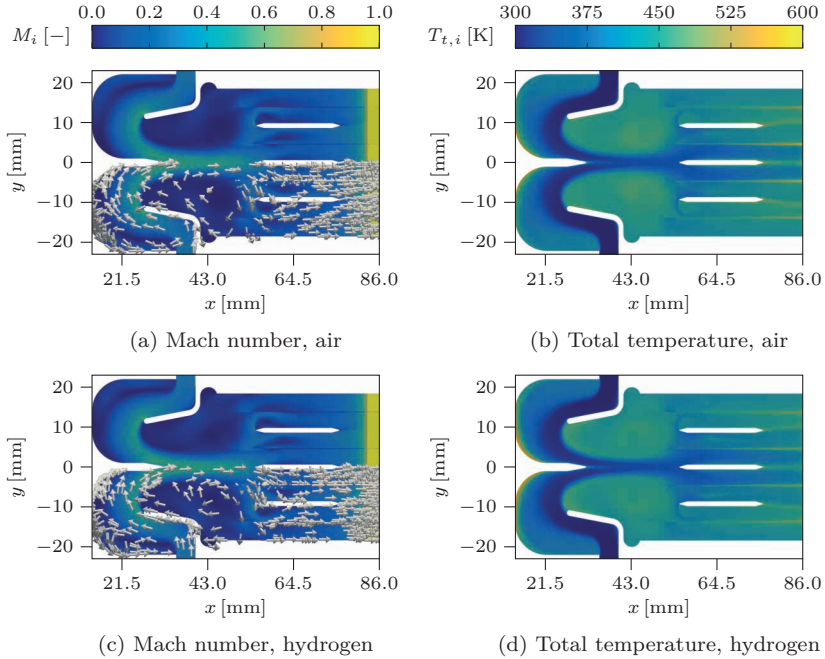


Figure 6.17: Top view of the internal flow field,  $T_t = 1300$  K

conditions, the total temperature level is increased apart from the core flow of the coolant, which corresponds to the increased heat loads generated by the external channel flow. Furthermore, a more homogeneous total temperature is obtained at the outermost ramps due to the cool combustor walls. The total temperature remains higher towards the sides of the other ramps. This is caused by the absence of any internal flow path inside the vertical parts of the trailing edge.

Switching from air to hydrogen slightly decreases the general total temperature level, as due to the considerably higher heat capacity of hydrogen more heat is required to achieve a similar temperature rise as in case of air. This effect is most notably observed in the recirculation zones near the leading edge and in the central region. The coolant flow remains at a comparably low total temperature within the main flow path in the front part of the strut. Towards the curved center of the front region, where the highest heat loads are transferred to the coolant, the total temperature is found to be close to the

local solid body temperature as presented in the following section. More heat can be absorbed here in case of hydrogen, while at the same time the higher heat conductivity leads to a broadening of the hot fluid zone compared to the air-cooled case. The total temperature increases towards the trailing edge, but still remains lower than for the air-cooled injector. This is best observed in the area downstream of the ramp stabilizers, where the hot streaks are reduced for hydrogen.

For all investigated cases, it is found that the total temperature of the internal flow does not rise above 600 K despite the considerably higher external flow temperature. At the trailing edge of the injector, the coolant only exhibits an average total temperature of around 500 K in the outer ramps and even less in the center of the strut. This has to be taken into account for future combustion simulations, as the initial total temperature of the fuel is an important aspect, for example for the correct determination of the ignition delay.

### 6.3.3 Injector Surface and Body

Before the temperature distribution inside the solid part of the injector is evaluated, first the injector surface is discussed in detail. A overview of both the top and bottom surface temperature is presented in figure 6.18 for all investigated hot gas cases. Besides the parabolic temperature at the leading edge caused by the cool walls, also the second hot zone at the trailing edge is present, which was already identified for the moderate flow conditions. It still coincides with the impact of the reflected leading edge shock and the corresponding increase in temperature and the thickening of the boundary layer. This is shown in figure 6.19 for the uncooled injector.

As expected, the activation of the internal air flow does not significantly reduce the leading edge temperature. This can be seen in the comparison of figures 6.18a and 6.18b to 6.18c and 6.18d. Instead, the central region and the trailing edge exhibit a more pronounced decrease in temperature. However, the center region of the trailing edge still remains approximately 150 K hotter compared to the more upstream part of the injector surface regardless of the internal cooling. Figures 6.18e and 6.18f show that the overall surface temperature, except for the immediate surroundings of the leading edge, can be further decreased by using hydrogen as coolant. A more inhomogeneous temperature is obtained in the center of the strut, with distinct cool areas in the surroundings of the sideways fuel supply ports around  $x = 35$  mm. The trailing edge can be cooled more efficiently due to the lower coolant total temperature, as presented above in figure 6.17d. However, it still exhibits a

## 6 Investigation of Thermal Loads onto the Lobed Strut Injector

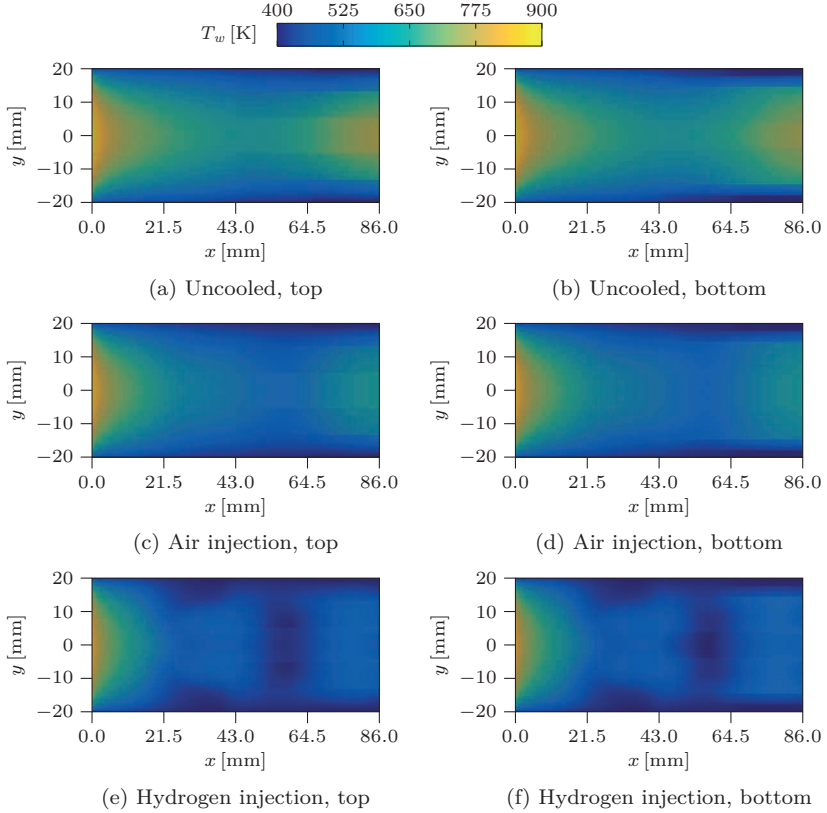


Figure 6.18: Injector surface temperature,  $T_t = 1300$  K

rise in temperature compared to the region more upstream around  $x = 55$  mm, which coincides with the location of the ramp stabilizers. As already observed for the moderate flow conditions, the impinging of the coolant leads to a local increase in heat transfer, which is more pronounced for hydrogen due to its thermophysical properties. The difference between the top and bottom sides of the injector is negligible for all evaluated conditions, thus only the top surface will be taken into account in the following discussions.

Selected lines along the top surface of the injector are considered for a more detailed evaluation. As illustrated in figure 6.20, three lines in  $x$ -direction are investigated. These correspond to the middle of the central ramp ( $y_1 = 0$  mm),

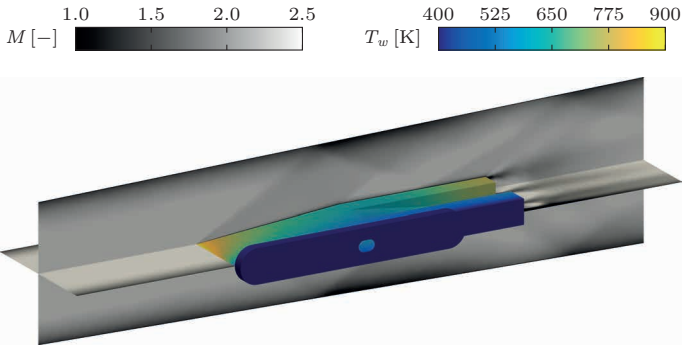


Figure 6.19: Mach number distribution of the external flow and injector surface temperature, uncooled injector,  $T_t = 1300$  K

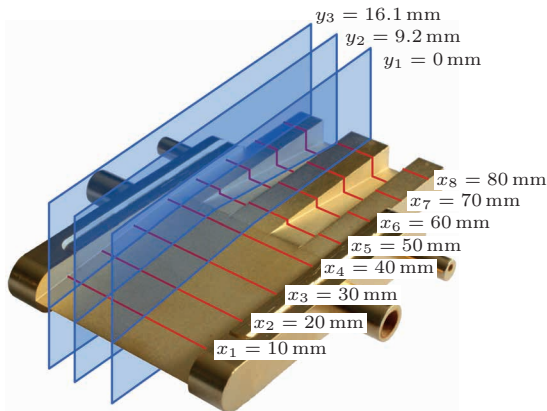


Figure 6.20: Evaluation positions along the injector surface

of the second ramp ( $y_2 = 9.2$  mm) and of the outermost ramp ( $y_3 = 16.1$  mm). Slices at these positions will also be used for the later analysis of the temperature distribution inside the solid body. In addition, also eight equidistant lines perpendicular to the main flow between  $x_1 = 10$  mm and  $x_8 = 80$  mm are investigated. It has to be noted that a comparison of the data between the different locations is difficult for the ramped aft of the strut due to the increasing difference in ramp height and the resulting vertical step size along the investigated line. However, the influence of the internal cooling can still be assessed along each line.

## 6 Investigation of Thermal Loads onto the Lobed Strut Injector

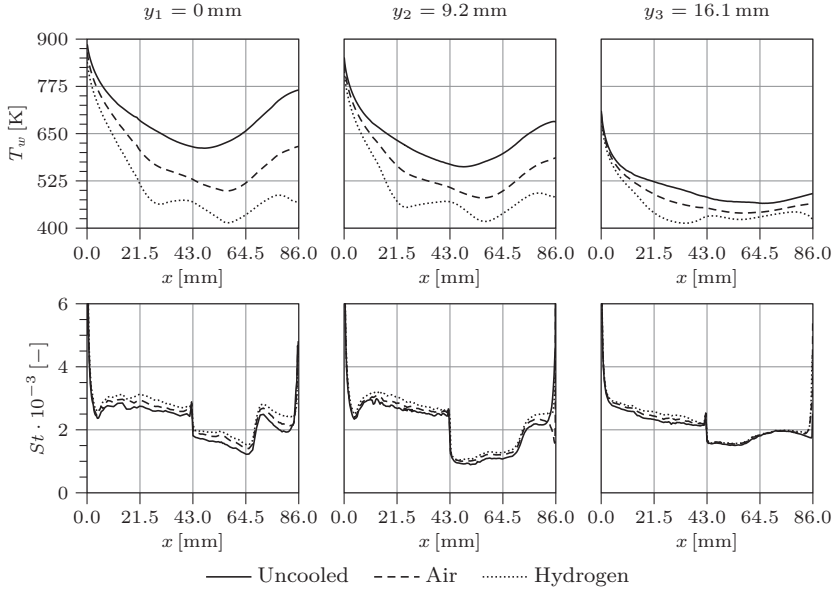


Figure 6.21: Temperature and Stanton number distribution at the injector top surface in  $x$ -direction,  $T_t = 1300$  K

At the selected locations, also the Stanton number distribution is obtained in addition to the surface temperature. The required reference values for velocity and density are taken from the external flow at  $M = 2.5$  to represent the incident flow at the injector. The total flow temperature of 1300 K is used as reference temperature due to the reasons discussed in section 2.2.

As shown in figure 6.21, the evaluation along the ramp centers confirms what has been already shown in the contour plots above. The decrease in surface temperature is most pronounced at the middle ramp of the injector, while towards the isothermal side walls lateral heat conduction is responsible for a major part of the cooling. Thus even for the uncooled case an uncritical temperature level is observed at the outermost ramp. This is backed by the Stanton number, where no effect of the internal cooling on the downstream half of the strut is found for  $y_3$ , although the internal flow path is located close to the side wall. The influence of the ramp stabilizers is visible around  $x = 55$  mm for  $y_1$  and  $y_2$ . Furthermore, switching from air to hydrogen intensifies a secondary minimum in surface temperature at around  $x = 25$  mm, which is found to be

very weak in case of air. The location coincides with the tip of the internal deflection rib and the redirection of the coolant towards the trailing edge. As already indicated in the discussion of the contour plots, a more efficient cooling at the trailing edge is achieved with hydrogen.

Considering the Stanton number distribution, an asymptotic behavior is found at the leading and trailing edges. This is caused by the sharp angles in the geometry and the resulting difficulties in obtaining an accurate numerical heat flux. While the general trend at these locations is supposed to be correct, actual quantities cannot be considered here. The Stanton number shows a decreasing trend for the middle part of the strut towards the aft region, before the impact of the reflected leading edge shock results in a local increase in heat flux at around  $x = 70$  mm. The cut of the inverse ramp at  $y_2 = 9.2$  mm exhibits a different behavior. Here the onset of the Stanton number increase is shifted upstream and coincides with the beginning of the ramp, as the additional boundary layers in the cavity thicken towards the trailing edge. For activated internal cooling, a maximum Stanton number increase of approximately ten percent is obtained at the middle ramp, with a decreasing tendency towards the side walls. Hydrogen causes a minor increase, but does not alter the general trend.

The extraction of data perpendicular to the main flow direction, as depicted in figure 6.22 for the fore half of the injector, shows the characteristic parabolic temperature profile near the leading edge. However, even for the uncooled strut the surface temperature is reduced by 100 K towards mid-length of the injector by heat conduction only. The profile shape is maintained for air injection, but at a lower temperature level. No internal cooling path is present at  $x_1 = 10$  mm, thus a reduced cooling effect and a comparably high maximum temperature are observed. This changes for the positions downstream, where a considerable decrease in temperature is obtained.

Besides resulting in a further decrease in maximum temperature at  $x_1$ , the use of hydrogen leads to a change in profile shape at the positions where internal cooling is directly applied. A plateau in surface temperature can be identified near mid-length of the injector, which does not change any more between  $x_3 = 30$  mm and  $x_4 = 40$  mm. Regarding the Stanton number, a similar behavior as for the streamwise evaluation presented in figure 6.21 is observed for the lines perpendicular to the flow. The level decreases towards mid-length of the strut and towards the side walls. The internal cooling mechanism only leads to a slight increase in Stanton number, which is more pronounced for hydrogen.

The profiles for the aft half of the injector are shown in figure 6.23, where the steps in the profiles are caused by the vertical edges of the ramps. The

## 6 Investigation of Thermal Loads onto the Lobed Strut Injector

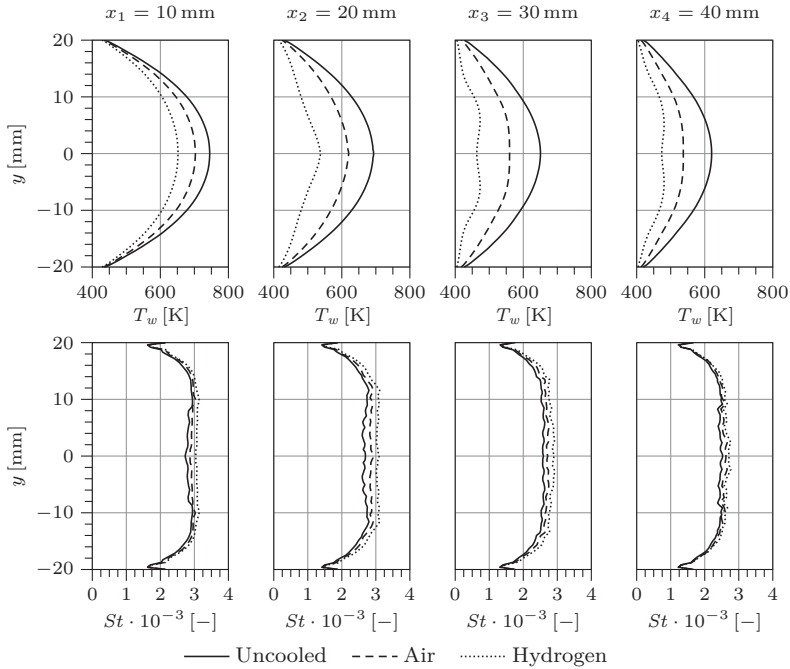


Figure 6.22: Temperature and Stanton number distribution at the injector top surface (upstream half) in  $y$ -direction,  $T_t = 1300$  K

cooling effect is most pronounced towards the trailing edge of the center ramp, where a temperature decrease of almost 300 K can be achieved by hydrogen cooling, compared to approximately 150 K for air. The Stanton number distributions exhibit a lower level for the inverse ramps between  $x_5$  and  $x_7$ . A more homogeneous level is developed towards  $x_8$ , which is located downstream of the shock impact onto the surface. Also a more pronounced increase in Stanton number due to the cooling is observed in this region, which is caused by the higher temperature differences and local heat fluxes for the cooled cases.

Lastly, the temperature distribution inside the solid body of the injector is evaluated. As mentioned above, again three streamwise slices at  $y_1 = 0$  mm,  $y_2 = 9.2$  mm and  $y_3 = 16.1$  mm are investigated. For deactivated cooling, as presented in figure 6.24a, the leading and trailing edges exhibit the highest

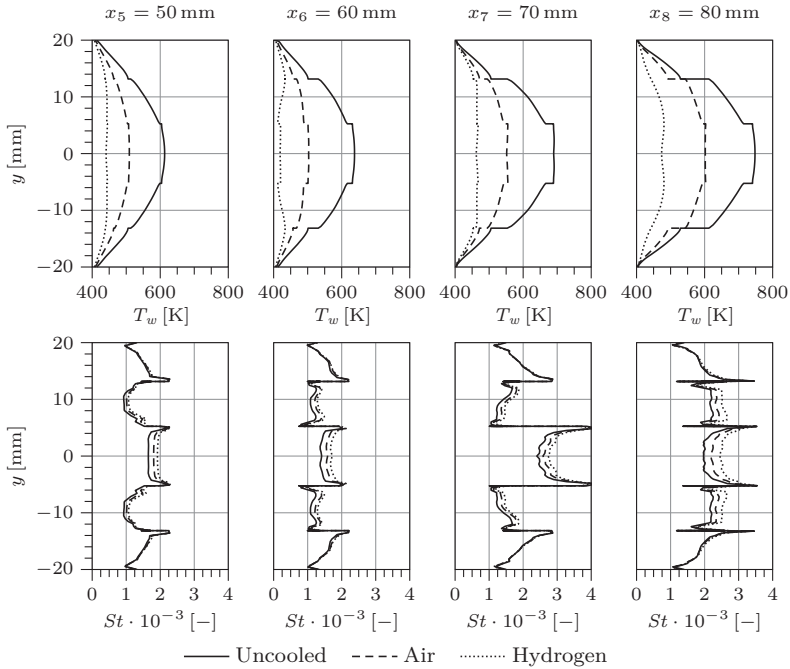


Figure 6.23: Temperature and Stanton number distribution at the injector top surface (downstream half) in  $y$ -direction,  $T_t = 1300$  K

temperature over the whole height of the strut for the first two slices. Towards mid-length, the temperature level decreases with increasing material thickness, as the effect of lateral heat conduction towards the cool side walls becomes more pronounced. This is further supported by the significant drop in temperature towards the outermost ramp at  $y_3 = 16.1$  mm, where a quite uniform and low level is found.

As shown in figure 6.24b, air cooling leads to an overall temperature reduction apart from the immediate vicinity of the leading edge, which is not affected. The ramp stabilizers are among the best cooled areas, as already suspected in the previous discussion. They are directly exposed to the coolant flow and thus feature the lowest temperature, which then leads to an efficient cooling of the aft part. This phenomenon is even more pronounced for hydrogen, as can be seen in figure 6.24c.

## 6 Investigation of Thermal Loads onto the Lobed Strut Injector

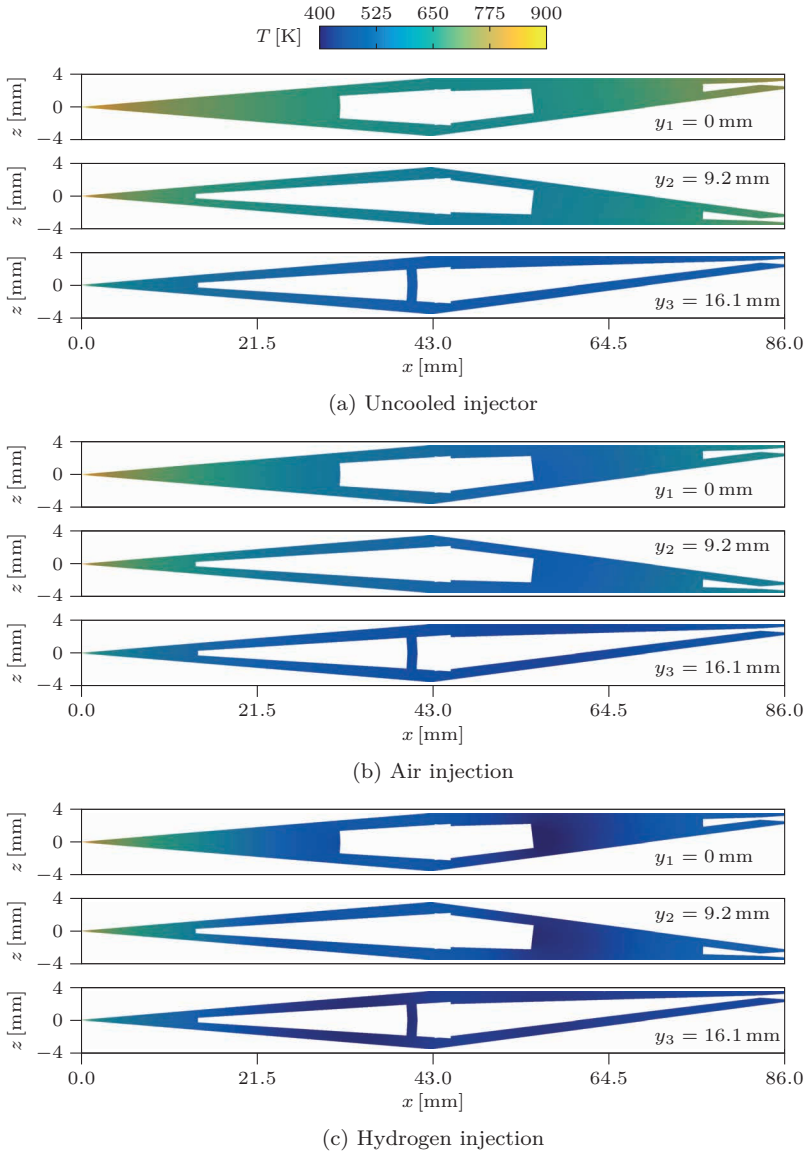


Figure 6.24: Injector temperature,  $T_t = 1300$  K

Table 6.3: Heat flux balance at the strut,  $T_t = 1300$  K ( $\dot{Q}$ : Heat flux across the external strut surface,  $\dot{Q}_i$ : Heat flux across the internal strut surface,  $\dot{Q}_{uc}$ : Heat flux across the external strut surface for the uncooled case)

	Uncooled	Air	Hydrogen
$\dot{Q}_i/\dot{Q}$	1 %	36 %	64 %
$\dot{Q}/\dot{Q}_{uc}$	100 %	112 %	124 %

To assess the effect of the combustor side walls, the ratios of the heat fluxes across the external and internal injector surfaces are listed in table 6.3. Even for the uncooled injector, a small heat flux is transferred to the internal, quiescent fluid. The comparison of air and hydrogen exhibits a significant change in the distribution of the heat fluxes. While for air only about one-third of the heat flux is absorbed by the coolant, this is increased to approximately two-thirds in case of hydrogen. At the same time, the external heat flux increases due to the higher temperature difference between injector and external flow. However, as shown in section 6.3.2, the total temperature level still remains lower for hydrogen than for air, which illustrates the superior cooling capabilities of hydrogen caused by the considerably higher heat capacity rate.

While the cooled combustor walls are essential for long-duration experiments, they do not represent actual flight conditions, where a significantly higher wall temperature is expected. A simulation with adiabatic combustor walls, which represent the worst possible case, would be desirable to estimate the impact of the absence of wall cooling effects on the strut surface temperature. However, due to the geometry of the numerical domain, this is not feasible. The mount of the strut injector is not in contact with the hot combustor flow, and would thus not exhibit a realistic wall temperature. For this reason, a concluding simulation with a constant wall temperature of  $T_w = 1200$  K is conducted. Based on preliminary simulations, this is expected to be close to the adiabatic wall temperature for the investigated main flow conditions.

Figure 6.25 shows the top surface temperature of the hydrogen-cooled injector and the total temperature inside the strut in comparison to the results of the standard case with  $T_w = 400$  K, which corresponds to figures 6.18e and 6.17d, respectively. While the general shock structure of the channel flow is not affected by the change in wall temperature, the injector surface features a considerably different temperature distribution for  $T_w = 1200$  K. Here, a major part of the heat flux onto the strut is due to the combustor side walls. Besides the generally higher temperature level, the parabolic temperature profile at the leading edge is now inverted and the hottest parts of the surface are located

## 6 Investigation of Thermal Loads onto the Lobed Strut Injector

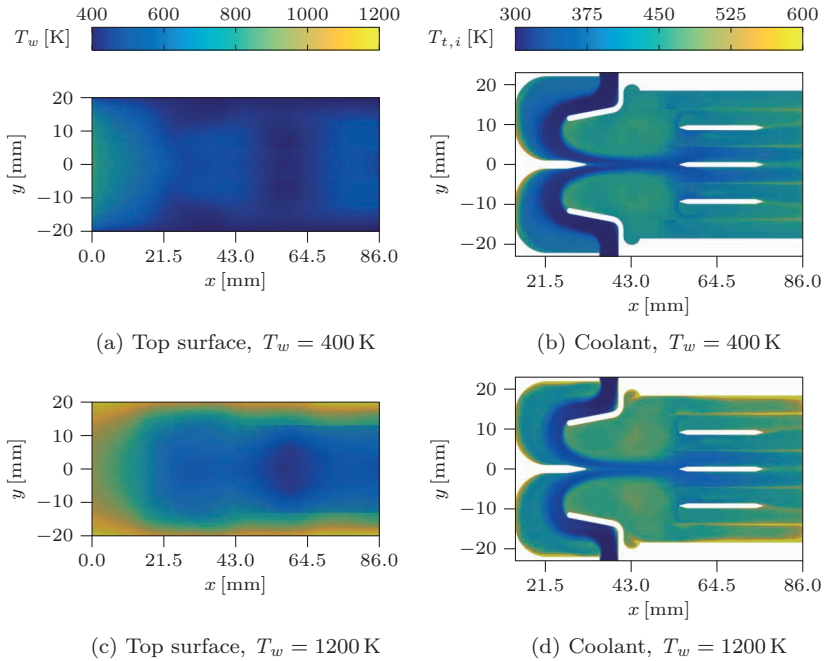


Figure 6.25: Hydrogen-cooled strut at different combustor wall temperatures,  $T_t = 1300$  K

in the lateral regions. The center part of the leading edge can still be cooled by heat conduction towards the internal flow path. It exhibits an about 150 K higher temperature compared to the prediction for the cold side walls. The characteristic cold spot at the center of the strut, which coincides with the tips of the ramp stabilizers, is again present. The lower coolant mass flow rate inside the outer ramps leads to a raised surface temperature in this region, while the three central ramps are comparably well cooled.

The overall coolant total temperature is also increased compared to the corresponding data at  $T_w = 400$  K, which is due to the higher heat flux absorbed by the coolant. This is most pronounced near the leading edge, where the heat conduction inside the solid body contributes a significant part of the cooling effect in case of cool combustor side walls. At  $T_w = 1200$  K, the side walls cause a heat flux towards the strut instead of absorbing energy, which leads to a significant reduction of the cool core flow region inside the upstream half of

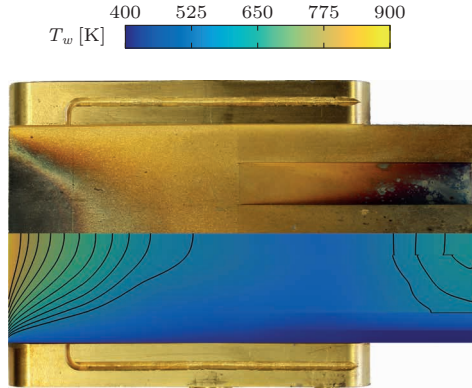


Figure 6.26: Composite of the numerical surface temperature and an injector used during combustion experiments

the injector. Furthermore, the increased temperature of the outermost ramps is directly reflected in the coolant total temperature. The combination of the hot side walls and the reduced coolant mass flow rate in these two ramps causes an increase in total temperature towards the side of the strut. Also the vertical sections between the ramps, which are not in direct contact with the coolant and exhibit a higher temperature, induce distinct hot streaks towards the trailing edge of the strut.

No direct experimental data for the strut surface temperature at hot gas conditions is available. However, the injector exhibits a characteristic surface degradation after several experiments. This has already been shown in figure 1.8c, where the strut was originally introduced. While these degradations do not allow for a quantitative validation of the numerical simulation, they still enable a qualitative verification of the main findings of the present chapter. Figure 6.26 presents a composite of the experimentally damaged injector in the top half and the numerically predicted surface temperature for the air-cooled strut at  $T_w = 400$  K in the bottom half. Internal air cooling is chosen for the comparison, as it represents the idle and thus most common conditions during a typical experimental test day. Temperature contours are included in steps of 25 K.

At the leading edge, the surface degradation exhibits the same parabolic profile as the numerical temperature distribution. The discoloring can be attributed completely to the external channel flow, as no combustion is present in this

## 6 Investigation of Thermal Loads onto the Lobed Strut Injector

---

region of the duct. The size of the parabola and also the undamaged spots near the water-cooled side walls are matched well by the numerical prediction. The trailing edge also exhibits distinct damages to the surface coating, especially inside the inverted ramps. While the degradation inside the ramps is probably due to chemically reacting recirculation zones during combustion experiments, a change in color is also found at the top of the other ramps, where combustion is less likely to occur. Furthermore, these damages also coincide with the numerically predicted rise in temperature due to the reflected shock impact, which is an additional indication that both the external flow characteristics and the surface temperature are correctly captured by *scramjetFoam*.

### 6.4 Summary

Summing up the findings of the present chapter, it can be stated that *scramjetFoam* is able to predict the behavior of the strut injector for both moderate flow temperatures and more realistic hot gas conditions. Existing deviations to experimental data in case of the moderate conditions can be attributed to a non-ideal external flow field, which is caused by geometric irregularities during the experiments. The effects of the internal cooling mechanism can be simulated using the new solver. However, it is also found that a considerable part of the cooling is caused by lateral heat conduction instead of the internal flow path. This is a feature of the experimental setup only, as during flight conditions the combustor side walls are expected to exhibit a significantly higher temperature. A simulation with increased combustor wall temperature proves that parts of the leading edge can be cooled by hydrogen. At these conditions, the lateral regions of the strut are the most highly loaded areas.

The numerical simulations of these realistic applications have proven the ability of *scramjetFoam* to deal with conjugate heat transfer in supersonic flows. Especially in combination with its capability to account for combustion processes, the solver is a well-suited tool for the numerical investigation of scramjet engines.

## CHAPTER 7

---

### Conclusion and Outlook

---

Within the frame of the present thesis, a solver for the coupled numerical investigation of heat transfer phenomena in supersonic flows was developed. The solver was embedded into the open-source CFD environment OpenFOAM, which offers completely code modifiability and enables high parallelization without licensing costs. Together with the included support of chemical reactions, which was the main topic of a cooperating PhD thesis conducted at the Chair of Thermodynamics at the Technical University of Munich, the new numerical solver *scramjetFoam* is able to cover all flow phenomena relevant for the investigation of a scramjet combustion chamber. To demonstrate its suitability, *scramjetFoam* was applied to investigate an internally cooled lobed strut injector, which was exposed to a supersonic hot gas flow.

Based on an existing density-based OpenFOAM solver for transient supersonic flows, *scramjetFoam* was designed to deal with supersonic, chemically reacting engine flows including the conjugate simulation of heat transfer onto the solid structure of the engine. For this purpose, the support of multi-region simulations was included into the solver. It allows the coupling of the fluid region with an arbitrary number of solid regions. A fully transient approach was considered unnecessarily cost-intensive due to the highly different time scales, which are needed to reach convergence of the fluid region and to obtain

## 7 Conclusion and Outlook

---

thermal equilibrium for the solid bodies. Therefore, a local time-stepping technique was implemented, which allows for quasi-steady-state simulations of the flow. These can then be coupled with a steady-state approach for the solid bodies, which could be shown to drastically reduce the required resources.

Before being applied to its actual design purpose, *scramjetFoam* was first validated for a range of test cases available from either literature or preceding studies at ITLR. These cases were selected to provide a thorough validation of major flow phenomena, such as shock waves, expansion fans and boundary layers as well as their interaction. Furthermore, also the validation of a supersonic channel flow representing a realistic model combustion chamber, including fuel injectors protruding into the flow, was conducted. A good performance of *scramjetFoam* for these validation cases could be demonstrated. In addition, also a variety of numerical settings was evaluated, including different wall-functions. This led to the conclusion that the use of the standard wall functions available in OpenFOAM cannot be recommended if the correct numerical prediction of the thermal boundary layer is relevant for the study in question. A fine grid resolution perpendicular to walls delivered good results. A further evaluation of numerical schemes and the influence of the turbulent Prandtl number on the result accuracy allowed for the determination of a well-suited numerical setup, which was then used for further simulations.

Since suitable validation cases for supersonic heat transfer were found to be scarce, additional experiments were conducted at the supersonic test facility at ITLR. The surface of the lobed strut injector was investigated at moderate flow temperatures up to  $T_t = 500$  K using infrared thermography. Although no actual surface temperatures could be obtained due to the impracticality of an in-situ calibration, characteristic cold and hot spots could still be identified by non-dimensionalizing the measured data. Besides air, also the effect of helium as coolant was evaluated due to its closer thermophysical resemblance to hydrogen, which would be used as fuel for a realistic engine. The experimental results were then compared to numerical simulations. Despite deviations regarding flow separation inside the channel, these simulations qualitatively confirmed the experimental findings of distinctive hot and cold zones along the strut surface. Furthermore, it could be demonstrated that the use of helium provides a comparable cooling effect to air at a considerably lower coolant mass flux.

Finally, *scramjetFoam* was applied to the injector at hot gas conditions, which represents an actual combustion experiment at ITLR. Simulations were conducted for both air and hydrogen cooling. Independently of the coolant medium, two major recirculation zones were found for the internal flow path, which had also been observed in comparable form at moderate flow conditions. These

---

zones exhibit an increase in coolant total temperature, and thus lead to a local decrease of cooling effectivity. However, an impinging effect was found to occur at the ramp stabilizers in the rear part of the strut, which considerably enhances the cooling effect in this region. Subsequently, the injector surface temperature was evaluated. Besides the expected identification of the leading edge as thermally most loaded part of the strut, also the trailing edge exhibited a significantly elevated surface temperature compared to the central region of the injector. It could be shown that the reason for this phenomenon is the impact of the reflected leading edge shock onto the injector surface. Air cooling reduced the overall surface temperature level with exception of the immediate surroundings of the leading edge. A further reduction could be achieved using hydrogen as coolant, but the actual leading edge temperature was only slightly affected. For both coolants, the cooled combustor walls were found to absorb a considerable part of the thermal loads onto the injector by means of heat conduction, ranging from one-third for hydrogen to even two-thirds in case of air. Changing to a more realistic and higher combustor wall temperature led to a change in the temperature distribution on the strut surface. While the leading edge could still be partially cooled by the internal hydrogen flow, the lateral regions of the strut were found to exhibit the highest temperature due to a major part of the heat flux being supplied by the side walls.

Thus the main goals of this thesis could be achieved. The functionality of the newly developed *scramjetFoam* solver was successfully demonstrated. Its capabilities regarding the coupled numerical simulation of supersonic heat transfer were proven using the example of the lobed strut injector. The internal cooling mechanism was assessed, which led to the attribution of a major percentage of the cooling effect to heat conduction instead of convection. The coupled numerical approach also offers the possibility to replace the estimated values of injector temperature and fuel injection conditions, which have been used during previous studies, as numerical boundary conditions. This would provide a closer approximation of reality even by simulations which only consider the external combustor flow. Future prospects might include the evaluation of a wider variety of coolant conditions to provide a more complete data matrix. Based on these results, a further optimization of the internal flow path could be considered to eliminate recirculation zones as far as possible and to enhance the overall cooling efficiency. Finally, coupled numerical simulations of the full combustor including chemical reactions would be desirable for a complete analysis of the combustion chamber. Although these simulations would, of course, imply enormous computational costs, they would also further demonstrate the benefits of a highly parallelizable code for the present application.



---

## Bibliography

---

- [1] Anderson Jr., J. D.: Hypersonic and High Temperature Gas Dynamics. McGraw Hill, Inc., 1989. ISBN: 978-0070016712.
- [2] Anderson Jr., J. D.: Modern Compressible Flow. 3<sup>rd</sup> edition. McGraw Hill, Inc., 2004. ISBN: 978-0071241366.
- [3] Aso, S., Hakim, A. N., Miyamoto, S., Inoue, K., and Tani, Y.: Fundamental Study of Supersonic Combustion in Pure Air Flow with Use of Shock Tunnel. *Acta Astronaut.* 2005, 57 (2-8), pp. 384–389. DOI: 10.1016/j.actaastro.2005.03.055.
- [4] Banica, M. C., Scheuermann, T., Chun, J., Weigand, B., and von Wolfersdorf, J.: Numerical Study of Supersonic Combustion Processes with Central Strut Injection. *J. Propul. Power*, 2010, 26 (4), pp. 869–874. DOI: 10.2514/1.43599.
- [5] Bao, W., Zong, Y., Chang, J., and Yu, D.: Effect of Structural Factors on Maximum Aerodynamic Heat Flux of Strut Leading Surface. *Appl. Therm. Eng.* 2014, 69 (1-2), pp. 188–198. DOI: doi:10.1016/j.applthermaleng.2013.11.068.
- [6] Baumann, E., Pahle, J. W., Davis, M. C., and White, J. T.: X-43A Flush Airdata Sensing System Flight-Test Results. *J. Spacecr. Rockets*, 2010, 47 (1), pp. 48–61. DOI: 10.2514/1.41163.
- [7] Baurle, R. A., Fuller, R. P., White, J. A., Chen, T. H., Gruber, M. R., and Nejad, A. S.: An Investigation of Advanced Fuel Injection Schemes for Scramjet Combustion. 36<sup>th</sup> AIAA Aerospace Sciences Meeting and Exhibit. Reno, NV, USA, 1998. DOI: 10.2514/6.1998-937.

## Bibliography

---

- [8] Benzler, M.: Auslegung eines modellähnlichen Scramjet-Treibstoffinjektors sowie erste numerische Analysen der Innenströmung. Student research project. Institute of Aerodynamics and Gasdynamics, University of Stuttgart, 2011.
- [9] Bertram, M. H., Cary Jr., A. M., and Whitehead Jr., A. H.: Experiments with Hypersonic Turbulent Boundary Layers on Flat Plates and Delta Wings. *AGARD Specialists' Meeting on Hypersonic Boundary Layers and Flow Fields*. London, England, 1968.
- [10] Billig, F. S.: Research on Supersonic Combustion. *J. Propul. Power*, 1993, 9 (4), pp. 499–514. DOI: 10.2514/3.23652.
- [11] Boivin, P., Dauptain, A., Jiménez, C., and Cuenot, B.: Simulation of a Supersonic Hydrogen-Air Autoignition-stabilized Flame using Reduced Chemistry. *Combust. Flame*, 2012, 159 (4), pp. 1779–1790. DOI: 10.1016/j.combustflame.2011.12.012.
- [12] Bouchez, M., Saunier, E., Peres, P., and Lansalot, J.: Advanced Carbon/Carbon Injection Strut for Actual Scramjet. *Space Plane and Hypersonic Systems and Technology Conference*. Norfolk, VA, USA, 1996. DOI: 10.2514/6.1996-4567.
- [13] Bouchez, M., Kergaravat, Y., Saucereau, D., Penanhoat, O., and Scherrer, D.: Scramjet Combustor Design in French PREPHA Program - Final Status in 1998. *8<sup>th</sup> AIAA International Space Planes and Hypersonic Systems and Technologies Conference*. Norfolk, VA, USA, 1998. DOI: 10.2514/6.1998-1534.
- [14] Boussinesq, J.: Essai sur la Théorie des Eaux Courantes. Mémoires présentés par divers savants à l'Académie des Sciences de l'Institut de France, XXIII, 1877. ISBN: 978-1271798728.
- [15] Boyce, R. R., Gerard, S., and Paull, A.: The HyShot Scramjet Flight Experiment - Flight Data and CFD Calculations Compared. *12<sup>th</sup> AIAA International Space Planes and Hypersonic Systems and Technologies Conference*. Norfolk, VA, USA, 2003. DOI: 10.2514/6.2003-7029.
- [16] Boyce, R. R., Tirtrey, S. C., Brown, L., Creagh, M., and Ogawa, H.: SCRAMSPACE : Scramjet-based Access-to-Space Systems. *17<sup>th</sup> AIAA International Space Planes and Hypersonic Systems and Technologies Conference*. San Francisco, CA, USA, 2011. DOI: 10.2514/6.2011-2297.
- [17] Bredberg, J.: On the Wall Boundary Condition for Turbulence Models. Technical report, 00/4. Department of Thermo and Fluid Dynamics, Chalmers University of Technology, 2000.

- 
- [18] Bühler, M. N., Förster, F. J., Dröske, N. C., von Wolfersdorf, J., and Weigand, B.: Design of a Focusing Schlieren Setup for Use in a Supersonic Combustion Chamber. *30<sup>th</sup> International Symposium on Shock Waves*. Tel Aviv, Israel, 2015.
- [19] Cabell, K., Hass, N., Storch, A., and Gruber, M.: HIFiRE Direct-Connect Rig (HDCR) Phase I Scramjet Test Results from the NASA Langley Arc-Heated Scramjet Test Facility. *17<sup>th</sup> AIAA International Space Planes and Hypersonic Systems and Technologies Conference*. San Francisco, CA, USA, 2011. DOI: 10.2514/6.2011-2248.
- [20] Cain, T.: Reconstructing the HyShot Flights. Technical report, RTO-EN-AVT-130 - Flight Experiments for Hypersonic Vehicle Development. NATO Science and Technology Organization, 2007, pp. 9.1–9.18.
- [21] Carroll, B. F. and Dutton, J. C.: Characteristics of Multiple Shock Wave/Turbulent Boundary Layer Interactions in Rectangular Ducts. *J. Propul. Power*, 1990, 6 (2), pp. 186–193. DOI: 10.2514/3.23243.
- [22] Cecere, D., Giacomazzi, E., and Ingenito, A.: A Review on Hydrogen Industrial Aerospace Applications. *Int. J. Hydrogen Energy*, 2014, 39 (20), pp. 10731–10747. DOI: 10.1016/j.ijhydene.2014.04.126.
- [23] Chang, Y.-W.: The First Decade of Commercial Space Tourism. *Acta Astronaut.* 2015, 108, pp. 79–91. DOI: 10.1016/j.actaastro.2014.12.004.
- [24] Charyulu, B. V. N., Kurian, J., Venugopalan, P., and Sriramulu, V.: Experimental Study on Mixing Enhancement in Two Dimensional Supersonic Flow. *Exp. Fluids*, 1998, 24 (4), pp. 340–346. DOI: 10.1007/s003480050181.
- [25] Chase Jr., M. W., Davies, J., Downey Jr., J. R., Frurip, D. J., McDonald, R. A., and Syverud, A. N.: JANAF Thermochemical Tables. *J. Phys. Chem. Ref. Data*, 1985, 14, Suppl. 1.
- [26] Coles, D.: Measurements in the Boundary Layer on a Smooth Flat Plate in Supersonic Flow. PhD thesis. California Institute of Technology, 1953.
- [27] Crocco, L.: One-dimensional Treatment of Steady Gas Dynamics. In: *Fundamentals of Gas-Dynamics, Vol. 3*. Ed. by Emmons, H. W., Princeton University Press, 1958. ISBN: 978-0691079691.
- [28] Cummings, E. B.: Laser-induced Thermal Acoustics: Simple Accurate Gas Measurements. *Opt. Lett.* 1994, 19 (17), pp. 1631–1363. DOI: 10.1364/OL.19.001361.

## Bibliography

---

- [29] Cummings, E. B., Leyva, I. A., and Hornung, H. G.: Laser-induced Thermal Acoustics (LITA) Signals from Finite Beams. *Appl. Opt.* 1995, 34 (18), pp. 3290–3302. DOI: 10.1364/AO.34.003290.
- [30] Curran, E. T.: Scramjet Engines: The First Forty Years. *J. Propul. Power*, 2001, 14 (6), pp. 1138–1148. DOI: 10.2514/2.5875.
- [31] Davis, M. C. and White, J. T.: Flight-Test-Determined Aerodynamic Force and Moment Characteristics of the X-43A at Mach 7.0. *14<sup>th</sup> AIAA/AHI Space Planes and Hypersonic Systems and Technologies Conference*. Canberra, Australia, 2008. DOI: 10.2514/6.2006-8028.
- [32] de Charentenay, J. and Ern, A.: Multicomponent Transport Impact on Turbulent Premixed H<sub>2</sub>/O<sub>2</sub> Flames. *Combust. Theor. Model.* 2002, 6 (3), pp. 439–462. DOI: 10.1088/1364-7830/6/3/304.
- [33] Debout, B. and Mathieu, C.: French PREPHA Program - Status Report. *4<sup>th</sup> Symposium on Multidisciplinary Analysis and Optimization*. Cleveland, OH, USA, 1992. DOI: 10.2514/6.1992-5107.
- [34] Dessornes, O. and Scherrer, D.: Tests of the JAPHAR Dual Mode Ramjet Engine. *Aerosp. Sci. Technol.* 2005, 9 (3), pp. 211–221. DOI: 10.1016/j.ast.2005.01.007.
- [35] Deutsche Forschungsgemeinschaft: Basic Research and Technologies for Two-Stage-to-Orbit Vehicles. Final Report of the Collaborative Research Centres 253, 255 and 259. Ed. by Jacob, D. and Sachs, G. and Wagner, S., Wiley-VCH, 2005. ISBN: 978-3527277358.
- [36] Dilley, A. D.: Evaluation of CFD Turbulent Heating Prediction Techniques and Comparison With Hypersonic Experimental Data. Technical report, NASA/CR-2001-210837. National Aeronautics and Space Administration, 2001.
- [37] Dolling, D. S.: Fifty Years of Shock-Wave/Boundary-Layer Interaction Research: What Next? *AIAA J.* 2001, 39 (8), pp. 1517–1531. DOI: 10.2514/2.1476.
- [38] Dröske, N. C., Makowka, K., Nizenkov, P., Vellaramkalayil, J. J., Sattelmayer, T., and von Wolfersdorf, J.: Validation of a Novel OpenFOAM Solver using a Supersonic, Non-reacting Channel Flow. *19<sup>th</sup> AIAA International Space Planes and Hypersonic Systems and Technologies Conference*. Atlanta, GA, USA, 2014. DOI: 10.2514/6.2014-3088.

- [39] Dröske, N. C., Förster, F. J., Weigand, B., and von Wolfersdorf, J.: Investigation of Heat Loads onto an Internally Cooled Strut Injector for Scramjet Application. *20<sup>th</sup> AIAA International Space Planes and Hypersonic Systems and Technologies Conference*. Glasgow, Scotland, 2015. DOI: 10.2514/6.2015-3555.
- [40] Duveau, P., Hallard, R., and Novelli, P.: Aerodynamic Performance Analysis of the Hypersonic Airbreathing Vehicle JAPHAR. *14<sup>th</sup> International Symposium on Air Breathing Engines*. Florence, Italy, 1999.
- [41] Eckerle, W. A., Sheibani, H., and Awad, J.: Experimental Measurement of the Vortex Development Downstream of a Lobed Forced Mixer. *J. Eng. Gas Turbines Power*, 1992, 114 (1), pp. 63–71. DOI: 10.1115/1.2906308.
- [42] Eggers, T., Novelli, P., and Haupt, M.: Design Studies of the JAPHAR Experimental Vehicle for Dual Mode Ramjet Demonstration. *10<sup>th</sup> AIAA/NAL-NASDA-ISAS International Space Planes and Hypersonic Systems and Technologies Conference*. Kyoto, Japan, 2001. DOI: 10.2514/6.2001-1921.
- [43] Ern, A. and Giovangigli, V.: Fast and Accurate Multicomponent Transport Property Evaluation. *J. Comput. Phys.* 1995, 120 (1), pp. 105–116. DOI: 10.1006/jcph.1995.1151.
- [44] Ettner, F. A.: Effiziente numerische Simulation des Deflagrations-Detonations-Übergangs. PhD thesis. Lehrstuhl für Thermodynamik, Technische Universität München, 2013. ISBN: 978-3843910309.
- [45] Falempin, F., Scherrer, D., and Rostand, P.: French Hypersonic Propulsion Program PREPHA – Results, Lessons and Perspectives. *8<sup>th</sup> AIAA International Space Planes and Hypersonic Systems and Technologies Conference*. Norfolk, VA, USA, 1998. DOI: 10.2514/6.1998-1565.
- [46] Fedorova, N. N. and Fedorchenko, I. A.: Computations of Interaction of an Incident Oblique Shock Wave with a Turbulent Boundary Layer on a Flat Plate. *J. Appl. Mech. Tech. Phys.* 2004, 45 (3), pp. 358–366. DOI: 10.1023/B:JAMT.0000025017.49191.14.
- [47] Ferri, A.: Possible Directions of Future Research in Air-Breathing Engines. *Combustion and Propulsion. Fourth AGARD Colloquium, Milan, April 4-8, 1960. High Mach Number Air-breathing Engines*. Pergamon Press, 1960, pp. 3–15.
- [48] Ferri, A.: Review of Scramjet Propulsion Technology. *J. Aircr.* 1968, 5 (1), pp. 3–10. DOI: 10.2514/3.43899.
- [49] Fick, A.: Über Diffusion. *Ann. Phys.* 1855, 170 (1), pp. 59–86. DOI: 10.1002/andp.18551700105.

## Bibliography

---

- [50] Förster, F. J., Baab, S., Lamanna, G., and Weigand, B.: Temperature and Velocity Determination of Shock-heated Flows with Non-resonant Heterodyne Laser-induced Thermal Acoustics. *Appl. Phys. B*, 2015, 121 (3), pp. 235–248. DOI: 10.1007/s00340-015-6217-7.
- [51] Förster, F. J.: Laser-Induced Thermal Acoustics: Simultaneous Velocimetry and Thermometry for the Study of Compressible Flows. PhD thesis. Institute of Aerospace Thermodynamics, University of Stuttgart, 2016.
- [52] Förster, F. J., Dröske, N. C., Bühler, M. N., von Wolfersdorf, J., and Weigand, B.: Analysis of Flame Characteristics in a Scramjet Combustor with Staged Fuel Injection using Common Path Focusing Schlieren and Flame Visualization. *Combust. Flame*, 2016, 168, pp. 204–215. DOI: 10.1016/j.combustflame.2016.03.010.
- [53] Fry, R. S.: A Century of Ramjet Propulsion Technology Evolution. *J. Propul. Power*, 2004, 20 (1), pp. 27–58. DOI: 10.2514/1.9178.
- [54] Fureby, C., Nordin-Bates, K., Petterson, K., Bresson, A., and Sabelnikov, V.: A Computational Study of Supersonic Combustion in Strut Injector and Hypermixer Flow Fields. *Proc. Combust. Inst.* 2015, 35 (2), pp. 2127–2135. DOI: 10.1016/j.proci.2014.06.113.
- [55] Gaisbauer, U. and Weigand, B.: Research Training Group GRK 1095/2: ‘Aero-thermodynamic Design of a Scramjet Propulsion System’. *20<sup>th</sup> International Symposium on Air Breathing Engines*. Gothenburg, Sweden, 2011. ISBN: 978-1618391803.
- [56] Gaisbauer, U., Weigand, B., and Yaroslavtsev, M. I.: Aero-thermodynamic Design of a Scramjet Propulsion System GRK 1095 – Ground Testing. *29<sup>th</sup> Congress of the International Council of the Aeronautical Science*. Novosibirsk, Russia, 2014.
- [57] Gardner, A. D., Hannemann, K., Paull, A., and Steelant, J.: Ground Testing of the HyShot Supersonic Combustion Flight Experiment in HEG. *Proceedings of the 24<sup>th</sup> International Symposium on Shock Waves*. Beijing, China, 2004, pp. 329–334. DOI: 10.1007/978-3-540-27009-6\_47.
- [58] Gaskell, P. H. and Lau, A. K. C.: Curvature-compensated Convective Transport: SMART, A New Boundedness-preserving Transport Algorithm. *Int. J. Numer. Methods Fluids*, 1988, 8 (6), pp. 617–641. DOI: 10.1002/flid.1650080602.

- [59] Gaston, M. J., Mudford, N. R., and Houwing, F.: A Comparison of Two Hypermixing Fuel Injectors in a Supersonic Combustor. *36<sup>th</sup> Aerospace Sciences Meeting and Exhibit*. Reno, NV, USA, 1998. DOI: 10.2514/6.1998-964.
- [60] Gaston, M. J., Mudford, N. R., and Houwing, F.: Effect of Heat Release on Hypermixing Fuel Injector Performance in a Supersonic Combustor. *13<sup>th</sup> Australasian Fluid Mechanics Conference*. Melbourne, Australia, 1998.
- [61] Gerlinger, P.: Numerische Verbrennungssimulation. Effiziente numerische Simulation turbulenter Verbrennung. Springer Verlag, 2005. ISBN: 978-3540233374.
- [62] Gerlinger, P., Kasal, P., Schneider, F., von Wolfersdorf, J., Weigand, B., and Aigner, M.: Experimental and Numerical Investigation of Lobed Strut Injectors for Supersonic Combustion. In: *Basic Research and Technologies for Two-Stage-to-Orbit Vehicles. Final Report of the Collaborative Research Centres 253, 255 and 259*. Ed. by Jacob, D. and Sachs, G. and Wagner, S., Wiley-VCH, 2005. ISBN: 978-3527277358.
- [63] Gerlinger, P., Schneider, F., and Aigner, M.: Numerical Investigation of Mixing Enhancement by Streamwise Vorticity in Supersonic Combustors. *17<sup>th</sup> International Symposium on Air Breathing Engines*. Munich, Germany, 2005.
- [64] Gerlinger, P., Stoll, P., Kindler, M., Schneider, F., and Aigner, M.: Numerical Investigation of Mixing and Combustion Enhancement in Supersonic Combustors by Strut Induced Streamwise Vorticity. *Aerosp. Sci. Technol.* 2008, 12 (2), pp. 159–168. DOI: 10.1016/j.ast.2007.04.003.
- [65] Gerlinger, P. and Simson, Y. H.: Numerical Simulation of the Internal and External Flow Fields and Heat Fluxes of a Lobed Strut Injector. *21<sup>st</sup> International Symposium on Air Breathing Engines*. Busan, Korea, 2013.
- [66] Goynes, C. P., Rodriguez, C. G., Krauss, R. H., McDaniel, J. C., and McClinton, C. R.: Experimental and Numerical Study of a Dual-Mode Scramjet Combustor. *J. Propul. Power*, 2006, 22 (3), pp. 481–489. DOI: 10.2514/1.13215.

## Bibliography

---

- [67] Greenshields, C. J., Weller, H. G., Gasparini, L., and Reese, J. M.: Implementation of Semi-Discrete, Non-staggered Central Schemes in a Colocated, Polyhedral, Finite Volume Framework, for High-speed Viscous Flows. *Int. J. Numer. Methods Fluids*, 2009. DOI: 10.1002/flid.2069.
- [68] Hannemann, K., Schramm, J. M., Karl, S., Haidn, O. J., Ciezki, H. K., Oswald, M., Sender, J., Clauss, W., Manfretti, C., Lamanna, G., Stotz, I., Weigand, B., Steelant, J., and Mack, A.: Combustion Experiments performed within the LAPCAT I Project – an Overview. *16<sup>th</sup> AIAA/DLR/DGLR International Space Planes and Hypersonic Systems and Technologies Conference*. Bremen, Germany, 2009. DOI: 10.2514/6.2009-7206.
- [69] Hannemann, K., Karl, S., Martinez-Schramm, J., and Steelant, J.: Methodology of a Combined Ground Based Testing and Numerical Modelling Analysis of Supersonic Combustion Flow Paths. *Shock Waves*, 2010, 20 (5), pp. 353–366. DOI: 10.1007/s00193-010-0269-8.
- [70] Hell, A.: Validierung der Lasermesstechnik Laser-induzierte Thermische Akustik für die Anwendung in turbulenten, chemisch reagierenden Überschallfreistrahlen. PhD thesis. Institute of Aerospace Thermodynamics, University of Stuttgart, 2012. ISBN: 978-3843907491.
- [71] Hell, A., Förster, F. J., and Weigand, B.: Validation of Laser-Induced Thermal Acoustics for Chemically Reacting H<sub>2</sub>/Air Free Jets. *J. Raman Spectrosc.* 2015. DOI: 10.1002/jrs.4859.
- [72] Hsu, K.-Y., Carter, C. D., Gruber, M. R., Barhorst, T., and Smith, S.: Experimental Study of Cavity-Strut Combustion in Supersonic Flow. *J. Propul. Power*, 2010, 26 (6), pp. 1237–1246. DOI: 10.2514/1.45767.
- [73] Hu, J., Chang, J., Bao, W., Yang, Q., and Wen, J.: Experimental study of a flush wall scramjet combustor equipped with strut/wall fuel injection. *Acta Astronaut.* 2014, 104 (1), pp. 84–90. DOI: 10.1016/j.actaastro.2014.07.012.
- [74] Huang, Z., Zhu, Y.-H., Xiong, Y.-B., and Jiang, P.-X.: Investigation of Transpiration Cooling for Sintered Metal Porous Struts in Supersonic Flow. *Appl. Therm. Eng.* 2014, 70 (1), pp. 240–249. DOI: 10.1016/j.applthermaleng.2014.02.076.
- [75] Huang, Z., Zhu, Y.-H., Jiang, P.-X., and Xiong, Y.-B.: Investigation of a Porous Transpiration-Cooled Strut Injector. *J. Propul. Power*, 2015, 31 (1), pp. 278–285. DOI: 10.2514/1.B35371.

- [76] Jachimowski, C. J.: An Analysis of Combustion Studies in Shock Expansion Tunnels and Reflected Shock Tunnels. Technical report, NASA TP-3224. National Aeronautics and Space Administration, 1992.
- [77] Jasak, H., Weller, H. G., and Gosman, A. D.: High Resolution NVD Differencing Scheme for Arbitrarily Unstructured Meshes. *Int. J. Numer. Methods Fluids*, 1999, 31, pp. 431–449. DOI: 10.1002/(SICI)1097-0363(19990930)31:2<431::AID-FLD884>3.0.CO;2-T.
- [78] Jasak, H., Jemcov, A., and Tukovic, Z.: OpenFOAM: A C++ Library for Complex Physics Simulations. *International Workshop on Coupled Methods in Numerical Dynamics*. Dubrovnik, Croatia, 2007.
- [79] Jeong, E., Jeung, I.-S., O’Byrne, S., and Houwing, A. F. P.: Investigation of Supersonic Combustion with Angled Injection in a Cavity-Based Combustor. *J. Propul. Power*, 2008, 24 (6), pp. 1258–1268. DOI: 10.2514/1.36519.
- [80] Jewell, J. S., Miller, J. H., and Kimmel, R. L.: Correlation of HIFiRE-5 Flight Data with Computed Pressure and Heat Transfer. *45<sup>th</sup> AIAA Thermophysics Conference*. Dallas, TX, USA, 2015. DOI: 10.2514/6.2015-2319.
- [81] Kays, W. M.: Turbulent Prandtl Number – Where Are We? *J. Heat Transfer*, 1994, 16 (2), pp. 284–295. DOI: 10.1115/1.2911398.
- [82] Kimmel, R. L., Adamczak, D., Juliano, T. J., and DSTO AVD Brisbane Team: HIFiRE-5 Flight Test Preliminary Results. *51<sup>st</sup> AIAA Aerospace Sciences Meeting including the New Horizons Forum and Aerospace Exposition*. Grapevine, TX, USA, 2013. DOI: 10.2514/6.2013-377.
- [83] Kirstein, S., Maier, D., Fuhrmann, T., Hupfer, A., and Kau, H. P.: Experimental Study on Staged Injection in a Supersonic Combustor. *16<sup>th</sup> AIAA/DLR/DGLR International Space Planes and Hypersonic Systems and Technologies Conference*. Bremen, Germany, 2009. DOI: 10.2514/6.2009-7343.
- [84] Koelle, D. E.: Launch Cost Analyses for Reusable Space Transportation Systems (Sänger II). *Acta Astronaut.* 1989, 19 (2), pp. 191–197. DOI: 10.1016/0094-5765(89)90101-X.
- [85] Koelle, D. E., Sacher, P., and Grallert, H.: Deutsche Raketenflugzeuge und Raumtransporter-Projekte. Die Deutsche Luftfahrt. Bernard & Graefe Verlag, 2007. ISBN: 978-3763761265.
- [86] Kouchi, T., Goyne, C. P., Rockwell Jr., R. D., and McDaniel, J. C.: Focusing-schlieren Visualization in a Dual-mode Scramjet. *Exp. Fluids*, 2015, 56 (12). DOI: 10.1007/s00348-015-2081-9.

## Bibliography

---

- [87] Kubo, N., Murakami, A., Kudo, K., and Tomioka, S.: An Experimental Investigation on Combustion Characteristics of Hypermixer Injectors – Effects of the ‘Swept’ Applied to Hypermixer Injector Ramps. *Procedia Eng.* 2015, 99, pp. 954–960. DOI: 10.1016/j.proeng.2014.12.627.
- [88] Kurganov, A. and Tadmor, E.: New High-Resolution Central Schemes for Nonlinear Conservation Laws and Convection-Diffusion Equations. *J. Comput. Phys.* 2000, 260, pp. 241–262. DOI: 10.1006/jcph.2000.6459.
- [89] Launder, B. E. and Sharma, B. I.: Application of the Energy-dissipation Model of Turbulence to the Calculation of Flow near a Spinning Disc. *Lett. Heat Mass Transfer*, 1974, 1 (2), pp. 131–137. DOI: 10.1016/0094-4548(74)90150-7.
- [90] Launder, B. E. and Spalding, D. B.: The Numerical Computation of Turbulent Flows. *Comput. Meth. Appl. Mech. Eng.* 1974, 3 (2), pp. 269–289. DOI: 10.1016/0045-7825(74)90029-2.
- [91] Laurence, S. J., Martinez-Schramm, J., Karl, S., and Hannemann, K.: An Experimental Investigation of Steady and Unsteady Combustion Phenomena in the HyShot II Combustor. *17<sup>th</sup> AIAA International Space Planes and Hypersonic Systems and Technologies Conference*. San Francisco, CA, USA, 2011. DOI: 10.2514/6.2011-2310.
- [92] Lederer, R., Schwab, R., and Voss, N.: Hypersonic Airbreathing Propulsion Activities for SÄNGER. *3<sup>rd</sup> International Aerospace Planes Conference*. Orlando, FL, USA, 1991. DOI: 10.2514/6.1991-5040.
- [93] Lemmon, E.W., Huber, M.L., and McLinden, M.O.: *NIST Standard Reference Database 23: Reference Fluid Thermodynamic and Transport Properties-REFPROP, Version 9.1*. National Institute of Standards and Technology, Standard Reference Data Program, Gaithersburg, 2013.
- [94] Lewis, M.: X51 Scrams into the Future. *Aerosp. Am.* 10/2010, pp. 26–31.
- [95] Lindblad, I. A. A., Wallin, S., Johansson, A. V., Friedrich, R., Lechner, R., Krogmann, P., Schülein, E., Courty, J.-C., Ravachol, M., and Giordano, D.: A Prediction Method for High Speed Turbulent Separated Flows with Experimental Verification. *29<sup>th</sup> AIAA Fluid Dynamics Conference*. Albuquerque, NM, USA, 1998. DOI: 10.2514/6.1998-2547.
- [96] Lorin, R.: Le Propulseur à Échappement et l’Aéroplane à Grande Vitesse. *L’Aérophile*, 09/1908, pp. 332–336.
- [97] MacLean, M., Wadhams, T., Holden, M., and Johnson, H.: Ground Test Studies of the HIFiRE-1 Transition Experiment Part 2: Computational Analysis. *J. Spacecr. Rockets*, 2008, 46 (6), pp. 1149–1164. DOI: 10.2514/1.37693.

- 
- [98] Makowka, K., Gurtner, M., Paukner, D., Sattelmayer, T., and Kau, H. P.: Numerical and Experimental Investigation of a Central Strut Injector with Perpendicular Injection for Scramjet Applications. *5<sup>th</sup> European Conference for Aeronautic and Space Sciences*. Munich, Germany, 2013.
- [99] Makowka, K., Dröske, N. C., Vellaramkalayil, J. J., von Wolfersdorf, J., and Sattelmayer, T.: Unsteady RANS Investigation of a Hydrogen-Fueled Staged Supersonic Combustor with Lobed Injectors. *19<sup>th</sup> AIAA International Space Planes and Hypersonic Systems and Technologies Conference*. Atlanta, GA, USA, 2014. DOI: 10.2514/6.2014-3215.
- [100] Makowka, K., Sattelmayer, T., Gurtner, M., Paukner, D., and Haidn, O.: Semi-Zonal Hybrid RANS/LES Turbulence Modeling with RANS Sensor Based Interfacing Applied to Supersonic Flows. *19<sup>th</sup> AIAA International Space Planes and Hypersonic Systems and Technologies Conference*. Atlanta, GA, USA, 2014. DOI: 10.2514/6.2014-3087.
- [101] Makowka, K.: Numerically Efficient Hybrid RANS/LES of Supersonic Combustion. PhD thesis. Lehrstuhl für Thermodynamik, Technische Universität München, 2015. ISBN: 978-3843924566.
- [102] Marshall, L. A., Bahm, C., Corpening, G. P., and Sherrill, R.: Overview With Results and Lessons Learned of the X-43A Mach 10 Flight. *13<sup>th</sup> AIAA/CIRA International Space Planes and Hypersonics Systems and Technologies Conference*. Capua, Italy, 2005. DOI: 10.2514/6.2005-3336.
- [103] Martinez-Schramm, J., Karl, S., Hannemann, K., and Steelant, J.: Ground Testing of the HyShot II Scramjet Configuration in HEG. *15th AIAA International Space Planes and Hypersonic Systems and Technologies Conference*. Dayton, OH, USA, 2008. DOI: 10.2514/6.2008-2547.
- [104] Martinez-Schramm, J., Hannemann, K., Karl, S., Defoort, S., Viguier, P., and Steelant, J.: Ground Testing Synthesis of the LAPCAT II Small Scale Flight Experiment Configuration Scramjet Flow Path. *20<sup>th</sup> AIAA International Space Planes and Hypersonic Systems and Technologies Conference*. Glasgow, Scotland, 2015. DOI: 10.2514/6.2015-3627.
- [105] Masuya, G., Komuro, T., Murakami, A., Shinozaki, N., Nakamura, A., Murayama, M., and Ohwaki, K.: Ignition and Combustion Performance of Scramjet Combustors with Fuel Injection Struts. *J. Propul. Power*, 1995, 11 (2), pp. 301–307. DOI: 10.2514/3.51425.
- [106] Matsuo, K., Miyazato, Y., and Kim, H.-D.: Shock Train and Pseudo-shock Phenomena in Internal Gas Flows. *Prog. Aerosp. Sci.* 1999, 35 (1), pp. 33–100. DOI: 10.1016/S0376-0421(98)00011-6.

## Bibliography

---

- [107] McBride, B. J. and Gordon, S.: Computer Program for Calculating and Fitting Thermodynamic Functions. Technical report, NASA RP-1271. National Aeronautics and Space Administration, 1992.
- [108] McClinton, C. R., Rausch, V. L., Nguyen, L. T., and Sitz, J. R.: Preliminary X-43 Flight Test Results. *Acta Astronaut.* 2005, 57 (2-8), pp. 266–276. DOI: 10.1016/j.actaastro.2005.03.060.
- [109] Menter, F. R.: Two-Equation Eddy-Viscosity Turbulence Models for Engineering Applications. *AIAA J.* 1994, 32, No. 8, pp. 1598–1605. DOI: 10.2514/3.12149.
- [110] Menter, F. R., Kuntz, M., and Langtry, R. B.: Ten Years of Industrial Experience with the SST Turbulence Model. *Turbulence, Heat and Mass Transfer IV*. Antalya, Turkey, 2003.
- [111] Merlin, P. W.: Design and Development of the Blackbird: Challenges and Lessons Learned. *47<sup>th</sup> AIAA Aerospace Sciences Meeting including The New Horizons Forum and Aerospace Exposition*. Orlando, FL, USA, 2009. DOI: 10.2514/6.2009-1522.
- [112] Mills, A. F.: Basic Heat and Mass Transfer. 2<sup>nd</sup> edition. Prentice Hall, 1999. ISBN: 978-0130962478.
- [113] Moffat, R. J.: Contributions to the Theory of Single-Sample Uncertainty Analysis. *J. Fluids Eng.* 1981, 104 (2), pp. 250–258. DOI: 10.1115/1.3241818.
- [114] Moffat, R. J.: Describing the Uncertainties in Experimental Results. *Exp. Therm Fluid Sci.* 1988, 1 (1), pp. 3–17. DOI: 10.1016/0894-1777(88)90043-X.
- [115] Mohieldin, T. O., Tiwari, S. N., and Olynciw, M. J.: Asymmetric Flow-Structures in Dual Mode Scramjet Combustor With Significant Upstream Interaction. *37<sup>th</sup> AIAA/ASME/SAE/ASEE Jet Propulsion Conference & Exhibit*. Norfolk, VA, USA, 2001. DOI: 10.2514/6.2001-3296.
- [116] Moses, P. L., Rausch, V. L., Nguyen, L. T., and Hill, J. R.: NASA Hypersonic Flight Demonstrators – Overview, Status, and Future Plans. *Acta Astronaut.* 2004, 55 (3-9), pp. 619–630. DOI: 10.1016/j.actaastro.2004.05.045.
- [117] Narayanswami, N., Knight, D. D., and Horstman, C. C.: Investigation of a Hypersonic Crossing Shock Wave/Turbulent Boundary Layer Interaction. *Shock Waves*, 1992, 3 (1), pp. 35–48. DOI: 10.1007/BF01414746.

- 
- [118] Nizenkov, P.: Numerical Investigation of the Flow inside a Scramjet Combustion Chamber with a Novel OpenFOAM-Solver. Diploma thesis. Institute of Aerospace Thermodynamics, University of Stuttgart, 2013.
- [119] Novelli, P. and Koschel, W.: Progress of the JAPHAR Cooperation between ONERA and DLR on Hypersonic Airbreathing Propulsion. *10<sup>th</sup> International Space Planes and Hypersonic Systems and Technologies Conference*. Kyoto, Japan, 2001. DOI: 10.2514/6.2001-1870.
- [120] *NPARC Alliance Validation Archive: Mach 4.5 Turbulent Flow over a Flat Plate*. 01/27/2012. URL: <http://www.grc.nasa.gov/WWW/wind/valid/fpmach45/fpmach45.html> (visited on 02/24/2016).
- [121] *NPARC Alliance Validation Archive: Oblique Shock on a 15 Degree Wedge at Mach 2.5*. 03/12/2012. URL: <http://www.grc.nasa.gov/WWW/wind/valid/wedge/wedge.html> (visited on 02/24/2016).
- [122] Oschwald, M., Guerra, R., and Waidmann, W.: Investigation of the Flowfield of a Scramjet Combustor with Parallel H<sub>2</sub>-Injection through a Strut by Particle Image Displacement Velocimetry. *Int. J. Energ. Mater. Chem. Propul.* 1994, 3 (1-6), pp. 498–503. DOI: 10.1615/IntJEnergeticMaterialsChemProp.v3.i1-6.510.
- [123] Osher, S. and Sanders, R.: Numerical Approximations to Nonlinear Conservation Laws with Locally Varying Time and Space Grids. *Math. Comput.* 1983, 41 (164), pp. 321–336. DOI: 10.1090/S0025-5718-1983-0717689-8.
- [124] Paull, A., Alesi, H., and Anderson, S.: The Development of the HyShot Flight Program. *Proceedings of the 24<sup>th</sup> International Symposium on Shock Waves*. Beijing, China, 2004, pp. 31–48. DOI: 10.1007/978-3-540-27009-6\_4.
- [125] Pezzella, G., Marini, M., Cicala, M., Vitale, A., Langener, T., and Steelant, J.: Aerodynamic Characterization of HEXAFLY Scramjet Propelled Hypersonic Vehicle. *32<sup>nd</sup> AIAA Applied Aerodynamics Conference*. Atlanta, GA, USA, 2014. DOI: 10.2514/6.2014-2844.
- [126] Presz Jr., W., Gousy, R., and Morin, B.: Forced Mixer Lobes in Ejector Designs. *22<sup>nd</sup> AIAA/ASME/SAE/ASEE Joint Propulsion Conference*. Huntsville, AL, USA, 1986. DOI: 10.2514/6.1986-1614.
- [127] Presz Jr., W., Blinn, R. F., and Morin, B.: Short Efficient Ejector Systems. *23<sup>rd</sup> AIAA/SAE/ASME/ASEE Joint Propulsion Conference*. San Diego, CA, USA, 1987. DOI: 10.2514/6.1987-1837.

## Bibliography

---

- [128] René-Corail, M., Rothmund, C., Ferrandon, O., and Dessornes, O.: A Hydrogen Cooled Injection Strut Design for Scramjet. *7<sup>th</sup> AIAA International Space Planes and Hypersonic Systems and Technologies Conference*. Norfolk, VA, USA, 1996. DOI: 10.2514/6.1996-4511.
- [129] Rocci Denis, S., Kau, H. P., and Brandstetter, A.: Experimental Study on Transition between Ramjet and Scramjet Modes in a Dual-Mode Combustor. *12<sup>th</sup> AIAA International Space Planes and Hypersonic Systems and Technologies Conference*. Norfolk, VA, USA, 2003. DOI: 10.2514/6.2003-7048.
- [130] Rodriguez, C. G.: Asymmetry Effects in Numerical Simulation of Supersonic Flows with Upstream Separated Regions. *39<sup>th</sup> AIAA Aerospace Sciences Meeting & Exhibit*. Reno, NV, USA, 2001. DOI: 10.2514/6.2001-84.
- [131] Roe, P. L.: Approximate Riemann Solvers, Parameter Vectors, and Difference Schemes. *J. Comput. Phys.* 1981, 43 (2), pp. 357-372. DOI: 10.1016/0021-9991(81)90128-5.
- [132] Rondeau, C. M. and Jorris, T. R.: X-51A Scramjet Demonstrator Program: Waverider Ground and Flight Test. *SFTE 44<sup>th</sup> International / SETP Southwest Flight Test Symposium*. Ft Worth, TX, USA, 2013.
- [133] Rothmund, C., Scherrer, D., Levy, F., and Bouchez, M.: Propulsion System for Airbreathing Launcher in the French PREPHA Program. *Space Plane and Hypersonic Systems and Technology Conference*. Norfolk, VA, USA, 1996. DOI: 10.2514/6.1996-4498.
- [134] Roy, M.: Thermodynamique des Systèmes Propulsifs à Réaction et de la Turbine à Gaz ; Leçons Professées au Centre d'Études Supérieures de Mécanique. Dunod, 1947.
- [135] Rust, B., Gerlinger, P., Lourier, J.-M., Kindler, M., and Aigner, M.: Numerical Simulation of the Internal and External Flowfields of a Scramjet Fuel Strut Injector Including Conjugate Heat Transfer. *17<sup>th</sup> AIAA International Space Planes and Hypersonic Systems and Technologies Conference*. San Francisco, CA, USA, 2011. DOI: 10.2514/6.2011-2207.
- [136] Sancho, M.: The French Hypersonic Research Program PREPHA: Progress Review. *5<sup>th</sup> International Aerospace Planes and Hypersonics Technologies Conference*. Munich, Germany, 1993. DOI: 10.2514/6.1993-5160.

- 
- [137] Scheel, F., Ciezki, H. K., and Haidn, O. J.: Investigation of the Influence of Streamwise Vortices Generating Geometries of Strut Injectors on the Mixing and Combustion Process in a Scramjet Model Combustor. *18<sup>th</sup> International Symposium on Air Breathing Engines*. Beijing, China, 2007.
- [138] Scheuermann, T.: Untersuchungen zur Verbrennung in einer SCRamjet-Brennkammer. PhD thesis. Institute of Aerospace Thermodynamics, University of Stuttgart, 2010. ISBN: 978-3868535952.
- [139] Schlichting, H. and Gersten, K.: *Grenzschicht-Theorie*. Springer Verlag, 2006. ISBN: 978-3662075555.
- [140] Schülein, E., Krogmann, P., and Stanewsky, E.: Documentation of Two-Dimensional Impinging Shock/Turbulent Boundary Layer Interaction Flow. Technical report, IB 223 - 96 A 49. Deutsches Zentrum für Luft- und Raumfahrt e.V., 1996.
- [141] Schülein, E.: Skin-Friction and Heat Flux Measurements in Shock/ Boundary-Layer Interaction Flows. *AIAA J.* 2006, 44 (8), pp. 1732–1741. DOI: 10.2514/1.15110.
- [142] Segal, C.: *The Scramjet Engine. Processes and Characteristics*. Cambridge University Press, 2009. ISBN: 978-0521838153.
- [143] Simson, Y. H. and Gerlinger, P.: High Order Numerical Simulation of the Thermal Load on a Lobed Strut Injector for Scramjet Applications. *Int. J. Numer. Methods Fluids*, 2016. DOI: 10.1002/fld.4224.
- [144] Smart, M. A., Hass, N. E., and Paull, A.: Flight Data Analysis of the HyShot 2 Scramjet Flight Experiment. *AIAA J.* 2006, 44 (10), pp. 2366–2375. DOI: 10.2514/1.20661.
- [145] Smith, L. L., Majamaki, A. J., Lam, I. T., Delabroy, O., Karagozian, A. R., Marble, F. E., and Smith, O. I.: Mixing Enhancement in a Lobed Injector. *Phys. Fluids*, 1997, 9 (3), pp. 667–678. DOI: 10.1063/1.869224.
- [146] Smith, T. R., Bowcutt, K. G., Selmon, J. R., Miranda, L., Northrop, B., Mairs, R., Unger, E. R., Lau, K. Y., Silvester, T., Alesi, H., Paull, A., Paull, R., and Dolvin, D. J.: HIFiRE 4: A Low-Cost Aerodynamics, Stability, and Control Hypersonic Flight Experiment. *17<sup>th</sup> AIAA International Space Planes and Hypersonic Systems and Technologies Conference*. San Francisco, CA, USA, 2011. DOI: 10.2514/6.2011-2275.
- [147] Smits, A. J. and Dussauge, J.-P.: *Turbulent Shear Layers in Supersonic Flow*. 2<sup>nd</sup> edition. New York: Springer-Verlag, 2006. ISBN: 978-0387261409.

## Bibliography

---

- [148] Steelant, J.: LAPCAT: An EC Funded Project on Sustained Hypersonic Flight. *57<sup>th</sup> International Astronautical Congress*. Valencia, Spain, 2006. DOI: 10.2514/6.IAC-06-C4.5.01.
- [149] Steelant, J.: Achievements Obtained for Sustained Hypersonic Flight within the LAPCAT Project. *15<sup>th</sup> AIAA International Space Planes and Hypersonic Systems and Technologies Conference*. Dayton, OH, USA, 2008. DOI: 10.2514/6.2008-2578.
- [150] Steelant, J.: LAPCAT: High-Speed Propulsion Technology. Technical report, RTO-EN-AVT-150 - Advances on Propulsion Technology for High-Speed Aircraft. NATO Science and Technology Organization, 2008, pp. 12.1–12.38.
- [151] Steelant, J.: Sustained Hypersonic Flight in Europe: Technology Drivers for LAPCAT II. *16<sup>th</sup> AIAA/DLR/DGLR International Space Planes and Hypersonic Systems and Technologies Conference*. Bremen, Germany, 2009. DOI: 10.2514/6.2009-7240.
- [152] Steelant, J., Varvill, R., Deefort, S., Hannemann, K., and Marini, M.: Achievements Obtained for Sustained Hypersonic Flight within the LAPCAT II Project. *20<sup>th</sup> AIAA International Space Planes and Hypersonic Systems and Technologies Conference*. Glasgow, Scotland, 2015. DOI: 10.2514/6.2015-3677.
- [153] Stokes, G. G.: On the Theories of Internal Friction of Fluids in Motion, and of the Equilibrium and Motion of Elastic Solids. *Trans. Cambridge Philos. Soc.* 1845, 8, pp. 287–305.
- [154] Strickland, J. H., Selerland, T., and Karagozian, A. R.: Numerical Simulations of a Lobed Fuel Injector. *Phys. Fluids*, 1998, 10 (11), pp. 2950–2964. DOI: 10.1063/1.869815.
- [155] Sugiyama, H., Minato, R., Mizobata, K., Tojo, A., and Muto, Y.: Experimental Investigation on Shock Wave and Turbulent Boundary Layer Interactions in a Square Duct at Mach 2 and 4. *J. Therm. Sci.* 2006, 15 (1), pp. 37–42. DOI: 10.1007/s11630-006-0037-3.
- [156] Sunami, T., Wendt, M. N., and Nishioka, M.: Supersonic Mixing and Combustion Control using Streamwise Vortices. *34<sup>th</sup> AIAA/ASME/SAE/ASEE Joint Propulsion Conference and Exhibit*. Cleveland, OH, USA, 1998. DOI: 10.2514/6.1998-3271.

- 
- [157] Sunami, T., Murakami, A., Kudo, K., Kodera, M., and Nishioka, M.: Mixing and Combustion Control Strategies for Efficient Scramjet Operation in Wide Range of Flight Mach Numbers. *11<sup>th</sup> AIAA/AAAF International Conference Space Planes and Hypersonic Systems and Technologies*. Orleans, France, 2002. DOI: 10.2514/6.2002-5116.
- [158] Sunami, T., Magre, P., Bresson, A., Grisch, F., Orain, M., and Kodera, M.: Experimental Study of Strut Injectors in a Supersonic Combustor using OH-PLIF. *13<sup>th</sup> AIAA/CIRA International Space Planes and Hypersonics Systems and Technologies Conference*. Capua, Italy, 2005. DOI: 10.2514/6.2005-3304.
- [159] Sutherland, W.: The Viscosity of Gases and Molecular Force. *Philos. Mag.* 5<sup>th</sup> ser., 1893, 36 (223), pp. 507–531. DOI: 10.1080/14786449308620508.
- [160] Tam, C.-J., Hsu, K.-Y., Gruber, M. R., and Raffoul, C. N.: Aerodynamic Performance of Strut Injection for a Round Scramjet Combustor. *43<sup>rd</sup> AIAA/ASME/SAE/ASEE Joint Propulsion Conference & Exhibit*. Cincinnati, OH, USA, 2007. DOI: 10.2514/6.2007-5403.
- [161] Tani, K., Kanda, T., and Kudou, K.: Aerodynamic Performance of Scramjet Inlet Models with a Single Strut. *J. Propul. Power*, 2006, 22 (4), pp. 905–912. DOI: 10.2514/1.17774.
- [162] Tannehill, J. C., Anderson Jr., J. D., and Pletcher, R. H.: Computational Fluid Mechanics and Heat Transfer. 2<sup>nd</sup> edition. Taylor & Francis, 1997. ISBN: 978-1560320463.
- [163] Thivet, F., Knight, D. D., Zheltovodov, A. A., and Maksimov, A. I.: Insights in Turbulence Modeling for Crossing-Shock-Wave/Boundary-Layer Interactions. *AIAA J.* 2001, 39 (6), pp. 985–995. DOI: 10.2514/2.1417.
- [164] Tirtey, S. C., Boyce, R. R., Brown, L. M., and Creagh, M. A.: The SCRAMSPACE I Hypersonic Flight Experiment Feasibility Study. *17<sup>th</sup> AIAA International Space Planes and Hypersonic Systems and Technologies Conference*. San Francisco, CA, USA, 2011. DOI: 10.2514/6.2011-2277.
- [165] Tomioka, S., Kanda, T., Tani, K., Mitani, T., Shimura, T., and Chinzei, N.: Testing of a Scramjet Engine with a Strut in M8 Flight Conditions. *34<sup>th</sup> AIAA/ASME/SAE/ASEE Joint Propulsion Conference and Exhibit*. Cleveland, OH, USA, 1998. DOI: 10.2514/6.1998-3134.
- [166] Toro, E. F.: *Riemann Solvers and Numerical Methods for Fluid Dynamics*. Springer Verlag, 2009. ISBN: 978-3540252023.

## Bibliography

---

- [167] Ueda, S., Tomioka, S., Ono, F., Sakuranaka, N., Tani, K., and Murakami, A.: Mach 6 Test of a Scramjet Engine with Multi-Staged Fuel Injection. *44<sup>th</sup> AIAA Aerospace Sciences Meeting and Exhibit*. Reno, NV, USA, 2006. DOI: 10.2514/6.2006-1027.
- [168] Ursch, A.: Auslegung, Konstruktion und Inbetriebnahme eines Prüfstandes zur Untersuchung eines modellähnlichen Scramjet-Treibstoffinjektors sowie erste Analysen der Innenströmung. Student research project. Institute of Aerodynamics and Gasdynamics, University of Stuttgart, 2011.
- [169] van Driest, E. R.: Turbulent Boundary Layer in Compressible Fluids. *J. Aeronaut. Sci.* 1951, 18, pp. 145–160. DOI: 10.2514/2.7048.
- [170] van Leer, B.: Towards the Ultimate Conservative Difference Scheme. II. Monotonicity and Conservation Combined in a Second-order Scheme. *J. Comput. Phys.* 1974, 14 (4), pp. 361–370. DOI: 10.1016/0021-9991(74)90019-9.
- [171] van Leer, B., Lee, W.-T., and Roe, P.: Characteristic Time-Stepping or Local Preconditioning of the Euler Equations. *10<sup>th</sup> Computational Fluid Dynamics Conference*. Honolulu, HI, USA, 1991. DOI: 10.2514/6.1991-1552.
- [172] Varvill, R. and Bond, A.: The Skylon Spaceplane: Progress to Realisation. *J. Br. Interplanet. Soc.* 2008, 61 (10), pp. 412–418.
- [173] Vellaramkalayil, J. J., Scheuermann, T., and von Wolfersdorf, J.: Numerical and Experimental Investigation of a Two-Staged Supersonic Combustion Chamber. *16<sup>th</sup> AIAA/DLR/DGLR International Space Planes and Hypersonic Systems and Technologies Conference*. Bremen, Germany, 2009. DOI: 10.2514/6.2009-7363.
- [174] Vellaramkalayil, J. J., Scheuermann, T., Winkler, S., von Wolfersdorf, J., and Banica, M. C.: Experimental and Numerical Study of a Supersonic Combustion Chamber with different Two-Staged Injection Concepts. *46<sup>th</sup> AIAA/ASME/SAE/ASEE Joint Propulsion Conference & Exhibit and 8th Annual International Energy Conversion Engineering Conference*. Nashville, TN, USA, 2010. DOI: 10.2514/6.2010-6647.
- [175] Vellaramkalayil, J. J., Scheuermann, T., and von Wolfersdorf, J.: Analysis of a Two-Staged Supersonic Combustion Chamber using Experiments and Simulations. *17<sup>th</sup> AIAA International Space Planes and Hypersonic Systems and Technologies Conference*. San Francisco, CA, USA, 2011. DOI: 10.2514/6.2011-2247.

- 
- [176] Vellaramkalayil, J. J.: Experimental and Numerical Investigations of Different Injection Schemes in a Supersonic Combustion Chamber. PhD thesis. Institute of Aerospace Thermodynamics, University of Stuttgart, 2014. ISBN: 978-3843917155.
- [177] Volland, R., Huebner, L., and McClinton, C.: X-43 Hypersonic vehicle technology development. *Acta Astronaut.* 2006, 59 (1-5), pp. 181–191. DOI: 10.1016/j.actaastro.2006.02.021.
- [178] von Kármán, T.: Mechanische Ähnlichkeit und Turbulenz. *Nachr. Ges. Wiss. Goettingen*, 1930, 5, pp. 58–76.
- [179] Wadhams, T. P., Mundy, E., MacLean, M. G., and Holden, M. S.: Ground Test Studies of the HIFiRE-1 Transition Experiment Part 1: Experimental Results. *J. Spacecr. Rockets*, 2008, 46 (6), pp. 1134–1148. DOI: 10.2514/1.38338.
- [180] Waidmann, W., Brummund, U., and Nuding, J.: Experimental Investigation of Supersonic Ramjet Combustion (Scramjet). *8<sup>th</sup> International Symposium on Transport Phenomena in Combustion*. San Francisco, CA, USA, 1995.
- [181] Walker, S. H., Rodgers, F. C., and Esposito, A. L.: Hypersonic Collaborative Australia/United States Experiment (HyCAUSE). *13<sup>th</sup> AIAA/CIRA International Space Planes and Hypersonics Systems and Technologies Conference*. Capua, Italy, 2005. DOI: 10.2514/6.2005-3254.
- [182] Walker, S., Rodgers, F., Paull, A., and van Wie, D. M.: HyCAUSE Flight Test Program. *15<sup>th</sup> AIAA International Space Planes and Hypersonic Systems and Technologies Conference*. Dayton, OH, USA, 2008. DOI: 10.2514/6.2008-2580.
- [183] Wang, H., Wang, Z., Sun, M., and Qin, N.: Combustion Characteristics in a Supersonic Combustor with Hydrogen Injection Upstream of Cavity Flameholder. *Proc. Combust. Inst.* 2013, 34 (2), pp. 2073–2082. DOI: 10.1016/j.proci.2012.06.049.
- [184] Weigand, B. and Gaisbauer, U.: An Overview on the Structure and Work of the DFG Research Training Group GRK 1095: ‘Aero-thermodynamic Design of a Scramjet Propulsion System’. *16<sup>th</sup> AIAA/DLR/DGLR International Space Planes and Hypersonic Systems and Technologies Conference*. Bremen, Germany, 2009. DOI: 10.2514/6.2009-7276.
- [185] Weingartner, S.: SÄNGER - The Reference Concept of the German Hypersonics Technology Program. *5<sup>th</sup> International Aerospace Planes and Hypersonics Technologies Conference*. Munich, Germany, 1993. DOI: 10.2514/6.1993-5161.

## Bibliography

---

- [186] Weiss, A., Grzona, A., and Olivier, H.: Behavior of Shock Trains in a Diverging Duct. *Exp. Fluids*, 2009, 49 (2), pp. 355–365. DOI: 10.1007/s00348-009-0764-9.
- [187] Weller, H. G., Tabor, G., Jasak, H., and Fureby, C.: A Tensorial Approach to Computational Continuum Mechanics using Object-oriented Techniques. *Comput. Phys.* 1998, 12 (6), pp. 620–631. DOI: 10.1063/1.168744.
- [188] White, F. M.: Viscous Fluid Flow. 3<sup>rd</sup> edition. McGraw Hill, Inc., 2006. ISBN: 978-0071244930.
- [189] Wilcox, D. C.: Reassessment of the Scale-determining Equation for Advanced Turbulence Models. *AIAA J.* 1988, 26 (11), pp. 1299–1310. DOI: 10.2514/3.10041.
- [190] Wilcox, D. C.: Turbulence Modeling for CFD. DCW Industries, Inc., 1998. ISBN: 978-0963605153.
- [191] Wilson, J. R.: High Hopes for HIFiRE Scramjet. *Aerosp. Am.* 11/2007, pp. 33–37.
- [192] Wollenhaupt, B.: Turbulenzmodellierung mit Tau. Diploma thesis. Institute of Aerospace Thermodynamics, University of Stuttgart, 2007.
- [193] Yang, Q., Bao, W., Zong, Y., Chang, J., Hu, J., and Wu, M.: Combustion Characteristics of a Dual-mode Scramjet Injecting Liquid Kerosene by Multiple Struts. *J. Aerosp. Eng.* 2015, 22 (6), pp. 983–992. DOI: 10.1177/0954410014542447.
- [194] Yu, K. H., Wilson, K. J., and Schadow, K. C.: Effect of Flame-Holding Cavities on Supersonic-Combustion Performance. *J. Propul. Power*, 2001, 17 (6), pp. 1287–1295. DOI: 10.2514/2.5877.
- [195] Zhang, C., Yang, Q., Chang, J., Tang, J., and Bao, W.: Nonlinear Characteristics and Detection of Combustion Modes for a Hydrocarbon Fueled Scramjet. *Acta Astronaut.* 2015, 110, pp. 89–98. DOI: doi:10.1016/j.actaastro.2014.11.023.
- [196] Zhong, F., Chen, T., Fan, X., Chen, L., and Chang, X.: Three-Dimensional Heat Transfer Analysis and Optimized Design of Actively Cooled Strut for Scramjet Applications. *48<sup>th</sup> AIAA/ASME/SAE/ASEE Joint Propulsion Conference & Exhibit*. Atlanta, GA, USA, 2012. DOI: 10.2514/6.2012-3926.

## APPENDIX A

---

### Isentropic Relations

---

Within an isentropic flow of an ideal gas, the static values of pressure, density and temperature can be related to the corresponding total conditions by a set of three equations:

$$\frac{p_t}{p} = \left(1 + \frac{\gamma - 1}{2} M^2\right)^{\frac{\gamma}{\gamma - 1}} \quad (\text{A.1})$$

$$\frac{\rho_t}{\rho} = \left(1 + \frac{\gamma - 1}{2} M^2\right)^{\frac{1}{\gamma - 1}} \quad (\text{A.2})$$

$$\frac{T_t}{T} = \left(1 + \frac{\gamma - 1}{2} M^2\right) \quad (\text{A.3})$$

It is assumed that no heat or work is added to or extracted from the flow. While this is usually not completely accurate for most technical applications, these isentropic relations still provide a reasonable approximation of the flow conditions.

## A Isentropic Relations

---

If a one-dimensional flow without any change in mass flow is considered, equations (A.1) and (A.2) can be combined to describe the ratio of the local cross section  $A$  to the critical cross section  $A^*$  depending on the local flow Mach number.

$$\left(\frac{A}{A^*}\right)^2 = \frac{1}{M^2} \left[ \frac{2}{\gamma+1} \left(1 + \frac{\gamma-1}{2} M^2\right) \right]^{\frac{\gamma+1}{\gamma-1}} \quad (\text{A.4})$$

## APPENDIX B

---

### Modified JANAF Coefficients

---

The coefficients for the JANAF tables [25] are designed to be valid within a temperature range of  $200\text{ K} \leq T \leq 5000\text{ K}$ . This range is not necessarily sufficient for supersonic and hypersonic flows, where static temperatures below  $200\text{ K}$  may occur. For this reason, the polynomial coefficients originally available in OpenFOAM were modified to account for lower temperatures using the software of McBride and Gordon [107]. The updated coefficients for the relevant species  $\text{H}_2$ ,  $\text{He}$ ,  $\text{N}_2$  and  $\text{O}_2$  are listed below. For the sake of completeness, also the species relevant for hydrogen combustion when using Jachimowski's [76] reduced reaction mechanism are included. Although such low static temperatures are not likely to appear in reaction zones, this may still happen in case of frozen chemical reactions, for example within an expansion nozzle.

H		H	1	G	50.00	5000.00	1000.00	1
	2.49989e+00	1.51504e-07	-8.38480e-11	1.85520e-14	-1.44711e-18			2
	2.54737e+04	-4.46283e-01	2.49983e+00	7.11615e-07	-8.60871e-10			3
	8.32271e-14	2.13262e-16	2.54737e+04	-4.46099e-01				4
H2		H	2	G	50.00	5000.00	1000.00	1
	3.02345e+00	6.42367e-04	-2.40903e-08	-1.65102e-11	2.15977e-15			2
	-8.45061e+02	-1.51769e+00	2.34158e+00	8.03079e-03	-1.97038e-05			3
	2.04999e-08	-7.54114e-12	-9.17956e+02	6.90881e-01				4

## B Modified JANAF Coefficients

---

H02	H	10	2	G	50.00	5000.00	1000.00	1
4.06011e+00	2.15598e-03	-5.45680e-07	6.46157e-11	-3.12565e-15				2
9.50723e+01	3.54780e+00	4.29476e+00	-4.73680e-03	2.12786e-05				3
-2.45449e-08	9.44026e-12	2.95756e+02	3.74985e+00					4
H202	H	20	2	G	50.00	5000.00	1000.00	1
3.09135e+00	1.03511e-02	-9.85000e-06	4.94854e-09	-9.75644e-13				2
-1.77293e+04	7.63722e+00	3.14935e+00	6.21278e-03	5.89623e-06				3
-1.50204e-08	7.32739e-12	-1.76352e+04	8.08230e+00					4
H20	H	20	1	G	50.00	5000.00	1000.00	1
2.63919e+00	3.10421e-03	-8.98483e-07	1.25762e-10	-6.83899e-15				2
-2.98797e+04	7.06571e+00	4.19466e+00	-2.00012e-03	6.41243e-06				3
-5.35647e-09	1.71333e-12	-3.02934e+04	-8.32864e-01					4
HE	HE	1		G	50.00	5000.00	1000.00	1
0.02500e+02	0.00000e+00	0.00000e+00	0.00000e+00	0.00000e+00				2
-0.07454e+04	0.09154e+01	0.02500e+02	0.00000e+00	0.00000e+00				3
0.00000e+00	0.00000e+00	-0.07454e+04	0.09154e+01					4
N2	N	2		G	50.00	5000.00	1000.00	1
2.84029e+00	1.62074e-03	-6.38711e-07	1.16393e-10	-7.95651e-15				2
-8.83740e+02	6.48469e+00	3.53079e+00	-1.13740e-04	-5.55918e-07				3
2.52037e-09	-1.45075e-12	-1.04703e+03	2.96736e+00					4
O	O	1		G	50.00	5000.00	1000.00	1
2.54229e+00	-2.39913e-05	-6.69191e-09	5.64101e-12	-5.40897e-16				2
2.92264e+04	4.92919e+00	3.16678e+00	-3.27770e-03	6.66713e-06				3
-6.18246e-09	2.14295e-12	2.91225e+04	2.05900e+00					4
O2	O	2		G	50.00	5000.00	1000.00	1
3.61509e+00	7.43739e-04	-1.95568e-07	3.31518e-11	-2.34305e-15				2
-1.19912e+03	3.66705e+00	3.78377e+00	-3.00829e-03	9.87759e-06				3
-9.71725e-09	3.25825e-12	-1.06402e+03	3.65231e+00					4
OH	H	10	1	G	50.00	5000.00	1000.00	1
2.90159e+00	9.84045e-04	-2.12212e-07	1.84304e-11	-2.59212e-16				2
3.92253e+03	5.49979e+00	4.11883e+00	-3.19401e-03	6.49935e-06				3
-5.82348e-09	2.09090e-12	3.59938e+03	-6.61842e-01					4

---

## Additional Data for the Investigation of the Strut Injector

---

### C.1 Uncertainty Analysis

In order to determine the influence of the total temperature level on the accuracy of the dimensionless surface temperature  $\Theta$ , an uncertainty analysis is conducted. As only single measurements and simulations are considered, no statistical analysis can be applied. A Gaussian root sum square method is used instead, which has been shown to be also valid for single sample studies [113, 114].

The basic form of the uncertainty is given as

$$\delta\Theta = \sqrt{\sum_{n=1}^N \left( \frac{\partial\Theta}{\partial T_n} \delta T_n \right)^2}. \quad (\text{C.1})$$

According to its definition in equation (3.2), the dimensionless surface temperature is a function of the three temperatures  $T$ ,  $T_{min}$  and  $T_{max}$ .

## C Additional Data for the Investigation of the Strut Injector

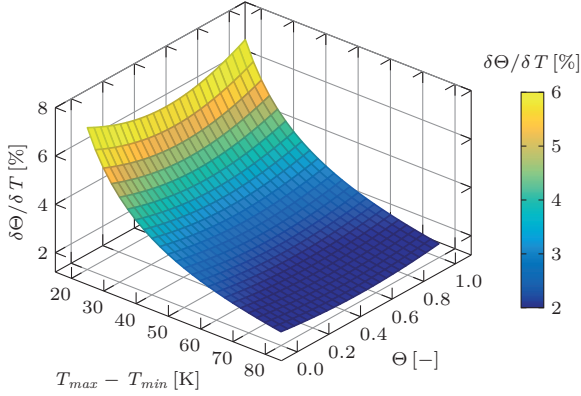


Figure C.1: Relative uncertainty of  $\Theta$

Assuming identical absolute values for the uncertainties in temperature, i.e.

$$(\delta T)^2 = (\delta T_{max})^2 = (\delta T_{min})^2, \quad (C.2)$$

and inserting the three corresponding partial derivatives in equation (C.1) yields

$$\frac{\delta\Theta}{\delta T} = \frac{1}{T_{max} - T_{min}} \sqrt{1 + \left(\frac{T_{min} - T}{T_{max} - T_{min}}\right)^2 + \left(\frac{T - T_{max}}{T_{max} - T_{min}}\right)^2}. \quad (C.3)$$

Equation (C.3) can be simplified by expressing the quadratic terms on the right hand side as functions of  $\Theta$ , which results in

$$\frac{\delta\Theta}{\delta T} = \frac{1}{T_{max} - T_{min}} \sqrt{1 + (-\Theta)^2 + (\Theta - 1)^2} \quad (C.4)$$

and can be further simplified to

$$\frac{\delta\Theta}{\delta T} = \sqrt{\frac{2(\Theta^2 - \Theta + 1)}{(T_{max} - T_{min})^2}}. \quad (C.5)$$

The resulting distribution of  $\delta\Theta/\delta T$  is shown in figure C.1. The relative uncertainty increases for low temperature differences  $T_{max} - T_{min}$  and, slightly, also towards extreme values of  $\Theta$ . This has to be taken into account when evaluating the data at lower total flow temperatures. For example, the temperature

difference  $T_{max} - T_{min}$  is in the order of 40 K at  $T_t = 400$  K, while it is about 80 K if the total flow temperature is raised to  $T_t = 500$  K. This results in an approximately twice as large relative uncertainty at  $T_t = 400$  K.

## C.2 Injector Material Variation

Supplementary to the results for the variation of the injector material, as presented in section 6.2.3, the corresponding numerical data for an external flow total temperature of  $T_t = 400$  K is provided in figure C.2. Compared to the previous investigations at  $T_t = 500$  K, the lower external flow temperature leads to an overall reduction of temperature differences. Therefore, according to the uncertainty analysis for  $\Theta$ , this case is more prone to errors and is only considered as addendum.

Similar to the findings at  $T_t = 500$  K, the hottest zone of the uncooled strut is found to be in the aft region downstream of the reflected leading edge shock impact onto the surface. While an influence of the channel side wall

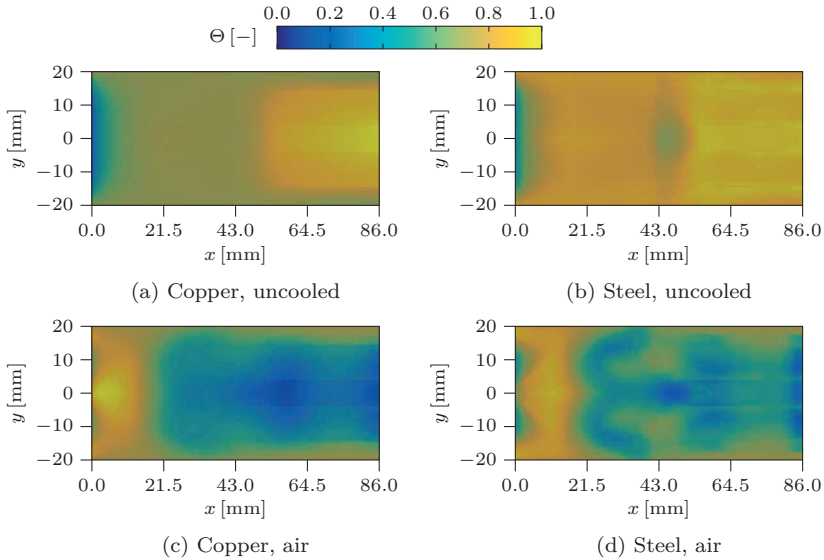


Figure C.2: Influence of the injector material on the dimensionless surface temperature,  $T_t = 400$  K

## C Additional Data for the Investigation of the Strut Injector

---

can be seen for the copper injector, this effect is found to be reduced for the stainless steel model. This is due to the low thermal conductivity of steel and the low temperature difference between wall and injector at this flow temperature. The overall level of  $\Theta$  is higher for steel, which is also the case for  $T_t = 500$  K as discussed in section 6.2.3. Furthermore, the onset of the expansion fan at mid-length of the strut only affects the dimensionless surface temperature significantly in case of the steel injector, where a local reduction in  $\Theta$  is observed.

If the internal cooling is activated, the results do not differ significantly from the findings at  $T_t = 500$  K. The copper injector provides a more homogeneous distribution of  $\Theta$ , while parts of the internal geometry are reflected in the dimensionless surface temperature for the steel injector. The familiar upstream propagation of the shock system inside the channel, which causes the characteristic hot spot in the center of the leading edge, is observed independently of the injector material.

---

### Scaling Performance of *scramjetFoam*

---

The results for the scaling analysis were obtained using the computational grid for the strut section as discussed in chapter 6. It consists of approximately 11.5 million cells per region. The computations were performed on the CRAY XC40 ‘Hazel Hen’ at HLRS in Stuttgart. In order to investigate speed-up and performance, the number of processors used for the computation was varied for given grid size and numerical setup, thus a so-called strong scaling is presented. Parallelization is obtained using the OpenFOAM MPI data exchange with a spatial grid decomposition, where the number of grid cells for each processor is as close to equal as possible.

The speed-up  $S_n$  of parallel computations using  $n$  processors can be written as

$$S_n = \frac{t_n}{t_{ref}}, \quad (\text{D.1})$$

where  $t_{ref}$  is the final simulation time of the test case after a fixed number of hours of wall clock time using a reference number of CPUs. Decomposing the case into the single processors is conducted externally, thus the entire CPU time is used only for the numerical simulation. For the present study a computation using 12 CPUs is taken as reference case for the speed-up investigation, which

## D Scaling Performance of *scramjetFoam*

Table D.1: Data for the strong scaling test at HLRS (HT: Hyper-threading)

CPUs	24	48	96	192	384
Cells / CPU	$4.86 \cdot 10^5$	$2.43 \cdot 10^5$	$1.21 \cdot 10^5$	$0.61 \cdot 10^5$	$0.30 \cdot 10^5$
$S$	2.08	4.30	8.84	15.02	7.46
$E$	104.0%	107.6%	110.5%	93.3%	23.3%
$S$ (HT)	-	2.21	4.50	7.56	5.06
$E$ (HT)	-	55.2%	56.3%	47.2%	15.8%

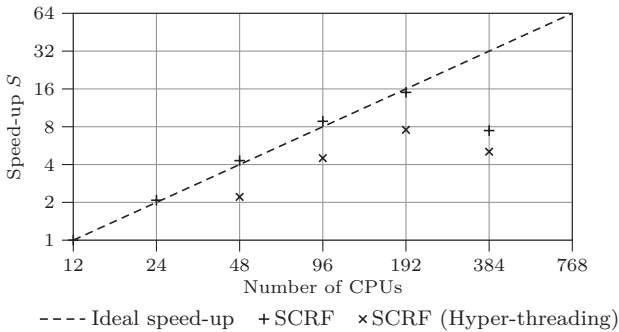


Figure D.1: Strong scaling of *scramjetFoam* on Cray XC40 at HLRS

corresponds to half a computational node on the CRAY XC40 architecture. The wall clock time was set to three hours for all simulations. An ideal speed-up for a simulation using  $n$  processors would therefore be reached for  $S_n = n/12$ , which allows the definition of a parallel efficiency  $E$ .

$$E = \frac{12 t_n}{n t_{12}} = \frac{12 S_n}{n} \quad (\text{D.2})$$

Table D.1 shows the approximate number of grid cells per processor for the conducted simulations as well as an overview of the performance. As the fluid region contains slightly more grid cells than the solid region, this value is taken as reference. The corresponding speed-up evaluation is presented in figure D.1.

The results show that a good speed-up behavior is achieved as long as hyper-threading is deactivated. For these simulations a lower efficiency limit of approximately 50 000 cells per CPU can be determined. If more CPUs are used,

---

the computational overhead rises significantly due to an increasing number of inter-processor boundaries, which require the exchange of data between the processors.

In addition to the scaling study, also the effect of hyper-threading on parallel efficiency is investigated. As shown in figure D.1, hyper-threading always results in a considerably less efficient parallelization. Virtually no speed-up at all can be achieved when switching from a calculation running on  $n$  nodes with  $24n$  processors to a setup using the same number of nodes with hyper-threading, i.e. running on  $n$  nodes with  $48n$  processors.